Geotechnical Investigation for the Emplacement of Radio Telemetry Dishes at the Matjiesfontein Space Geodesy Observatory

by

Jaco Coetzee

Thesis presented in fulfilment of the requirements for the degree of Master of Engineering in the Department of Civil Engineering at Stellenbosch University

Supervisor - Mr L. Croukamp

March 2020

Acknowledgements

Throughout the writing of this thesis I received a great deal of assistance and support from several people that I would like to express my sincere gratitude to. Firstly I would like to thank my supervisor, Mr. Leon Croukamp, for his vital input and guidance throughout the project. I would like to thank our experienced geotechnical and structural laboratory technicians, Mr. Colin Isaacs, Mr Gavin Williams and Mr Charlton Ramat for their assistance during testing.

I would like to thank Dr. Roelf Botha of HartRAO for financing the drilling operations and allowing me to visit their radio observatory and Mr Eugene Avenant of SANSA for providing important information with regard to the preliminary foundation design; Prof. Andrezj Kijko for providing resources and insight regarding the seismic hazard at Matjiesfontein; Prof. Philip Paige-Green for providing copies of very useful papers on Dwyka tillite; Dr. Peter Day and Mr. Frans van der Merwe for their helpful course presentations and guidance.

I would also like to thank Dr. Botha, Mr. Tommy Vlok, Mr. Eon Croukamp, Dr. Stoffel Fourie and my supervisor for their invaluable assistance during the geophysical investigation. Finally, I would like to thank my father, the Namibia Water Corporation (NamWater) and Stellenbosch University for the opportunity and my friends and family for their support throughout the project.

Declaration

By submitting this thesis electronically, I declare that the entirety of the work contained therein is my own, original work, that I am the sole author thereof (unless to the extent explicitly otherwise stated), that the reproduction and publication thereof by Stellenbosch University will not infringe any third party rights and that I have not previously in its entirety or in part submitted it for obtaining any qualification.

Signature: .....
Date: .....

Abstract

Geotechnical Investigation for the Emplacement of Radio Telemetry Dishes at the Matjiesfontein Space Geodesy Observatory

J. Coetzee

Department of Civil Engineering,

University of Stellenbosch,

Private Bag X1, 7602 Matieland, South Africa.

Thesis: MEng (Civil)

March 2020

A secondary site area at the Matjiesfontein Space Geodesy Observatory (MSGO) has provisionally been selected for the emplacement of large radio telemetry dishes. While several investigations have been performed for the geotechnical characterization of the main MSGO site area, similar data that pertains to the newly selected site area is mostly unavailable. Since telemetry dishes are sensitive structures that require very stable founding conditions, a geotechnical investigation was performed to determine the suitability of the new site area for emplacement. Furthermore, the procurement and transportation of materials from external sources is typically among the highest expenditures of construction projects. In addition, unutilized materials leave a larger footprint on the environment. Therefore, tests were performed to determine the suitability of local material for use as coarse aggregate in concrete.

Two variations of the predominant underlying rock type, namely slightly and highly weathered Dwyka tillite, were collected for coarse aggregate tests. Sample characteristics were tested as follows: particle size distribution and dust content through grading analyses; particle shape through Flakiness Index (FI) tests; crushing resistance and water absorption through a full set of dry and soaked Aggregate Crushing Value (ACV) and 10 % Fines Aggregate Crushing Value (10%FACT) tests; and durability through a modified slake durability test. All requirements were met comfortably by slightly weathered tillite. On the other hand, the dust content, soaked crushing resistance, water absorption and slake durability of highly weathered tillite indicated that it may adversely affect the workability and water requirement of fresh concrete as well as the durability of hardened concrete. While slightly weathered tillite is deemed suitable for use as coarse aggregate in concrete, the use of highly weathered tillite is not recommended. Furthermore, a basic feasibility study indicated that the local production of aggregate can reduce construction costs significantly.

Rock mass characterization was performed through geophysical electro-resistivity tests, drilling and core logging, the Rock Quality Designation (RQD) and Rock Mass Rating (RMR) systems and Unconfined Compressive Strength (UCS) tests. Electro-resistivity imaging along the length of the site area indicated that competent rock can be found within a few metres below the surface. Furthermore, no distinct problem areas were identified. Recovered core consisted predominantly of unweathered and slightly weathered tillite, while medium weathered tillite was encountered in subordinate amounts. The overall rock quality was classified as "good to fair rock" according to the RQD and RMR systems. Based on the results of numerous UCS tests, unweathered and slightly weathered tillite were classified as "hard to very hard rock" according to standard core logging guidelines, while medium weathered tillite was classified as "medium hard rock".

Finally, a preliminary foundation design was performed to determine the minimum foundation diameter and indicate potential governing factors. The design indicated that the minimum foundation diameter would ultimately be governed by the size of the superstructure and the space required inside the pedestal for the housing and operation of telemetry equipment, since safety against the verified failure modes was satisfied at relatively small diameters. Therefore, local founding conditions are indeed suitable for the emplacement of large telemetry dishes.

Opsomming

Geotegniese Ondersoek vir die Plasing van Radiotelemetrie Skottels by die Matjiesfontein "Space Geodesy Observatory"

J. Coetzee

Departement Siviele Ingenieurwese,

Universiteit van Stellenbosch,

Privaatsak X1, 7602 Matieland, Suid Afrika.

Thesis: MIng (Siviel)

Maart 2020

'n Nuwe sekondêre terrein by die Matjiesfontein "Space Geodesy Observatory" (MSGO) is voorlopig geselekteer vir die plasing van groot radiotelemetrie-skottels. Hoewel verskeie ondersoeke in die verlede uitgevoer is vir die geotegniese karakterisering van die van die MSGO-hoofterrein, is soortgelyke inligting met betrekking tot die nuwe terrein grotendeels onbeskikbaar. Aangesien telemetrie-skottels sensitiewe strukture is wat besonder stabiele grondvestingstoestande verg, is 'n geotegniese ondersoek uitgevoer om die geskiktheid van die nuwe terrein te bepaal. Verder word die aankoop en vervoer van boumateriaal vanaf eksterne bronne tipies getel onder die grootste uitgawes van 'n konstruksieprojek. Onbenutte materiaal laat boonop 'n groter voetspoor op die omgewing. Daarom is toetse uitgevoer om die geskiktheid van plaaslike materiaal te bepaal vir gebruik as growwe aggregaat in beton.

Twee variasies van die oorheersende onderliggende gesteentetipe, naamlik effens en hoogs verweerde Dwyka tilliet, is vir toetse versamel. Die eienskappe van growwe aggregaat is as volg bepaal: partikel-grootte verdeling en stofinhoud deur middel van graderings; partikel vorm deur "Flakiness Index" (FI) toetse; breekweerstand en waterabsorpsie deur 'n volledige stel droë en deurweekte "Aggregate Crushing Value" (ACV) en "10 % Fines Aggregate Crushing Value" (10%FACT) toetse; en duursaamheid deur middel van 'n aangepasde blusbaarheid-stoets.

Hoewel effens verweerde tilliet aan alle vereistes voldoen, het die stofinhoud, deurweekte breekweerstand, waterabsorpsie en blusbaarheid van hoogs verweerde tilliet aangedui dat dit die bewerkbaarheid en waterbehoefte van 'n betonmengsel nadelig mag beïnvloed. Gevolglik, terwyl effens verweerde tilliet as geskik beskou word vir gebruik as growwe aggregaat in beton, word die gebruik van hoogs verweerde tilliet nie aanbeveel nie. Verder het 'n basiese uitvoerbaarheidstudie aangedui dat die plaaslike produksie van growwe aggregaat konstruksiekostes aansienlik kan verminder.

Rotsmassa-karakterisering is uitgevoer deur middel van geofisiese elektro-resistiwiteitstoetse, kernmonster-ontleding, die "Rock Quality Designation" (RQD) en "Rock Mass Rating" (RMR) stelsels asook onbeperkte druksterkte (UCS) toetse. Elektro-resistiwiteitsbeelding oor die lengte van die terrein het aangedui dat geskikte rots binne enkele meters onder die oppervlak aangetref word. Daar is ook geen duidelike probleemareas geïdentifiseer nie. Herwonne kernmonsters bestaan hoofsaaklik uit onverweerde en effens verweerde tilliet, terwyl medium verweerde tilliet in kleiner hoeveelhede voorkom. Die algehele rotsgehalte is volgens die RQD en RMR stelsels geklassifiseer as "billike tot goeie rots". Op grond van die resultate van talle UCS toetse, is onverweerde en effens verweerde tilliet volgens standaard riglyne geklassifiseer as "harde tot baie harde rots", terwyl medium verweerde tilliet geklassifiseer is as "medium harde rots".

Laastens is 'n preliminêre fondasie-ontwerp uitgevoer om die minimum diameter van die fondasie te bepaal om as 'n aanduiding te dien van potensiële beherende faktore. Die ontwerp het aangedui dat die minimum diameter van die fondasie uiteindelik bepaal sal word deur die grootte van die superstruktuur en die ruimte wat benodig word in die voetstuk vir die behuising en bediening van telemetrie-toerusting, aangesien veiligheid teen alle oorwoë swigtingsmeganismes reeds by kleiner diameters bevestig is. Dus is plaaslike grondvestingstoestande inderdaad geskik vir die plasing van groot telemetrie-skottels.

Contents

List of Figures

List of Tables

List of Abbreviations

Abbreviation	Meaning
10%FACT	*10% Fines Aggregate Crushing Value*
ACV	*Aggregate Crushing Value*
ASR	*Alkali-Silica Reaction*
CDSCC	*Canberra Deep Space Communications Complex*
DSN	*Deep Space Network*
FAST	*Five-Hundred-Metre Aperture Spherical Telescope*
FI	*Flakiness Index*
FoS	*Factor of Safety*
GNSS	*Global Navigation Satellite Systems*
GSI	*Geological Strength Index*
HartRAO	*Hartebeesthoek Radio Astronomy Observatory*
ICRF	*International Celestial Reference Frame*
LL	*Liquid Limit*
LSD	*Limit States Design*
MSGO	*Matjiesfontein Space Geodesy Observatory*
NASA	*National Aeronautics and Space Administration*
PI	*Plasticity Index*
PL	*Plastic Limit*
RMR	*Rock Mass Rating*
RQD	*Rock Quality Designation*
S/LLR	*Satellite/Lunar Laser Ranger*
SCaN	*Space Communications and Navigation*
SKA	*Square Kilometre Array*
SL	*Shrinkage Limit*
SLS	*Serviceability Limit State*
UCS	*Unconfined Compressive Strength*
ULS	*Ultimate Limit State*
VLBI	*Very Long Baseline Interferometry*

Chapter 1

Introduction

1.1 Background

A site located 3 km south of Matjiesfontein, namely the Matjiesfontein Space Geodesy Observatory (MSGO), has been under development as an outstation of the Hartebeesthoek Radio Astronomy Observatory (HartRAO) since 2008. The area was selected for its favourable atmospheric seeing conditions, sparse population, radio quietness and existing infrastructure. This research project pertains to the emplacement of at least 2 radio telemetry dishes 2 km north of the main site area (see Figure 1.1), which are intended to track and communicate with satellites in orbit around Earth and spacecraft/probes through the reception and transmission of radio waves.

Figure 1.1: Layout of the Matjiesfontein area illustrating the main and secondary MSGO site areas.

1.2 Problem Statement

The South African network of space geodesy and astronomical observation stations must be upgraded constantly if it is to continue to play an important role in a global context. If not maintained and developed, ageing technology and a relatively sparse distribution of stations will eventually struggle to meet the ever-increasing standards of the industry and scientific community. Site areas are selected very carefully and must meet numerous requirements that facilitate successful operation, one of which is stable founding conditions.

1.3 Motivation for Research

Radio telemetry dishes are required to communicate accurately over extraordinarily long distances. With some deep space missions they may even be required to interact with probes that travel on the outskirts of our solar system; in these cases, they must be accurate to a few metres over millions of kilometres. Due to distance, the reception and transmission of data could take several hours. Consequently, the dishes need to be completely stable during operation and stringent limitations are specified for displacement and differential settlement. Moreover, failure could damage sensitive instruments and put dishes out of use for long periods of time.

Not only could damages be extremely expensive, it could also be detrimental to the mission at hand. It is therefore important that a geotechnical investigation is conducted to ensure stable founding conditions. Regarding construction, transportation costs are typically one of the greatest expenditures. Since large volumes of concrete will be required for the construction of the foundations and accompanying structures, it may be more feasible to produce aggregates from local materials, e.g. from excavated rock. However, the question must first be answered whether the material is adequate for utilization as aggregate in concrete.

1.4 Research Goals and Objectives

Goals:

- Determine the suitability of local material for use as coarse aggregate in concrete
- Determine whether the proposed site area provides stable founding conditions for the emplacement of large telemetry dishes

Objectives:

- Analyse the grading, Flakiness Index, Aggregate Crushing Value, 10 % Fines Aggregate Crushing Value and slake durability of the predominant lithology at the site area, Dwyka tillite
- Determine and compare the suitability of slightly and highly weathered tillite for use as coarse concrete aggregate based on results of the aforementioned tests
- Broadly assess the feasibility of producing aggregate locally as opposed to procurement from alternative sources
- Perform non-invasive geophysical tests for the characterization of sub-surface structures and identification of potential favourable/problem areas
- Recover core samples from site for core logging and comparison with geophysical results
- Quantify overall rock mass quality through evaluation of the Rock Quality Designation and Rock Mass Rating
- Prepare specimens from recovered core samples for compressive strength tests
- Perform a series of unconfined compressive strength tests on core specimens so that reasonable estimates of compressive strength, elasticity and deformation may be obtained
- Perform a preliminary foundation design for an indication of the minimum required diameter and applicable governing factors

1.5 Report Layout

The thesis is comprised of 5 chapters. In Chapter 1: Introduction, the background and purpose of the research project is discussed and the goals and objectives that serve as framework for the following chapters are outlined.

In Chapter 2: Literature Review, various subjects that pertain to the research topic are reviewed through a desktop study. In addition to providing further background information, the review is aimed at identifying potential problems that may be encountered as well as their causes and solutions.

In Chapter 3: Methodology, the methods that were used to achieve the research goals and objectives are discussed. The discussions include sample collection and preparation, testing

and assumptions/limitations. In Chapter 4: Results and Interpretations, the results of the implemented methods are discussed individually. The significance of the results is interpreted based on standard specifications (Chapter 3) and past research (Chapter 2).

In Chapter 5: Conclusions and Recommendations, the main findings are summarized and evaluated in terms of the research goals. Furthermore, Chapter 5 contains final remarks and recommendations for future research. Finally, the appendices, which contain supporting figures and detailed calculation sheets, are attached at the end of this document.

Chapter 2

Literature Review

The literature review forms an integral part of a comprehensive geotechnical desktop study. Readily available information can provide important insights into the features of a site area, which can be used, for example, to streamline subsequent investigations for the most effective use of resources. Not only can a literature review aid in identifying potential problems, it can also inspire solutions to potential problems. Additionally, it can serve as a reference for terms and concepts that are discussed in the chapters that follow.

As mentioned in Chapter 1, radio telemetry dishes are planned for emplacement at the Matjiesfontein Space Geodesy Observatory (MSGO). The history of Matjiesfontein and the MSGO is discussed to put into perspective their role in the context of a global space-geodetic network. Thereafter, the history and fundamentals of radio astronomy are discussed for a better understanding of the purpose, dynamics and stability requirements of telemetry dishes.

The physiography of the site is reviewed to define the natural patterns and processes that the area is subject to, i.e. location, climate, geology, topography and seismicity. Furthermore, since the site area is underlain predominantly by Dwyka tillite, a separate section is dedicated to discussing its origin, deglaciation sequences, geological characteristics, utilization, potential problems and recommended solutions.

The geotechnical investigation also aims to determine the suitability of local material for use as coarse aggregate in concrete. Therefore, the main characteristics of aggregates that affect the properties of fresh and hardened concrete are discussed. In addition, various rock properties are discussed as they pertain to foundation engineering; the section also touches upon methods that may be used to determine these properties and the problems that are commonly encountered during implementation.

A review of methods and considerations for foundation design is included. The section is mainly focused on the geotechnical design of shallow spread foundations, since other foundation types are not likely to be used for the intended application. Finally, the verification of safety against the main failure modes that are associated with shallow spread foundations are considered, namely bearing failure, sliding failure, overturning failure and excessive settlement.

2.1 Astronomy and Space Observation

2.1.1 History

The night sky inspired many of humankind's most fundamental questions: "where are we?", "are we alone?", "how did we come into being?" and "what is the eventual fate of the universe?". Billions of dollars are spent every year to find answers to these questions (Martin, 2017). Although research is generally driven by scientific curiosity, it has yielded technology and knowledge that arguably justify the expenditures. Technology that was originally developed for space exploration has revolutionized the fields of medical image processing, light-weight materials, solar panels, home insulation, digital data storage, robotics, global navigation and water purification, just to name a few (ISECG, 2013). Interest in celestial phenomena dates back thousands of years. In light of all that has been accomplished, it is easy to forget that there was once a time when many ancient civilizations thought of the Earth simply as a flat mass beneath a hollow, star-spangled dome.

In ancient times, astronomy was used to track climatic changes that would signal ideal times for planting and harvesting. It was also used extensively for navigational purposes, since it provided a reliable reference frame for sailors and desert travellers alike. Most ancient religions were very closely bound to celestial bodies and recurring astronomical events. Therefore, astronomical observations and interpretations were often entrusted to their high priests (Shuttleworth, 2010a). Numerous ancient astronomical observation sites have been discovered all over the world, including pyramids, temples and other mysterious megalithic structures. However, the oldest contributions to western astronomy are attributed to ancient Mesopotamia (parts of modern-day Iraq, Turkey, Syria and Iran) and more specifically, Sumer, its southern-most region (Aveni, 1999).

Mesopotamia is believed to be the cradle of civilization, dating back roughly 10 000 years. The main purpose of Mesopotamian astronomy was to record recurring celestial events. In contrast with Greek astronomers, the Mesopotamians were not particularly concerned about how or why these phenomena were occurring, as they were generally satisfied with vague attributions to religion and astrology (Shuttleworth, 2010b). Eventually, Sumerian knowledge was passed on to the later civilizations of Assyria and Babylon, by whom it was passed on to the Greeks centuries later. Although the Greeks put forth the tradition of tying the stars and planets to their own mythology, they revolutionized the field of astronomy by transforming it from a purely observational science into a theoretical science (Shuttleworth, 2010b). The Greeks understood that the universe obeys certain physical laws. Therefore, it could be explained through reason and mathematics. Astronomy was a subject of great interest among the philosophers – many of whom made discoveries that laid the foundation

of modern astronomy. Many of them dedicated years to the study of astronomy and the overall nature of the universe, modifying each other's theories and producing numerous works throughout their lifetimes (Shuttleworth, 2010b). Galileo Galilei (1564 – 1642) was the first known to use a telescope for astronomy. During his observations, Galileo discovered the four largest moons of Jupiter, namely Io, Europa, Ganymede and Callisto. These moons served as proof that not all objects in the universe revolve around the Earth and that the geocentric model is flawed. Despite the evidence, Galileo was charged with "suspected heresy" and placed under house arrest. It was not until the early 19th century that the ban on heliocentric works was repealed (Reimers, 2015).

The development of astrophotography (19th century) and digital sensing (20th century) vastly improved the quality and sensitivity of astronomical observations. Another revolution occurred when the technology was connected to telescopes and launched into orbit, where the atmosphere does not cloud observations. Images of the Orion Nebula that were taken in 1833 and 2004 are displayed in Figure 2.1 on the left and right, respectively. The image on the left is a photograph taken with an exposure time of 1 hour, while the image on the right is composed of 520 digital images taken by the Hubble Telescope from its low-Earth orbit. Note that Hubble images are taken using several wavelengths, including UV and infrared, which would otherwise be invisible to the eye (Moskowitz, 2010).

Figure 2.1: Development of astrophotography: the Orion Nebula photographed in 1833 (left) and 2004 (right) (ESA/Hubble, 2006).

During World War II, Nazi Germany developed long-range missiles that were used in an attack on London (Deffree, 2017). Thereafter, USA and the Soviet Union started their own missile programs, as they became aware of its potential for space exploration and military

operations. In 1957, the Soviet satellite Sputnik 1 became the first satellite to orbit the Earth, thereby signalling the commencement of the Space Race. In 1958, NASA reciprocated with the launch of their first Earth-orbiting satellite, Explorer 1. Merely a decade later during the famed Apollo missions, Neil Armstrong became the first person to walk on the moon. As the years progressed and international tension faded, space exploration gradually shifted from a competitive race into a combined global effort. Numerous missions have been launched in our solar system, e.g. the Pioneer, Voyager, Galileo, Cassini and New Horizons missions. Of all the Pioneer missions, Pioneers 10 and 11 were the most successful. Launched in 1972 and 1973, they started on their journeys throughout the solar system.

After becoming the first spacecraft in history to successfully navigate through the asteroid belt, Pioneer 10 also became the first to visit the gas giant Jupiter in 1973 (NASA, 2007). Using gravitational assist provided by its flyby of Jupiter, it ventured deeper into space to explore the outskirts of our solar system. After April 2002, Pioneer 10's power source had degraded and, as a result, its signals became too weak to detect (NASA, 2007). Pioneer 11 reached Jupiter in 1974, after which it became the first spacecraft to visit Saturn. It eventually joined Pioneer 10 in its exploration of the outskirts. Contact with Pioneer 11 ceased when its antenna was carried out of view in November 1995 (NASA, 2007).

Voyagers 1 and 2 were launched in 1977 with the goal of building upon the Pioneers' exploration of Jupiter and Saturn. Both spacecraft were sufficiently operational after the completion of their primary missions, resulting in extended projects. Voyager 1 was sent directly into deep space to sample interplanetary medium, while Voyager 2 was instructed to visit Neptune and Uranus. Thereafter, Voyager 2 was also sent into deep space. (NASA JPL, n.d.). Unlike the Pioneers, the Voyager spacecraft are still operational and are credited with the longest operating space missions in history (NASA JPL, n.d.).

The later missions of Galileo (Jupiter), Cassini (Saturn) and New Horizons (Pluto) were conducted in a similar manner – utilizing gravitational assists, visiting numerous moons and collecting data that delivered great insights into the nature of the objects in our solar system. The Galileo and Cassini spacecraft were instructed to collide with Jupiter and Saturn, respectively, and were destroyed by extreme heat and pressure. The orders were given to prevent collisions with the planets' moons after their missions had been completed.

Although the spacecraft themselves were designed ingeniously, they would not have been able to complete their missions without communication from Earth. They depended on timely instructions that allowed them to navigate, deploy probes, reboot/update systems and operate their instruments. Communications infrastructure is also responsible for receiving the data collected by a spacecraft during its exploration.

2.1.2 Radio Telemetry

The Deep Space Network (DSN) is the primary communications infrastructure for deep space missions (Mai, 2018). The DSN is a network of antennas operated by NASA's Jet Propulsion Laboratory (JPL). The Near-Earth Network (NEN) and the Space Network (SN), on the other hand, serve as communications infrastructure mainly for satellites in the Earth-moon system. The DSN, NEN and SN are all subdivisions of NASA's Space Communications and Navigation (SCaN).

Due to the size and rotation of Earth, a minimum of three complexes are required to maintain an unobstructed view of the solar system (Mai, 2018). The complexes, namely the Goldstone (California), Madrid (Spain) and Canberra (Australia) complexes, were established approximately 120 degrees apart in longitude, i.e. each spaced roughly $\frac{1}{3}$ around the globe, as shown in Figure 2.2.

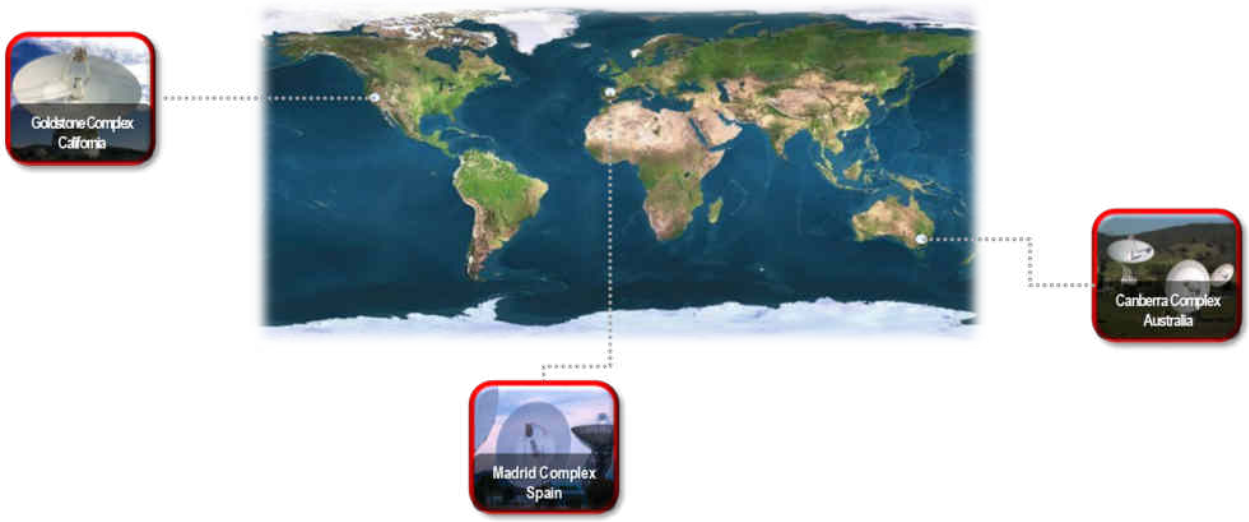

Figure 2.2: DSN communication complexes, eached spaced roughly one third around the globe (Mai, 2016).

A large variety of dish diameters are used, the largest of which is 70 m (Redd, 2018). The 70 m diameter Goldstone dish is shown in Figure 2.3. They act as transmitters and receivers for spacecraft and guide them through the solar system. Received signals, i.e. coded information in the form of radio waves, are reflected off the main reflector into the secondary reflector, which is suspended above the centre of the dish. The secondary reflector focuses the signals into the centre of the dish. Thereafter, they are reflected by a series of mirrors onto a receiver in the pedestal. The coded package is processed several times by the DSN and JPL to obtain meaningful data, for example images or equipment status reports.

Figure 2.3: 70 m dish at the Goldstone Deep Space Communications Complex, California (Dunford, 2012).

After receiving images or equipment status reports, the scientists at JPL usually write programs for the spacecraft that include instructions or system updates. Once they are ready, the programs are converted into radio signals and sent to the spacecraft via an unobstructed DSN complex. Here, the antennas serve as transmitters, reflecting the signal back through the series of mirrors, onto the primary reflector and into space.

To study the ancient beginnings and eventual fate of the universe, scientists need to peer billions of light-years into space. Therefore, The DSN complexes, like many other observation stations, have been using their dishes as radio telescopes for decades. In contrast with most other forms of radiation, radio waves have the ability to penetrate the atmosphere and reach ground-based observation stations, as illustrated in Figure 2.4.

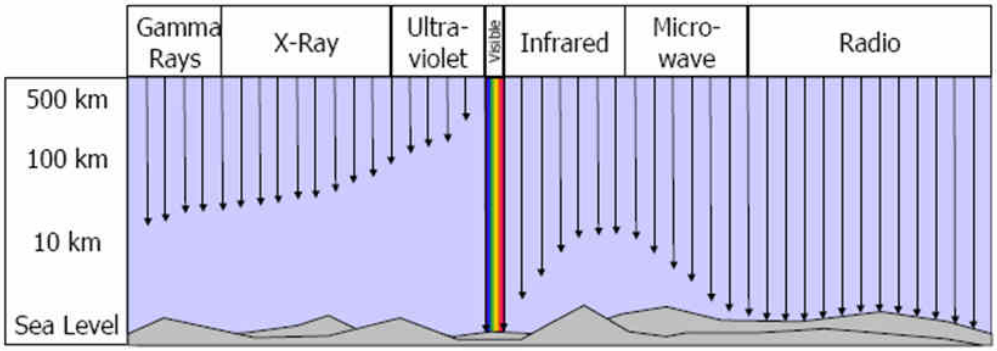

Figure 2.4: Penetrating ability of different wave frequences (Harris Geospatial Solutions Inc., 2018).

Cosmic radio emissions were first detected during the early 1930s by American physicist and engineer, Karl Jansky (Mukai, 2016). While optical telescopes detect energy within the visible portion of the electromagnetic spectrum, cosmic energy is often emitted in frequencies that are either too high or too low to be seen. Since radio emissions may contain wavelengths that are in the order of a million times longer than that of visible light, the telescopes require extremely large diameters to achieve the same angular resolution as optical telescopes (Mukai, 2016).

Angular resolution refers to the minimum angular spacing at which two radio sources can be distinguished, i.e. the ability to distinguish detail. Angular resolution is determined by Rayleigh's Criterion, which states that it is proportional to the wavelength of the incoming signal and inversely proportional to the diameter of the aperture; as shown in Equation 2.1 (Mukai, 2016):

$$\theta = 1.22\frac{\lambda}{D} \tag{2.1}$$

Where:
θ = Angular Separation (Rad)
λ = Wavelength (m)
D = Aperture Diameter (m)

Consequently, one would need to create a dish with a diameter of several kilometres to achieve the angular resolution of the optic Hubble Space Telescope. In comparison, the world's largest single-aperture (single dish component) radio telescope, the Five-hundred-metre Aperture Spherical Telescope (FAST), has a total diameter of 500 m and an effective aperture of roughly 300 m (Nan et al., 2002). Although FAST, as displayed in Figure 2.5, is a great feat of modern engineering, the telescope by itself cannot provide sufficient angular resolution for ambitious deep space observations.

Figure 2.5: The Five-hundred-meter Aperture Spherical (radio) Telescope, southwestern China (Zinan, 2019).

Fortunately, radio telescopes are not limited to consisting of single apertures. Numerous radio telescopes can be linked together to form arrays known as interferometers. Radio interferometers are essentially massive synthesized single aperture telescopes. A synthesized aperture can be regarded as an incomplete single aperture, where elements only exist at the locations of the individual antennas. The angular resolution of an interferometer can be improved by increasing the maximum distance, or baseline, between antennas.

When baselines are stretched over such great distances, the process is referred to as Very Long Baseline Interferometry (VLBI). NASA's Space VLBI, for example, consists of both orbiting antennas and ground-based antennas – the synthesized aperture is equivalent to a single dish with a baseline that exceeds the diameter of the Earth. The sensitivity of an interferometer (ability to distinguish signals from background noise) can be improved by increasing the number of antennas in the array, thus decreasing the number of "missing" elements in the synthesized aperture (SKA, 2018).

Although there are several other factors involved that may limit the abilities of radio telescopes, such as space, cost or electrical processing ability, interferometers can be expanded to sizes that allow them to outperform optical telescopes. In addition, the individual telescopes of an array can be adjusted to observe different parts of the sky simultaneously, whereas single aperture telescopes are only able to observe in one direction at a time. Therefore, radio dishes are currently being employed as building blocks in the construction of the largest and most sensitive telescope on Earth, the Square Kilometre Array (SKA).

The SKA is mainly being constructed over parts of South Africa and Australia. Roughly 100 organizations from 20 countries are contributing to its development (SKA South Africa, 2018). The synthesized aperture will be approximately 50 times more sensitive and survey at speeds roughly 10 000 times faster than the foremost radio telescopes of today. Furthermore, the system will be able to process data at rates that exceed global internet traffic. The primary purpose of the project is to provide insight into various scientific questions, including how the first planets and galaxies were formed, how gravitational and magnetic waves behave throughout the universe, the nature of dark matter and whether intelligent life exists beyond Earth (SKA South Africa, 2018).

2.2 Matjiesfontein

2.2.1 History

Named after the Matjiesgoed reed, a plant that was traditionally used for the weaving of mats and baskets, the small Karoo town of Matjiesfontein, as displayed in Figure 2.6, was established in 1884 by James Douglas Logan (Frandsen, 2018). Today Matjiesfontein has a population of a few hundred people. However, it was once a place of first-rate luxury, international cricket and war.

Figure 2.6: Aerial view of Matjiesfontein (Keurkloof Karoo Farm Accomodation, 2018).

According to Frandsen (2018), Logan was a Scotsman who arrived in South Africa by accident in 1877. He worked as an apprentice on a sailing vessel that suffered storm damage on its way to Queensland, Australia. Consequently, the vessel had to anchor at Simonstown for repairs. During the delay, Logan obtained an official discharge and went to work for the Cape Province Railway Service as a porter (Buser, 2014). Years later, he became the superintendent of the railway line between Hex River and Prince Albert. There, in the Great Karoo, he set up the station that would evolve into Matjiesfontein.

In 1883, Logan parted ways with the Railway Service and bought his farm, Tweedside. He proceeded to develop the land by planting orchards wherever he could find a sufficient water supply. To the amazement of many who had initially advised against it, his desert orchards flourished to such an extent that he established his own private railway station to facilitate the transportation of the produce (Frandsen, 2018). Logan was a pioneer in many ways. At one stage, his home was the only private dwelling in South Africa with electrical lights and

waterborne sewage. The telephone line that was lain from his farm lodge to his house in Matjiesfontein was roughly 20 km long, the longest private landline in South Africa at the time. Other additions included a swimming pool, houses, shops, golf links and, since Logan was a great advocate of the sport, a full-sized cricket pitch. One of the first international test matches between South Africa and England was held there in the 1890s (Buser, 2014). With the commencement of the South African Anglo-Boer War in 1899, Matjiesfontein became the headquarters of the Cape Command, hosting roughly 12 000 British soldiers. During this time, the hotel was utilized as a military hospital and lookout post (Frandsen, 2018).

In 1968, the village was purchased by hotelier David Rawdon, by whom it was restored to its current state. Today it is a window to the past; with the famous Lord Milner hotel, the transport museum and the Marie Rawdon museum - one of the largest private collections of Victorian era memorabilia and Anglo-Boer War artefacts in the world - it was declared a National Heritage Site in 1975.

2.2.2 Matjiesfontein Space Geodesy Observatory (MSGO)

Space geodesy is an interdisciplinary research method that involves the application of the principles of mathematics, physics and astronomy for the determination of fundamental Earth parameters. The parameters are typically used to model the exact shape, size, rotation and orientation of the Earth within the International Celestial Reference Frame (ICRF), which is also maintained through space geodesy (Combrinck, 2007). Other applications include the determination of ice sheet thicknesses, mean sea levels, wave heights and tectonic plate velocities. As a result, space geodesy benefits many other fields of study, such as climate change and natural hazard mitigation.

According to Combrinck (2007), space geodesy is growing rapidly and international requirements are becoming more stringent. Therefore, the global network of space geodesy stations must grow in number as well as technological capability. Space geodesy in South Africa has gained a lot of support internationally because of its institutional and geographical potential. However, if South Africa is to continue to play an important role in the global network, it must grow accordingly (Combrinck, 2007).

For that reason, it was decided that a new station will be developed as an outstation of the Hartebeesthoek Radio Astronomy Observatory (HartRAO). After careful consideration, a site located in a small depression roughly 3 km south of Matjiesfontein and just north of the Witteberge was selected for the new station, namely the Matjiesfontein Space Geodesy Observatory (MSGO). The main site area of the MSGO is shown in Figure 2.7. It is isolated from densely populated cities, where radio frequency interference and light pollution are

major concerns. Atmospheric seeing conditions are also favourable due to its clear skies. Furthermore, sufficient existing infrastructure is available, i.e. water, electricity, the N1 national road, railway station, airstrip and accommodation (Combrinck, 2007).

Figure 2.7: The main site area of the MSGO, situated in a slight depression in front the Witteberge.

A Global Navigation Satellite System (GNSS) station was installed in 2008 and was the first addition to the MSGO. In 2013, a vault was constructed in a rock face as a housing unit for 3 seismometers and a gravimeter (L. Croukamp, pers. comm., 2019), as displayed in Figure 2.8. In addition, solar panels have been installed at a borehole that will supply water to the site. Future additions include a Satellite/Lunar Laser Ranger (S/LLR) and radio telescope dishes. The S/LLR will be used to determine geometrical ranges to retroreflectors that were either placed on the moon during the Apollo missions or installed on satellites.

Figure 2.8: Outside (left) and inside (right) of the seismic vault at the main site area.

Provisionally, it is planned that at least 6 dishes will be emplaced, 4 of which will be lo-

cated at the main site area for Very Long Baseline Interferometery (VLBI) and 2 of which will be located near the airstrip to be used for radio telemetry (Botha, pers. comm., 2019). Geotechnical investigations for the the rock vault, S/LLR and VLBI antennas were carried out by Van Wyk (2013), Bothma (2015) and Janse van Rensburg (2017), respectively, while the geotechnical investigation for the emplacement of the radio telemetry dishes near the airstrip is the focus of the current study.

2.3 Site Physiography

2.3.1 Location

The site is located in the south-western reaches of the Great Karoo - roughly 1 km south of Matjiesfontein, just off the N1 national route between Touwsrivier and Laingsburg, as shown in Figure 2.9.

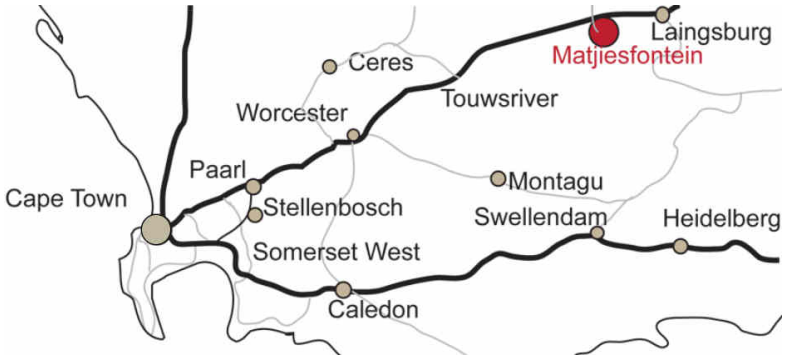

Figure 2.9: Location of Matjiesfontein relative to other towns in the Western Cape (Snyderskloof, 2013).

The area of interest can be found on the 3320BA Matjiesfontein topographic sheet of South Africa, as illustrated in Figure 2.10.

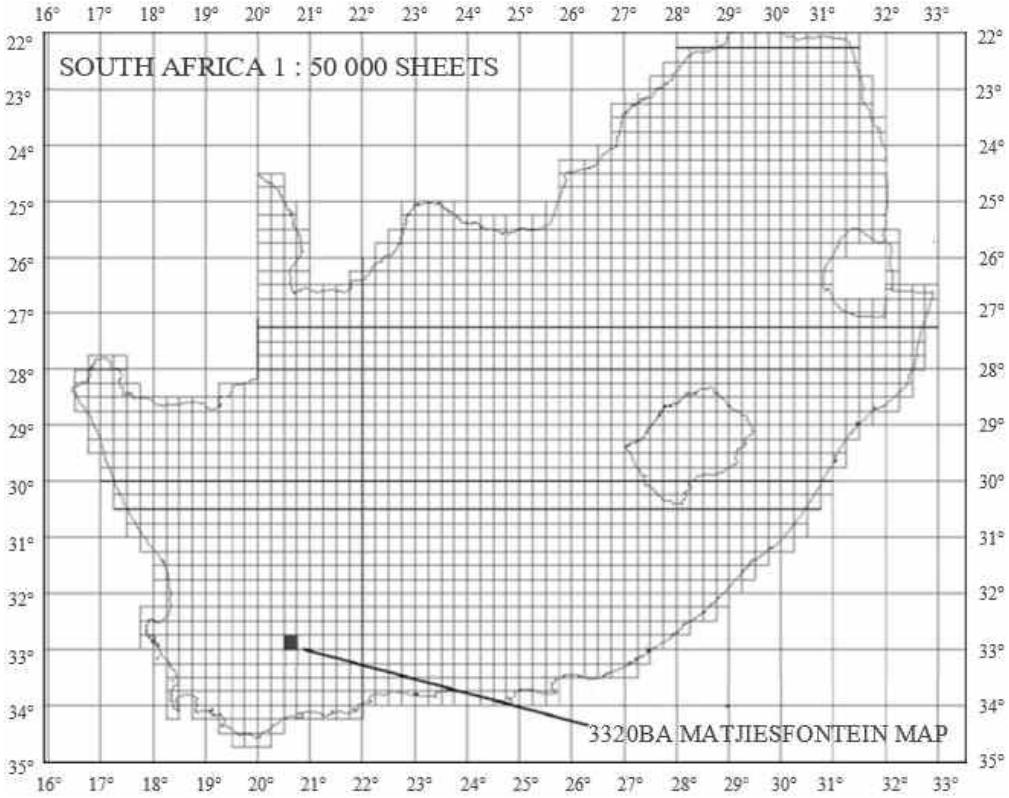

Figure 2.10: Topographic sheet layout of South Africa (Croukamp et al., 2014).

2.3.2 Climate

Temperature

Matjiesfontein has a continental semi-desert climate. The climate is classified as a mid-latitude cold desert sub-type (BWk) according to the Köppen-Geiger-Pohl system (Augustyn et al., 2018). Measured historic data is difficult to come by, since Matjiesfontein does not have a reliable weather station. The closely situated Laingsburg station reported mean annual minimum and maximum temperatures of 9 $°C$ and 23 $°C$, respectively (Laingsburg Municipality, 2017). Although the temperature appears fairly moderate from mean annual values, it is not uncommon for temperatures to fall below 0 $°C$ during the winter.

Precipitation

Matjiesfontein experiences many cloudless days. The Laingsburg station reported a mean annual rainfall of 110 mm with the highest rainfall occurring between March and June (Laingsburg Municipality, 2017). Although they seldom occur, flash flood events have been reported in the past, where the Lord Milner hotel was submerged knee-deep in water (L. Croukamp, pers. comm., 2019). As shown in Figure 2.11, the Weinert N-value of the area is greater than 5, which indicates that the ratio of evaporation to precipitation is high; hence, the area is relatively dry. For that reason, physical disintegration is the dominant mode of weathering.

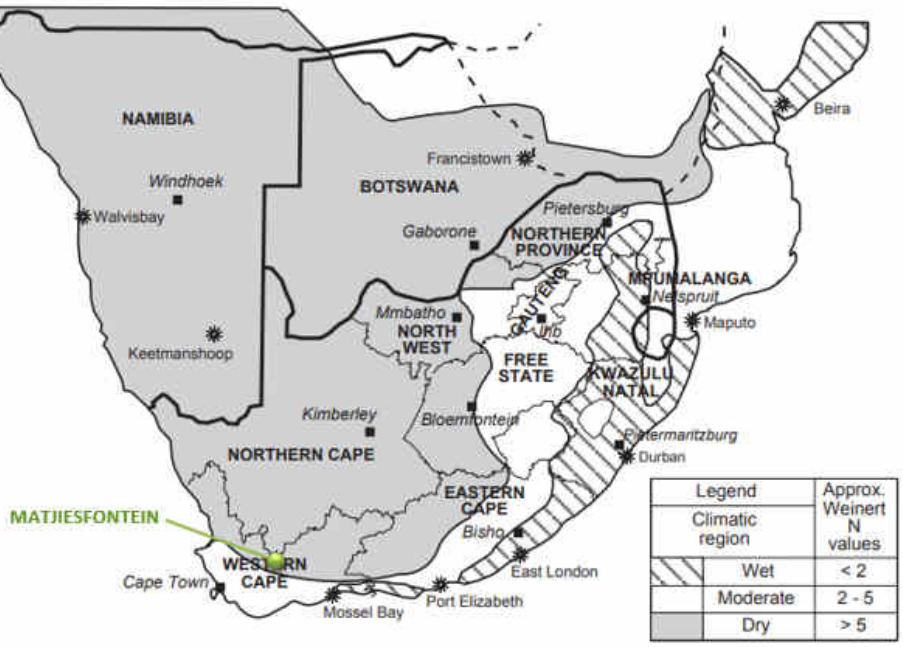

Figure 2.11: Climatic regions of southern Africa (Weinert, 1980 cited in TRH3, 2007).

Wind

A wind rose, which indicates the number of hours per year that wind blows from a certain direction, is displayed in Figure 2.12, which indicates that the wind blows mainly from the north-west or south-east directions. Maximum wind speeds range between $38 - 50$ km/h. However, the diagram is based on hourly simulated data that extends over 30 years and has a spatial resolution of approximately 30 km (Meteoblue, 2018). Consequently, they may not account for extreme local conditions.

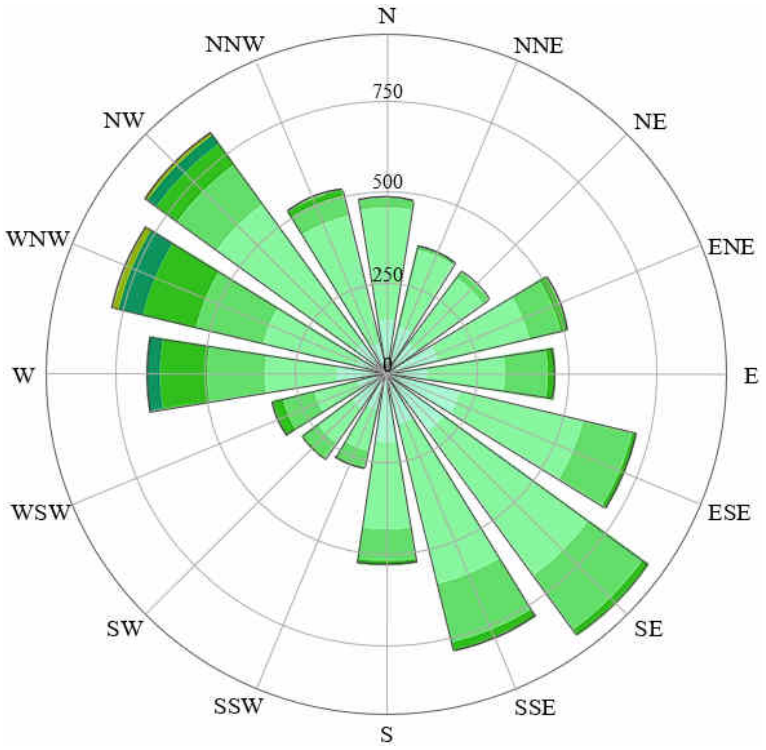

Figure 2.12: Hours per year that wind blows from a certain direction at Matjiesfontein (adapted from Meteoblue, 2018).

As before, weather data from Laingsburg was deemed representative. Recent wind conditions determined by Kruger, Retief and Goliger (2017) for SANS 10160-3 indicate that the design wind speed (v_{b_0}) for wind gusts at Laingsburg is 40 m/s. This translates to 144 km/h, a speed that may induce significant cross-wind response in large dishes.

2.3.3 Geology

The site is located slightly north of the Cape Fold mountains, where the Dwyka Group of the Karoo Supergroup meets the Witteberg Group of the Cape Supergroup. The main lithologies that have been identified are shale, sandstone, quartzitic sandstone, quartzite and tillite.

Tillite is the predominant lithology of the new site area. It is sedimentary rock that formed through the lithification of glacial deposits known as till. It has been used extensively in

construction in South Africa, especially in Natal. According to Van Wyk (2013), it is the second most durable lithology at Matjiesfontein after quartzite. Further information on the geology of Dwyka tillite is included in Section 2.4.

2.3.4 Topography

The proposed site area is located on a slightly undulating landscape. As shown in Figure 2.13, the area is relatively flat, although vertical features have been exaggerated by a factor of 3. It contains a small river, which is fed by numerous smaller tributaries and runs towards the east on the contact between Dwyka sequences D3 and D4 (see Section 2.4.2). The river is non-perennial, flowing mainly during the previously mentioned flash flood events.

Figure 2.13: Drone image of the site area with vertical features exaggerated by a factor of 3.

The site contains a 1.2 km unpaved airstrip, which runs along and slightly north of the river. The ground elevation increases slightly from the river towards the north. Potential line-of-site obstructions are limited to the Cape Fold mountains south of the airstrip and a small isolated hill at the eastern end of the airstrip.

2.3.5 Seismicity

A magnitude 3.7 earthquake was recently recorded by the MSGO seismometer (Brophy, 2015). Although no remarkable damage was caused by the event, it is important to consider the potential impact of seismic activity. Seismicity can present various challenges for radio astronomy (Eff-Darwich et al., 2010). Events may cause damage to instrumentation and supporting infrastructure, which, in addition to having major financial implications, can reduce or delay operation time significantly.

The seismic hazard of an area refers to the probability that a seismic event of a certain magnitude will occur at least once in a time period, e.g. 50 years. The seismicity of South Africa can be described as intraplate seismicity (Kijko et a.l, 2003), which occurs within tectonic plates, as opposed to interplate seismicity, which occurs between plate boundaries.

By global standards, intraplate seismicity is relatively low. A seismic hazard map of southern Africa is displayed in Figure 2.14. The map is based on a database of natural and mining-induced seismic events from the year 1620 to December 2000 (Kijko et al., 2003). The peak ground acceleration (m/s^2) with a 10 % probability of being exceeded at least once in 50 years is indicated. Here, acceleration is expressed in units of gravity acceleration (9.81 m/s^2). The level of hazard is indicated by colour intensity ranging from blue (low) to dark red (very high). At Matjiesfontein, the peak ground acceleration is approximately 0.12 g, which corresponds to a moderate expected level of seismic hazard.

Seismic hazard zones were identified in SANS 10160-4 (2017) based on Figure 2.14. Two different types, namely Zone I and II, were delineated on the map. Structures in Zone I areas are subject to natural seismicity, whereas structures in Zone II areas are subject to natural and/or mining-induced seismicity. Matjiesfontein lies within the Zone I of the Western Cape. Structures in this area must comply with clauses 6 - 10 of SANS 10160-4 (2017).

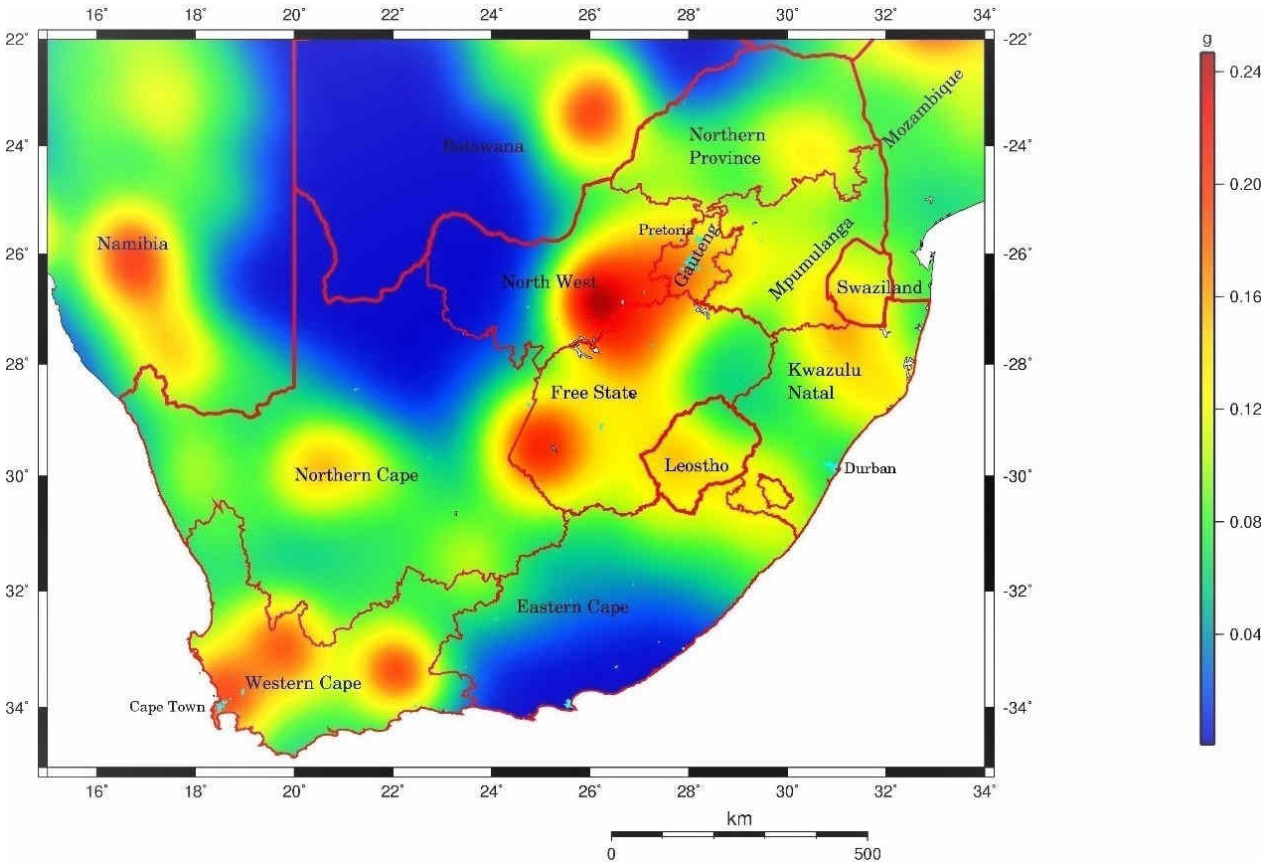

Figure 2.14: Seismic hazard map of southern Africa: Peak ground acceleration (g) with a 10 % probability of being exceeded in a 50 year period (Kijko et al., 2003).

2.4 Dwyka Tillite

2.4.1 Origin

Tillite is the most frequently occurring member of the Dwyka Group, which crops out more than than 10% of southern Africa (Paige-Green, 1984), as displayed in Figure 2.15. The Dwyka Group was deposited 320 - 360 million years ago during the late Carboniferous and early Permian periods (Dunlevey and Stephens, 1995) and it is the oldest layer in the Karoo Supergroup (Brink, 1983).

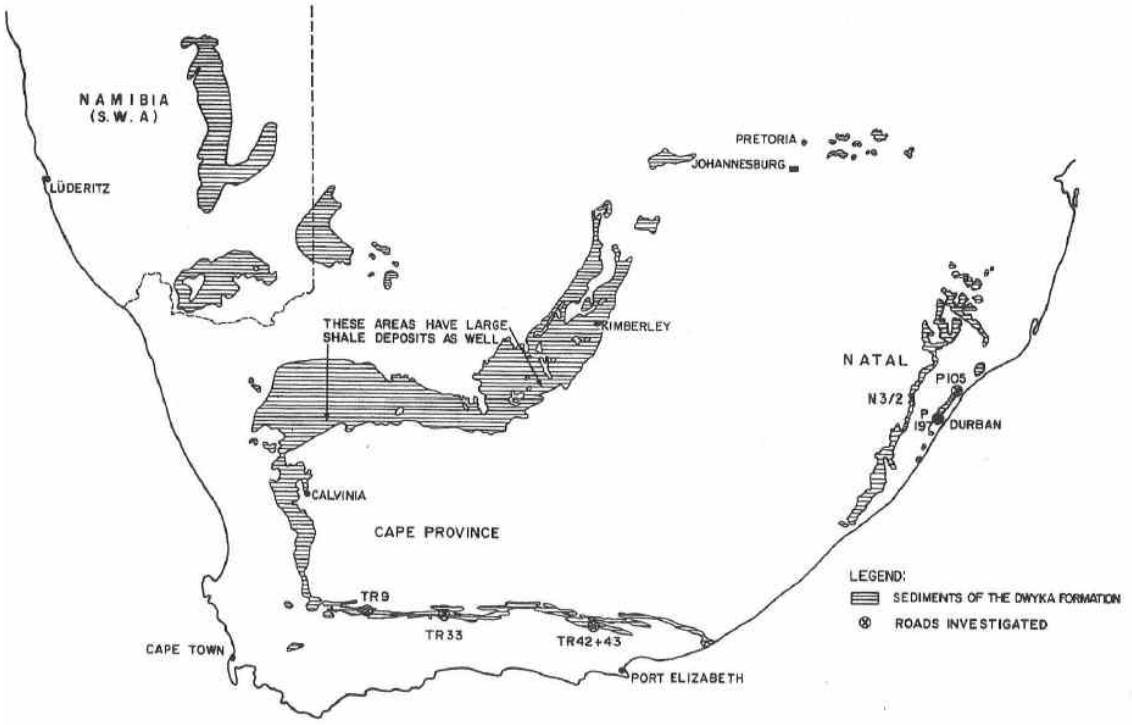

Figure 2.15: Distribution of the Dwyka Group in southern Africa (Paige-Green, 1984).

The most frequently occurring member of the Dwyka Group is diamictite, or more specifically, tillite, which is diamictite that was formed through glacial deposition. Continental drift drove the part of Gondwanaland that is now South Africa across the frigid zones of Earth (Dunlevey & Stephens, 1995). At the time, the southern portion of South Africa was sunk below sea level. Massive glacial ice sheets started to flow out to open water, eroding the substrate on their way to the sea through glacial action, as illustrated in Figure 2.16.

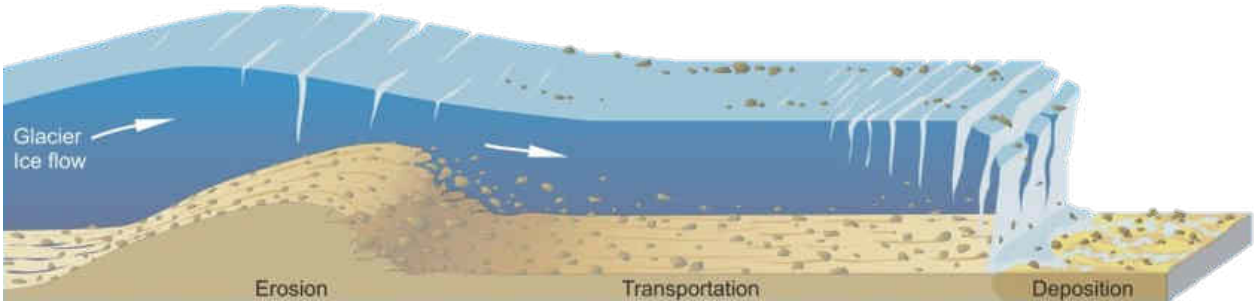

Figure 2.16: Glacial erosion and deposition (Jebasingh, 2016).

Since glaciers have extremely viscous fluid, they have great capacity and competence for the transportation of sediment (Schoneman, 2018). As the ice thawed during glacial retreat, sediment was deposited beneath the glaciers. These unsorted glacial deposits, known as till, underwent lithification and transformed into the sedimentary rock, tillite. Although the main area of erosion was where glacial ice started to float (Dunlevey & Stephens, 1995), the glaciers covered great distances over highly variable substrate. As a result, the particle composition of tillite is variable from location to location and is dependent on its origin and distance to its depositional environment (Paige-Green, 1984).

2.4.2 Sequences

In the southern Karoo, narrow exposures of tillite dip steeply toward the north (Brink, 1983). The formation consists of 4 sequences, namely D1, D2, D3 and the youngest sequence, D4. During each sequence, glaciers advanced and retreated across the Karoo basin. This occurred due to major changes in sea level over long time periods. As the sea level dropped, glacial ice advanced toward the sea, during which no sediment was deposited. While the sea level remained static or just began to rise, the ice retreated slowly inland and hard basal tillite was deposited. As the sea level continued to rise and conditions became less stable, the ice retreated at a faster rate and upper layers of softer and stratified tillite was deposited.

As the sea level eventually dropped, the ice advanced again, reworking the underlying soil and marking the beginning of the next sequence. Since climatic conditions and ice flow patterns varied throughout the formation of the Dwyka Group, the sequences have different characteristics, as illustrated on the cross section in Figure 2.17 (after Visser, 1992 and Visser et al., 1997 cited in DeVille-Wickens and Cole, 2017). Overlying shale and siltstone of the Waaipoort Formation, D1 consists of clast-poor tillite at the base and a boulder beds of 2 m thick at the top of the sequence.

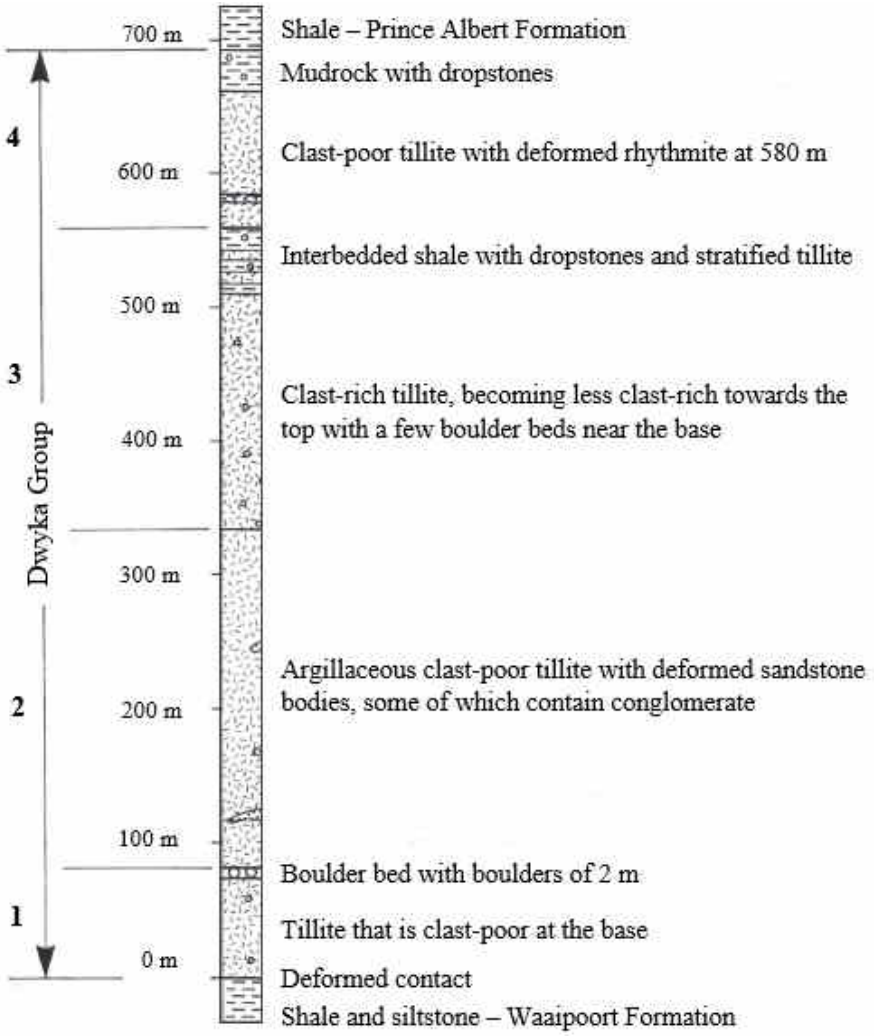

Figure 2.17: Cross section through the sequences of the Dwyka Group 6 *km* south of Laingsburg (DeVille-Wickens and Cole, 2017).

D2 consists of a argillaceous (clayey), clast-poor tillite with isolated deformed sandstone bodies. According to DeVille-Wickens and Cole (2017), D2 has a relatively low resistance to weathering. Sequence D3 consists of massive tillite overlain by alternating beds of shale with sparse dropstones and stratified tillite. D3 is clast-rich at the base and becomes less so toward the top, where it is clast-poor with the exception of concentrated clast lenses.

Overlying the shale of D3, D4 consists of clast-poor tillite with dropstone-bearing mudrock at the top. Note that layer thickness may vary from one location to another, since either the basal part or upper part of a sequence is often missing (DeVille-Wickens and Cole, 2017). Outcrops of the sequences around Matjiesfontein are illustrated in Figure 2.18 along with the proposed site area of the telemetry dishes. Based on Figure 2.18, the site area is underlain by sequence D3.

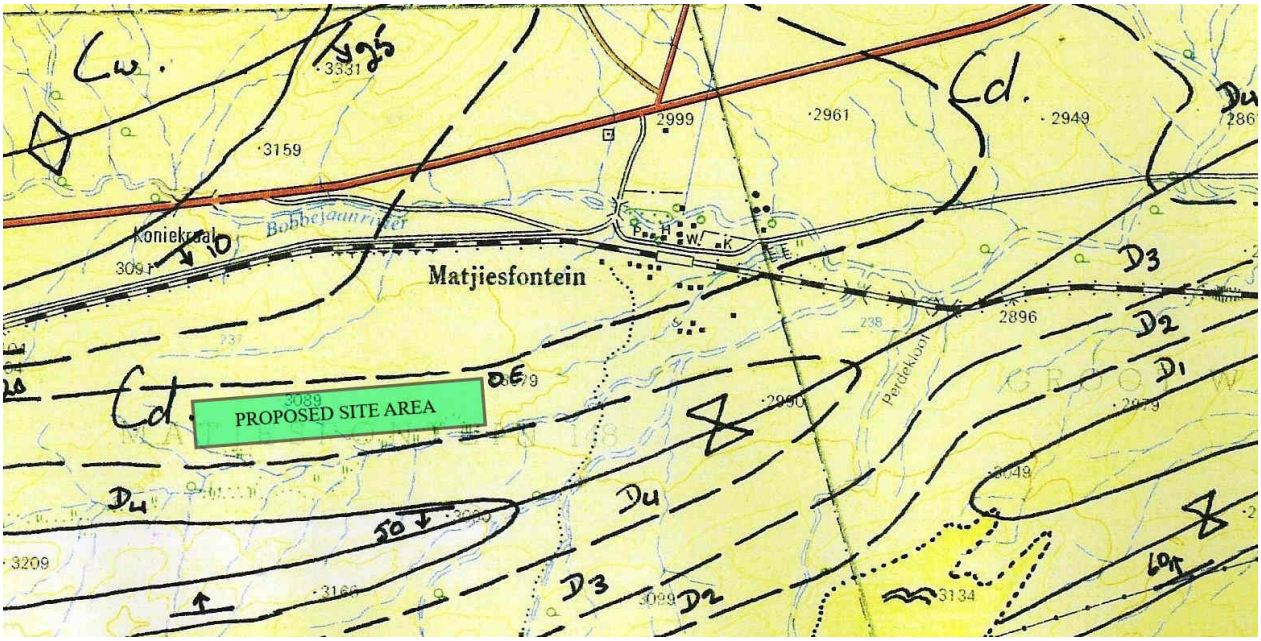

Figure 2.18: 1:50 000 field sheet with surface outcrops of sequences indicated (DeVille-Wickens, n.d.).

2.4.3 Characteristics

In its fresh state, tillite is blueish grey in colour, as shown in Figure 2.19. The colour is caused by its concentrated iron content (Paige-Green, 1980a). Upon extended exposure to the atmosphere, the colour is reduced to a yellowish brown by weathering processes.

Figure 2.19: Fresh blueish grey tillite exposed by excavation at the turn-off into Matjiesfontein.

According to Brink (1983), the most useful classification of tillite is according to degrees of weathering:

- **W1 - Unweathered:** completely fresh blueish grey tillite; very hard (70 MPa - 200 MPa) rock.
- **W2 - Slightly weathered:** Similar to W1; stained brown on discontinuity planes.
- **W3 - Medium weathered:** Stained brown throughout; hard (25 MPa - 70 MPa) to soft (3 MPa - 10 MPa) rock.
- **W4 - Highly weathered:** Stained yellow, pink or white; original structure retained; soft (3 MPa - 10 MPa) to very soft (1 MPa - 3 MPa) rock.
- **W5 - Completely weathered:** Stained dark brown to black; gravelly residual soil with little to no inherited fabric; soft, firm/stiff or loose gravel.

Furthermore, tillite is not associated with a specific fracture pattern, although it is usually well jointed (Brink, 1983). The rock possesses a bimodal size distribution, consisting mostly of gravel/pebble-sized particles that are set in a matrix of fine silt/clay-sized particles (Paige-Green, 1984). It contains clasts of various rock types, of which the larger inclusions are most frequently identified as granite and the smaller inclusions as polymictite (DeVille Wickens and Cole, 2017). Less dominant coarse particle constituents such as quartzite and gneiss are also common. The fine particle matrix typically consists of ground quartzite, feldspar and clay minerals.

According to Paige-Green (1984), the composition of clay minerals in the matrix is crucial, as it influences important engineering properties. Despite its overall variability, X-ray diffraction and electron microscope techniques revealed that the clay mineralogy of tillite is remarkably consistent (Paige-Green, 1980a). From 16 samples collected from various locations across southern Africa, it appeared that chlorite is the predominant clay mineral. Illite/mica, although subordinate, was also common. Smectite and kaolinite were occasionally encountered in small quantities.

The main clay minerals were formed prior to or during the lithification process, whereas smectite and kaolinite were formed through weathering and hydrothermal processes, respectively. One of the samples from this study was collected from Laingsburg. Considering that the clay mineralogy is remarkably consistent, the sample description, as displayed in Table 2.1, should provide a good indication of the clay mineralogy of tillite at Matjiesfontein.

Table 2.1: Clay mineralogy of tillite from Laingsburg (Paige-Green, 1980a).

Total % of clays present				Sample Description
Chlorite	Illite/Mica	Smectite	Kaolinite	
> 50 %	20 - 50 %	not identified	< 5 %	Medium dark grey (N4), very hard

2.4.4 Utilization in South Africa

A comprehensive study was conducted on the use of tillite in flexible pavements in southern Africa (Paige-Green, 1984). The suitability of tillite was considered for each layer of a typical flexible pavement structure, as displayed in Figure 2.20. The findings are summarized briefly in the following sub-sections.

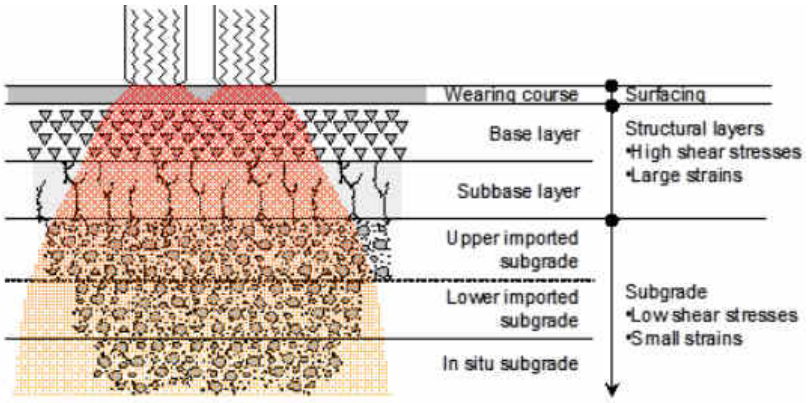

Figure 2.20: Typical layers of flexible pavements (SANRAL, 2014).

Gravel Wearing Course

The gravel wearing course (surface course) is the top layer of a typical flexible pavement. As a surface layer, it must endure direct contact with traffic. Therefore, it is usually composed of high-quality materials. According to Paige-Green (1984), highly weathered tillite (W4) is suitable for use in gravel wearing courses, as long as the plasticity is between 8 and 14. Higher plasticity could lead to hazardous road traction losses in wet conditions.

Base Course

The base course is located directly underneath the surfacing and aids in the distribution of concentrated surface loads, which reduces the impact on lower layers to acceptable levels. Both unweathered (W1) and slightly weathered (W2) tillite with less than 20 % discolouration has been used in unstabilized base courses in roads that carry up to 4000 vehicles per day. Extra care should be taken with drainage to ensure that the base course is not excessively exposed to moisture, as this could cause the tillite to break down (Paige-Green, 1984). During a survey of roads constructed with tillite, only 1 out of 56 sites exhibited a rut depth of more

than 10 mm, while no other sites required major rehabilitation. Furthermore, it is noted that existing standard material specifications are too stringent (Paige-Green, 1984), especially for low volume roads in dry areas, which would be the case for MSGO access roads, for example.

Sub-base Layers

Sub-base layers are placed underneath base layers to aid in load distribution and to improve drainage. According to Paige-Green (1984), unweathered (W1) and slightly weathered (W2) tillite has been used in sub-bases of roads that carried up to 10 000 vehicles per day.

Selected Subgrade

Highly weathered (W4) tillite has proved to be suitable for use in selected subgrade, as adequate CBR strengths are usually obtained with minimal reworking/compaction. Where this is not the case, CBR values higher than 100 % could be achieved by stabilizing W4 tillite with 2 % lime (Paige-Green, 1984), as shown in Table 2.2.

Table 2.2: Effect of 2 % lime stabilization on highly weathered (W4) tillite cured for 7 days, soaked for 4 days and compacted to 100 % Mod. AASHTO density (Paige-Green, 1984).

Sample	Plasticity Index	CBR before stabilization (%)	CBR after stabilization (%)
1	6	37	150
2	9	10	110
3	5	100	250
4	7	16	140

Concrete Aggregate

Despite the problems that have been encountered with tillite in roads, it makes an excellent concrete aggregate (Paige-Green, 1980b). Tillite has been used extensively as concrete aggregate in South Africa, especially in Natal – it was estimated that approximately 40 % of the concrete in Durban was manufactured using tillite (Addis and Owens, 2001). However, its success depends on the composition of the rock at the source location.

While the water absorption of fresh tillite is well below 1 %, the range of drying shrinkage is relatively high. Therefore, the material should be used with caution where shrinkage is a major concern, e.g. pre-stressed concrete (Dunlevey and Stephens, 1995). The water absorption and drying shrinkage of tillites are closely related to its mineralogy and normally increases with the degree of weathering and the development of clay minerals. Dunlevey and Stevens (1995) concluded that the material properties of tillite are adequate for aggregates in most cases, while it could be regarded as marginal in some cases. Detailed testing is recommended for the identification of localized zones of poorer quality material.

2.4.5 Potential Problems

Chemical Weathering

Although the clay matrix is very dense, the cohesion is not due to cementation, but to strong bonds between the clay minerals. Pores are formed around larger grains due to the lack of cementation. Since the pores are seldom interconnected, tillite is highly impermeable, which in turn delays the onset of chemical decomposition. However, once decomposition has started, it progresses rapidly (Paige-Green, 1980b). The rate of decomposition can be accelerated by crushing, as a greater surface area is exposed to reactive chemical agents. Furthermore, it was discovered that the decomposition of chlorite clays in tillite produces smectite, a highly expansive clay. Since prolonged exposures to moisture are usually required for excessive alteration to occur (Paige-Green, 1980b), semi-desert areas such as Matiesfontein should be exempt from deleterious quantities of smectite.

Water Absorption and Drying Shrinkage

Tillites have variable water absorption and drying shrinkage due to its clay mineralogy. The primary clay minerals of glacial deposits were not altered significantly when sediment was consolidated into rock (Dunlevey and Stephens, 1995) and, as mentioned previously, the clay matrix is susceptible to alteration. The number of clay minerals and ferric hydroxides increases in accordance with the degree of weathering. As a result, water absorption and drying shrinkage is least for fresh tillite and increases significantly as chemical weathering progresses (Dunlevey and Stephens, 1995). Thus, if the colour of the tillite has changed from a blueish grey to brown, higher water absorption/drying shrinkage values can be expected.

Physical Disintegration

At certain locations, rapid disintegration of tillite has been observed upon exposure to the atmosphere. According to Paige-Green (Paige-Green, 1980b), the phenomenon is primarily physical, since it is caused by shrinkage/expansion of the clay matrix due to repeated wetting and drying rather than oxidation. The resulting material is typically pockets of small ($1 - 2\ cm$) blocky fragments within an otherwise solid material of the same colour.

Subsequent to these observations, the use of tillite in road construction decreased significantly. In contrast, they have not affected its use in concrete, since concrete aggregates are isolated from moisture variations and other agents that cause the phenomenon (Paige-Green, 1980b). Although degrading tillite has not proven to be very harmful, more expensive alternatives are often used in its place to avoid the risk. Tillite that contains significant quantities of expansive clay, e.g. smectite, is particularly susceptible to disintigration.

In wet regions where the Weinert N-value is below 5 and chemical decomposition is the main weathering mode, increased alteration leads to higher quantities of expansive clay. Although instances of degrading tillites have been encountered in some dry regions, e.g. Seeheim (Namibia), they are mostly associated with wet regions, especially Natal (Paige-Green, 1980b). Results of laboratory tests that were performed on known degrading tillites from Durban and Seeheim are shown in Table 2.3. In addition, the corresponding results of known durable tillites were included for comparison; note that the values given in parentheses represent the number of durable samples that were tested.

Of the tests performed, the Washington Degradation test appeared to be the most reliable indicator of degrading tillites (Paige-Green, 1980b). While the Aggregate Crushing Value (AVC) test was not a reliable indicator, the soaked to dry ratios of 10 % Fines Aggregate Crushing Value (10%FACT) tests were more successful. Furthermore, while similar values were obtained for the apparent specific gravity of durable and degrading tillites, they could be differentiated using the values obtained for bulk specific gravity and water absorption. Overall, it appears that most of the more reliable indicator tests involve the addition of moisture and shrinkage/expansion of the clay matrix.

Table 2.3: Test results of unweathered degraded, intact and durable tillites (Paige-Green, 1980b).

Sample	Location	Description	ACV (%)	10%FACT			Washington Degradation Value	Apparent Specific Gravity	Bulk Specific Gravity	Water Abs. (%)
				Dry (kN)	Soaked (kN)	S/D (%)				
6680	Durban	Degraded, blocky tillite	31	126	43	34	3	2,71	2,51	3,0
6681	Durban	Intact tillite, no visible cracks	31	101	31	31	9	2,67	2,49	2,9
7313	Seeheim	Degraded, blocky tillite	17	248	177	71	65	2,71	2,45	4,2
7314	Seeheim	Intact tillite, no visible cracks	19	210	119	57	45	2,71	2,48	4,2
Various	RSA and Namibia	Intact, hard, durable tillite	14-20 (5)	213-269 (10)	160-267 (6)	65-92 (6)	67-87 (10)	2,70-2,73 (8)	2,63-2,69 (8)	0,3-1,3 (8)

2.4.6 Recommended Solutions

Since durability is the main concern, recommended solutions are aimed at identifying and eliminating non-durable tillites. The 1976 SABS specifications for base course aggregates were modified for tillites by Weinert (1980). According to Paige-Green (1980b), these specifications failed to eliminate all instances of degrading tillites. The modified specifications in Table 2.4 were suggested based on existing roads with known performance. Here, the dry bulk specific gravity should not be less than 2.6, the water absorption should not exceed 2.0 %, the

10% FACT value should not be less than 200 kN and the ratio of soaked to dry 10% FACT values should not be less than 70 % in moist areas or 56 % in dry areas.

Table 2.4: Recommended specifications for use of tillite as base course aggregates (Paige-Green, 1980b).

Property	Moist Areas (N < 2)				Dry Areas
	Base		Subbase		(N > 2)
Vehicles per day	1000 - 4000	< 1000	1000 - 10 000	< 1000	< 1200
(approx % heavy***)	(10)	(5)			
Estimated E80/day	460	36	1200	36	180
Max. size (mm)	19,0 - 37,5	19,0 - 37,5	26,5 - 37,5	63	37,5
% < 0.075 mm	5 - 17	5 - 17	5 - 12	< 25	5 - 16
Max. liquid limit (%)	26	26	26	35*	28
Max. plasticity index (%)	13	13	6	13*	13
Max. Bar Linear shrinkage (%)	4	4	2	4	4
Min. 98% Mod. AASHTO soaked 2.54 mm CBR (%)	100	80	80	70	80
Max. flakiness index	45**	-	-	-	-
10% FACT (kN)	200	180	110	-	200
Min. ratio soaked/dry 10% FACT (%)	70	70	70	-	56
Min. Washington degradation value	60	55	50	50	-

* Provided the material is stabilized. Values are before stabilization.
** Provided the 10% FACT specification is met; if not, discard.
*** Heavy vehicles = axle load > 15 kN. All vehicle counts are both directions.

In addition to the Washington Degradation test, several other widely implemented methods are available for the evaluation of durability, such as the Durability Mill Index (DMI) and slake durability tests. The DMI test is typically used for the evaluation of aggregates used in road layers (SANS 3001-AG16, 2013), as it allows for the identification of materials that carry a risk of degradation due to traffic loading and wet conditions. The method involves rotating field samples in a steel cylinder under 3 conditions, namely "dry with steel spheres", "wet without steel spheres" and "wet with steel spheres". The DMI is calculated as the product of the highest individual fines content and Plasticity Index recorded for material passing the 425 μm sieve.

The slake durability method involves the rotation of material in bins made from 2 mm wire mesh for two standard wet and dry cycles (ASTM D4644-16, 2016). The durability index is calculated as the mass percentage of material retained inside the bin (> 2 mm). Although the slake durability method is suitable for the measurement of slaking into clay or silt sized particles, it may not be suitable for the measurement of physical disintegration (Brink, 1983), e.g. disintegration of tillite into 2 cm blocky particles. In this case, the slake durability test implemented by Venter (1980 cited in Brink, 1983) can be used for the qualitative evaluation of breakdown into various shapes and sizes.

Venter's method was used to evaluate and compare the durability of tillite, quartzite, sandstone and shale from Matjiesfontein (Van Wyk, 2013). As shown in Table 2.5, quartzite and tillite were indicated as the most durable materials, with less than 20 % of both samples degraded at completion of the tests. In contrast, more than half of the sandstone and shale samples were degraded.

Table 2.5: Slake durability of various Matjiesfontein rock types (Van Wyk, 2013).

Sample	Mass Retained (%)	Mass Degraded (%)
Tillite	83,5	16,5
Quartzite	89,5	10,5
Sandstone	31,9	68,1
Shale	41,7	58,3

2.5 Foundation Engineering Properties

2.5.1 Concrete Aggregates

Aggregates are mixed with water and cement in the production of concrete. They are the most utilized materials in the world after water and soil and, according to Alexander and Mindess (2005), roughly 25 – 35 % of all aggregates are used in concrete, which usually consists of approximately 70 % aggregates by volume (Owens, 2013). Most aggregates are derived from natural sources, i.e. rock that has been broken down either naturally through weathering or artificially through crushing (Addis and Owens, 2001).

Initially, concrete aggregate was defined as an inert filler material with the purpose of providing dimensional stability and reducing manufacturing costs. However, it also has a major influence on the characteristics and behaviour of fresh and hardened concrete (Addis and Owens, 2001; Alexander and Mindess, 2005). For example, the addition of aggregate can reduce shrinkage by approximately 10 – 15 % (Alexander and Mindess, 2005). Additionally, its high stiffness relative to cement paste causes it to restrict movement and reduce creep. Aggregate also increases concrete durability, provided of course that the material meets appropriate specifications.

In contrast with the interactions mentioned above, aggregates may also interact poorly with other concrete constituents. If only cost is considered during the selection process, it may ultimately result in the production of a more expensive concrete with undesirable qualities (Addis and Owens, 2001). Therefore, it is prudent that aggregate characteristics are analysed thoroughly when determining its suitability for use in concrete. Aggregates are classified into two classes according to particle size, namely sands and stones. Sands are fine aggregates that pass through a 4.75 mm square aperture sieve and are retained on a 0.075 mm sieve. Stones are coarse aggregates that are retained on a 4.75 mm square aperture sieve (Addis and Owens, 2001). Although fine aggregates are occasionally discussed for context, this section of the Literature Review is focused mainly on the characterization and testing of *coarse* aggregates from *natural* sources, as it applies to the Goals and Objectives specified in Section 1.4. The following 9 characteristics are used to ensure the suitability of aggregates for different applications (Owens, 2013):

1. Grading
2. Bulk density
3. Particle relative density
4. Particle shape

5. Shrinkage
6. Strength
7. Surface texture
8. Geological type
9. Alkali reactivity

Grading

Grading refers to the particle size distribution of the aggregate. Coarse aggregates in South Africa are usually characterized with a single nominal size. The particle size distribution of coarse aggregate does not have a significant influence on the workability of concrete. In contrast, the grading of sand aggregates must ideally exhibit a good representation of all size fractions. The smaller size fraction is especially important, since a deficiency of very fine material may lead to bleeding and segregation in fresh concrete.

Although the workability of concrete is not affected significantly by the particle size distribution of coarse aggregates, it is affected by the selected nominal stone size (Owens, 2013). For example, a larger nominal size is associated with a lower water requirement, as illustrated in Figure 2.21 for air-entrained and non-air-entrained concrete. Here, both types of concrete required less water in order to achieve the same level of workability when a larger maximum nominal stone size was used (Kosmatka et al., 1995 cited in Alexander and Mindess, 2005).

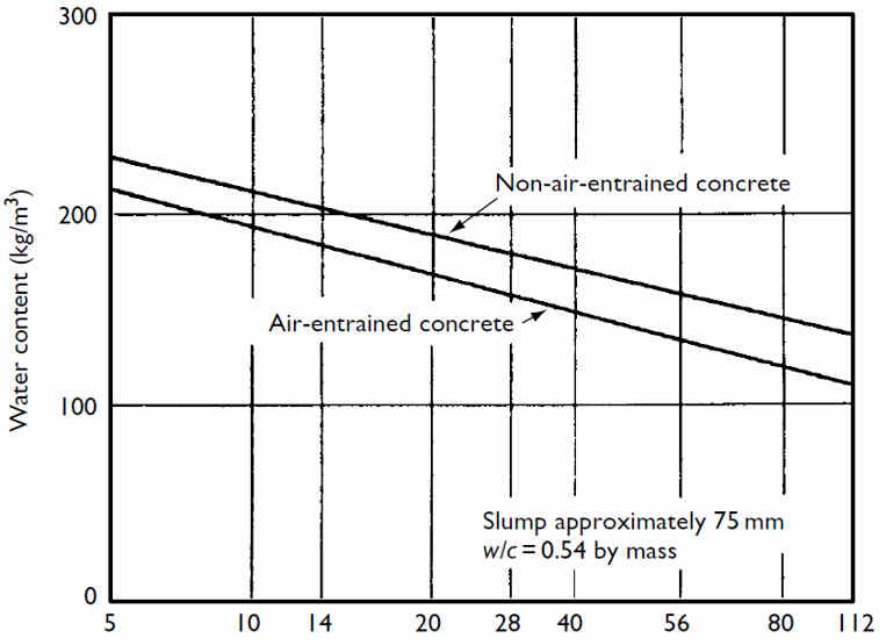

Figure 2.21: Relationship between concrete water requirement and the maximum nominal stone size for air-entrained and non-air-entrained concrete (Kosmatka et al., 1995 cited in Alexander and Mindess, 2005).

Bulk Density

Bulk density is the mass of aggregate that fills a 1 m^3 container. Two different methods exist for the calculation of bulk density (Owens, 2013), namely the loose bulk density, which is used for volume batching, and the compacted bulk density, which is used in the design of concrete mixes. In addition to the degree of compaction, the bulk density is influenced by aggregate characteristics such as the grading, particle relative density and particle shape. For example, a well graded, dense material with rounded particles has a higher bulk density than a poorly graded, low density material with angular particles. According to Owens (2013), a higher bulk density leads to a lower water requirement, which in turn leads to lower permeability, lower shrinkage and higher durability in hardened concrete.

An example of the effect of bulk density on the properties of concrete is shown in Figure 2.22. Here, numerous concrete cylinders were prepared using either crushed stone (SC) or crushed brick (CB) as aggregate (Iffat, 2015). A constant mix proportion was maintained for all specimens. The densities and compressive strengths of both types were tested after 21, 24, 28, 29, 30, 32, 34, 36, 40, 42, 45 and 56 days. Figure 2.22 shows that crushed stone, which possessed higher loose and compacted bulk densities (Table 2.6), also exhibited a higher range of compressive strengths.

Table 2.6: Loose and compacted bulk densities of crushed stone and crushed brick aggregate (Iffat, 2015).

Aggregate	Loose Bulk Density (kg/m³)	Compacted Bulk Density (kg/m³)
Crushed stone (SC)	1460	1590
Crushed Brick (SB)	980	1170

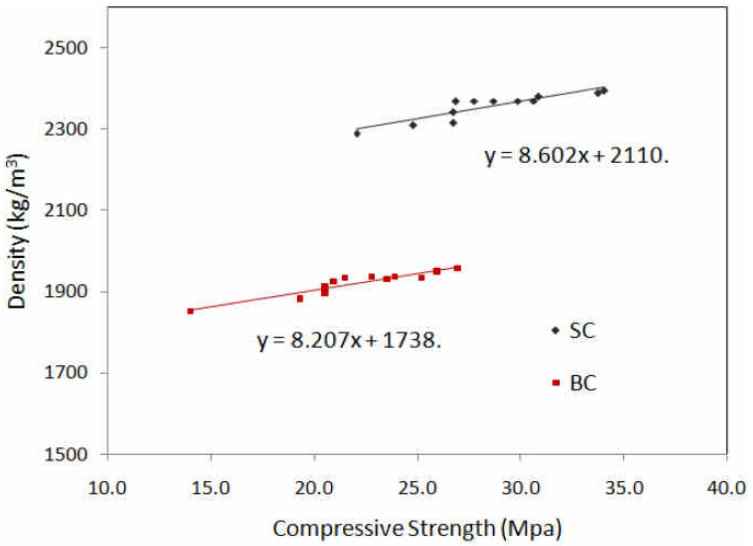

Figure 2.22: Relationship between bulk density and compressive strength for concrete cylinders prepared using crushed stone (SC) and crushed brick (BC) (Iffat, 2015).

Particle Relative Density

Particle relative density, also known as specific gravity, refers to the ratio of particle density to the density of water. The risk of segregation in fresh concrete is increased by coarse aggregates that possess higher particle relative densities and larger stone sizes (Alexander and Mindess, 2005). For example, a relatively high particle density could result in aggregates accumulating towards the bottom of a structure, as shown in Figure 2.23. The particle relative densities of concrete aggregates normally range between 2.5 and 3.0 and the workability of a concrete mix may be affected adversely by aggregates that do not fall within the normal range (Addis and Owens, 2001); these aggregates also carry a higher risk of segregation. The relative density of the tillite at Matjiesfontein was determined as 2.66 by Van Wyk (2013) and as 2.70 by Janse van Rensburg (2017), both of which fall within the normal range.

Figure 2.23: Concrete segregation due to high particle relative density coarse aggregate (Harikrishna, 2018).

Particle Shape

Particles can be classified as combinations of spherical or elongated and angular or rounded depending on their shape. Particle shape strongly affects the water requirement of fresh concrete, since more water is required for the increased surface areas of flaky particles. Consequently, it is the most important factor to be considered for aggregates in fresh concrete (Addis and Owens, 2001). Flakiness is known to cause higher permeability, higher shrinkage and lower durability (Owens, 2013).

Various quantitative methods exist to analyse particle shape, e.g. the Flakiness Index (FI) method. An example is shown in Figure 2.24. Here, concrete specimens were cast using varying percentages of flaky particles and tested for compressive strength, for which the

estimated target value was 31.6 MPa (Khan and Dhobale, 2018). The study indicated that an increase in flaky particles resulted in a decrease in compressive strength. Furthermore, the target strength of 31.6 MPa was not reached by specimens with FI's of 30 % or more (Khan and Dhobale, 2018).

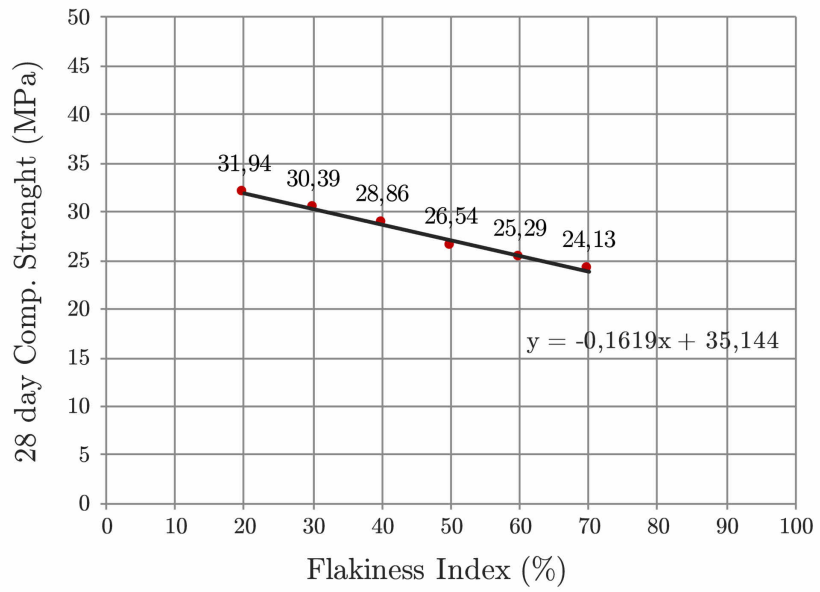

Figure 2.24: Effect of flaky particles on concrete compressive strength (after Khan and Dhobale, 2018).

There are three factors that could have a large influence on the particle shape of coarse aggregates, namely the type of rock, type of crusher and the operation of the crusher (Brown and Marek, 1996). For example, the Natal tillite aggregates vary widely due to the nature of the clasts, since they are generally more resilient than the fine-grained matrix and the rock tends to break around (not through) the clasts (Dunlevey and Stephens, 1995). Hence, angular clasts cause the rock to splinter when crushed. Impact type crushers tend to produce cube-shaped particles, while compression type crushers, such as jaw or cone crushers, are more inclined to produce flaky particles during the crushing of certain rock types.

Fortunately, the number of flaky particles can be minimized through good practices. It is recommended that several stages of crushing be implemented, as it is known to produce more cube-shaped particles (Brown and Marek, 1996). Choke-feeding the crusher by making sure the supply of material to the crusher is full and consistent can also improve particle shape, since the aggregate is broken down further through collision and interparticle friction. Furthermore, the size reduction ratio must be as low as practically possible, especially during the final stages of crushing (Shergold, 1949 cited in Addis and Owens, 2001).

Shrinkage

As mentioned previously, the dimensional stability of concrete is increased by the addition of aggregate, as shown in Figure 2.25. Therefore, if an aggregate is not dimensionally stable, it is not an effective aggregate and may lead to cracking/deformation in hardened concrete (Owens, 2013). Shrinkage can be measured indirectly using concrete or mortar specimens.

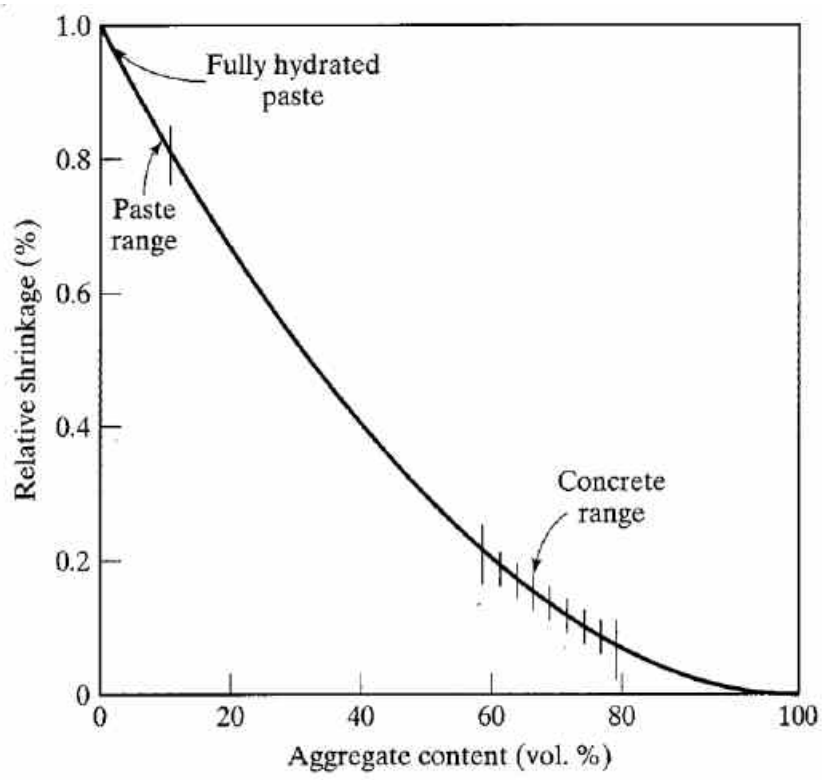

Figure 2.25: The effect of aggregate content on concrete shrinkage (Mindess et al., 2003).

Strength

Strength refers to the resistance of an aggregate to crushing. According to Owens (2013), it normally has little effect on the properties of fresh and hardened concrete as long as all requirements are met. This is mainly because aggregates are generally stronger than the concrete itself. On the other hand, if high strength concrete (say $\geq$ 60 MPa) is used, it may play a more significant role, as illustrated in Figure 2.26 (Alexander and Mindess, 2005). Note that the strength values have been normalized to compensate for varying w/c ratios. In contrast to medium strength concrete cubes (20 - 40 MPa), high strength cubes (60 - 70 MPa) exhibited a significant positive correlation (Alexander and Mindess, 2005).

Aggregate strength can be expressed through the unconfined compressive strength (UCS) of rock core specimens, as in Figure 2.26, or through the Aggregate Crushing Value (ACV) and 10% Fines Aggregate Crushing Value (10%FACT) tests. Further evidence of the effect

of aggregate strength on the performance of high strength concrete was provided in terms of the ACV, as shown in Figure 2.27 (Goldman and Bentur, 1993 cited in Alexander and Mindess, 2005). Note that a lower ACV indicates a stronger aggregate.

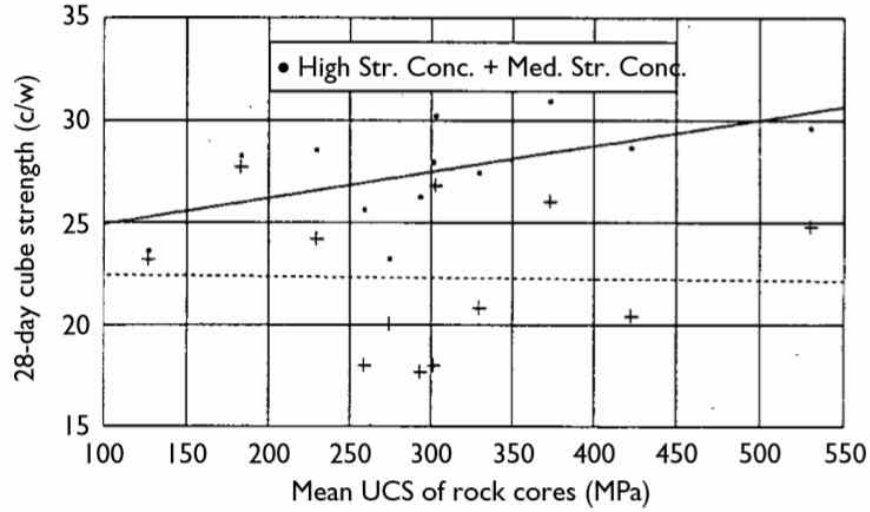

Figure 2.26: Normalized values of the concrete compressive strength plotted against respective unconfined compressive strength (UCS)values (Alexander and Davis, 1991 cited in Alexander and Mindess, 2005).

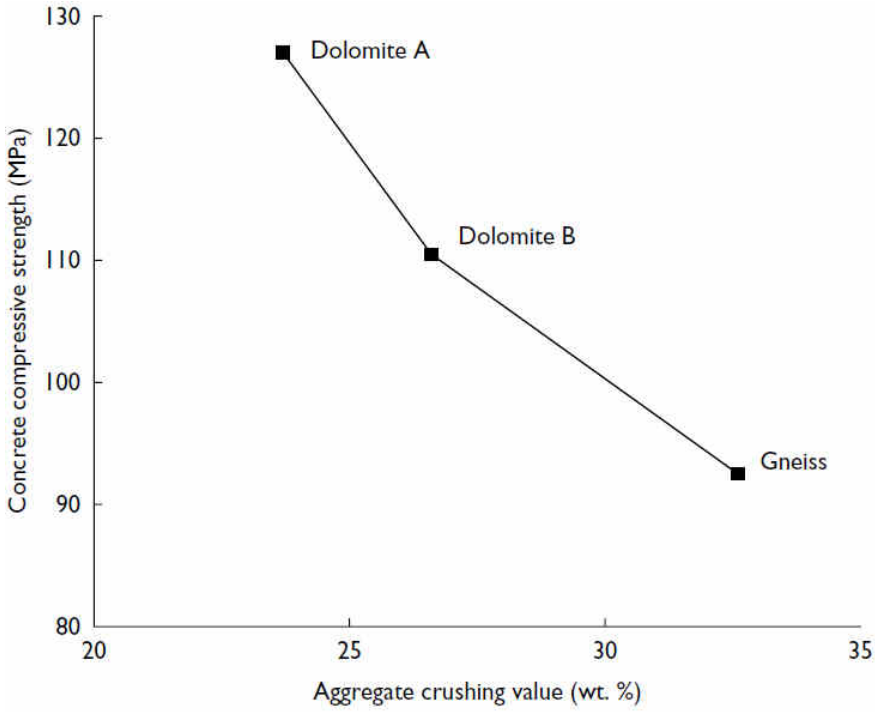

Figure 2.27: Relationship between ACV and concrete compressive strength (Goldman and Bentur, 1993 cited in Alexander and Mindess, 2005).

Surface Texture

The surface textures of aggregates are usually described in degrees of smooth or rough. While methods exist to analyse the combined effect of particle shape and surface texture, surface texture is usually described by an experienced concrete technologist (Owens, 2013). The effects of surface texture on the properties of fresh and hardened concrete, although to a lesser degree, are similar to the effects of the particle shape (Owens, 2013).

The total surface area of a rough particle is greater than that of a smooth particle of the same size. Therefore, more water is required to wet rough particles thoroughly. On the other hand, the strength of hardened concrete is increased considerably by rough aggregates due to stronger bonds with the cement paste, as illustrated in the typical example in Figure 2.28 (Alexander and Mindess, 2005); similar to aggregate strength, a greater effect is observed with high strength concrete, shown in Figure 2.28 as a dotted line.

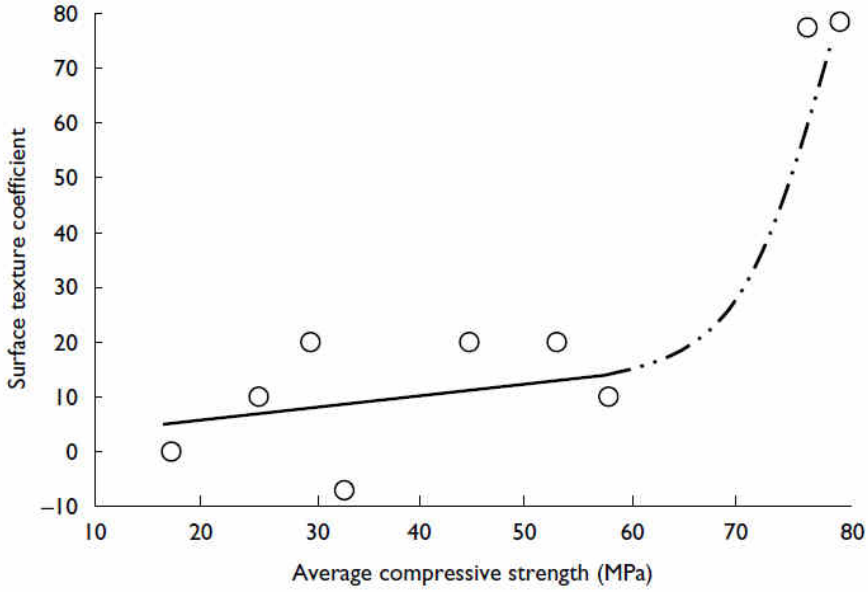

Figure 2.28: Relationship between surface roughness and concrete compressive strength (Kaplan, 1959 cited in Alexander and Mindess, 2005).

Geological Type

Practically all of the characteristics that are discussed here are inherently affected by the geological type of the aggregate. As mentioned in Section 2.4.4, tillite makes an excellent concrete aggregate in most cases, while the progression of weathering may result in unsuitable characteristics in some cases. An example of the effect of geological type is shown in Figure 2.29, where certain South African aggregates displayed similar relationships between concrete compressive strength and cement/water (c/w) ratio (Alexander and Mindess, 2005).

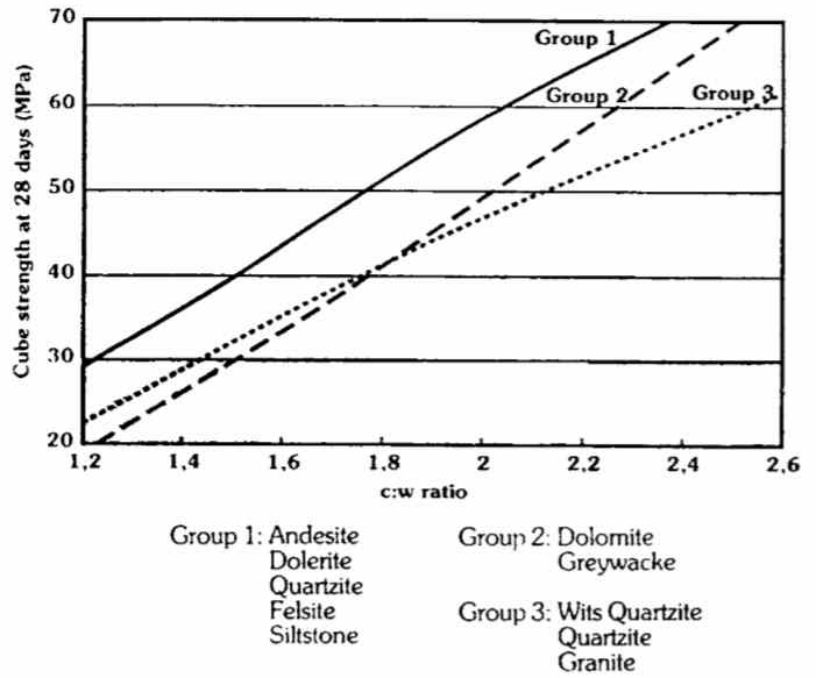

Figure 2.29: Relationship between concrete compressive strength and cement/water (c/w) ratio for various South African aggregates (Alexander and Davis, 1991 cited in Alexander and Mindess, 2005).

Alkali-Silica Reactivity

Alkali-Silica Reactions (ASR's) refer to reactions between pore solution alkalis from cement paste and chemically unstable forms of silica that are present in some concrete aggregates (Alexander and Mindess, 2005). The reactions result in the formation of an expansive gel that weakens the bond between the aggregate and the cement paste, which may lead to excessive cracking throughout the structure, as displayed in Figure 2.30. The following 3 factors govern the severity and extent of ASR's (Alexander and Mindess, 2005):

- *Reactive silicas* – The severity of ASR's is governed by the type and amount of chemically unstable silica in the aggregate. Well-known examples of reactive silica are altered or amorphous silica. Furthermore, reactive silica may also be encountered as poorly crystallised minerals, such as the microcrystalline, cryptocrystalline and strained quartz that may be present in tillites.

- *Alkalis* – The pore solution alkalis that are required for ASR's are mostly supplied by the cement/binder, although they may also be supplied by chemical admixtures, brackish water or even certain aggregates. The alkali content of cement is usually expressed in terms of the equivalent mass percentage of sodium oxide in the cement, expressed as Na_2O_{eq}. The risk of deleterious expansion is significantly higher for high-alkali cements, especially where Na_2O_{eq} exceeds 0.6 %. However, the actual amount of cement that is added to the concrete mix is more important than its alkalinity.

- *Environmental conditions* – Detrimental ASR cannot occur in an environment that is deficient in moisture. The external impact of moisture will be the more damaging in cases of high moisture and where the concrete element possesses a larger exposed surface area relative to its volume, e.g. long, thin elements. In cases where the exposed surface is relatively small, the moisture of the inner portion of concrete is usually retained enough to trigger ASR's, even where external moisture conditions are low. Local ASR's can also be caused by external sources of moisture and poor drainage.

An extensive petrographic analysis on Matjiesfontein tillite indicated that it does not carry a significant risk of ASR's for use as concrete aggregate (Van Wyk, 2013). Additionally, an accelerated mortar-bar test indicated slight expansion that may be regarded as innocuous (Janse van Rensburg, 2017). Considering that Matjiesfontein has a semi-desert climate (moisture deficient) which is generally accompanied by a reduced risk of ASR's (Alexander and Mindess, 2005), the results are deemed conclusive.

Figure 2.30: Du Vallon-Charest highway in Quebec, Canada, that was demolished due to ASR's (Fernandes and Broekmans, 2013).

2.5.2 Rock Engineering

Compressive Strength

Compressive strength of rock refers to the maximum compressive stress at failure. It can be measured either indirectly, through point load tests, or directly, through uniaxial unconfined compression (UCS) tests or triaxial tests. The advantage of point load tests is that they can be performed quickly on unprepared core samples, whereas UCS and triaxial tests require carefully prepared samples and laboratory apparatus. Since more accurate results are obtained through direct methods, they are generally preferred when the results are to be used in foundation design (Wyllie, 1999).

UCS tests involve the compression of cylindrical core samples between two parallel plates in the absence of a confining pressure. During triaxial tests, samples are subjected to a homogeneous pressure state where the two minor lateral stresses are equal (Jaeger, Cook and Zimmerman, 2007), i.e. $\sigma_1 > \sigma_2 = \sigma_3 > 0$.

Lateral stresses act as confining pressure and increase bearing capacity significantly. In situ rock is usually confined. Therefore, behaviour is presented more accurately by triaxial tests (Jaeger, 1979). On the other hand, the absence of confining pressure could result in more conservative strength estimates that would improve the safety of the design. At least 5 specimens should be tested with UCS tests. Cores with diameters of no less than 54 mm (NX size) and lengths of 2.5 - 3.0 times the diameter are prescribed (Bieniawski and Bernede, 1979). Lengths of 2.0 - 2.5 times the diameter, as prescribed in ASTM D 4543 (2001), are also widely accepted.

Loading must be applied at a rate of 0.5 - 1.0 $MPa/$s (Bieniawski and Bernede, 1979). Samples that are loaded more gradually tend to exhibit higher values of compressive strength. Results of UCS tests on the same rock type can vary remarkably, especially for heterogeneous rocks (Bewick et al., 2015). Large variations are mainly attributed to different failure modes. For example, specimens of the same rock can fail through axial splitting, splitting rupture, shearing of inherent discontinuities or a combination of modes.

Shear Strength

Failures during uniaxial or triaxial compression tests usually occur through shearing (Jaeger, 1979) when the shear strength limit along a certain plane is exceeded by the applied shear stress. Shear strength is expressed in terms of the normal stress, cohesion and friction angle and is assumed to behave according to Coulomb's law, as shown in Equation 2.2 (Wyllie, 1999):

$$\tau = c + \sigma' tan(\phi) \tag{2.2}$$

Where:
τ = Shear strength (kPa)
c = Cohesion (kPa)
σ' = Effective normal stress on shear plane (kPa)
ϕ = Friction angle (deg)

The cohesion and friction angle, also known as the Mohr-Coulomb parameters, refer to the shear strength provided by cementation between particles and the shear strength provided by the angle between the normal and resultant forces at failure, respectively (Allaby, 2008). In cases where the rock mass is fractured, shear strength may be governed by the Mohr-Coulomb parameters and the surface roughness of discontinuities. The risk of shear failure is usually low for intact rock or strong fractured rock masses that do not possess persistent discontinuity planes parallel to the shear plane (Wyllie, 1999).

Tensile Strength

Tensile failure typically occurs through punching or flexural failure in the presence of a weak subsurface layer (Wyllie, 1999). Since the tensile strength of fractured rock is negligible, it is usually ignored during design. However, structures occasionally require some tensile strength to resist uplifting forces or overturning moments, e.g. forces induced by wind loads on tall, slender structures. In these cases, tensile strength can be supplemented through the installation of anchor bolts.

Tensile strength can be estimated either directly through application of a pure pulling force at the ends of a core sample or indirectly through application of a flexural force. However, due to restrictions in the construction of representative fractured rock mass models, it is difficult to obtain accurate strength estimates from these tests. Alternatively, the tensile strength of a rock mass can be found using the Hoek-Brown failure criterion, as shown in Equation 2.3 (Hoek and Brown, 1988):

$$\sigma_t = 0.5\sigma_c[m - \sqrt{(m^2 + 4s)}] \tag{2.3}$$

Where:
σ_t = Uniaxial tensile strength (kPa)
σ_c = Uniaxial compressive strength (kPa)
m, s = Undisturbed Hoek-Brown material constants

Elasticity and Deformation

Rock stiffness is described by the modulus of elasticity (E) and the shear modulus (G), which are the ratios of longitudinal stress to longitudinal strain and lateral stress to lateral strain,

respectively (Allaby, 2008). Furthermore, the ratio of lateral strain to longitudinal strain is given by Poisson's ratio (v). Similar to compressive strength, the E-modulus may vary significantly depending on the rate of loading (Jaeger, 1979). For example, sandstone that is loaded slowly may exhibit an E-modulus up to 30 % higher than sandstone that is loaded rapidly. Therefore, the rate of loading should ideally be stated with the results.

Reported values of compressive strength, shear strength and elasticity for Dwyka tillite from the Goedertrouw and Oppermansdrift dams (George, Orr and Associates, n.d. cited in Brink, 1983), a tunnel 100 km east of Ulundi (Hawkins, Hawkins and Osborn, n.d. cited in Brink 1983), Lake Mentz in the Eastern Cape (Geertsema, 2000) and Natal (Paige-Green, 1975 cited in Brink 1983) are summarized in Table 2.7.

Table 2.7: Engineering properties of Dwyka tillite (after Brink, 1983 and Geertsema, 2000).

Value	W1				W2	W3				W4
	Goeder-trouw Dam	Ulundi Tunnel	Natal	Lake Mentz	Goeder-trouw Dam	Goeder-trouw Dam	Opper-mans-drift	Ulundi Tunnel	Natal	Goeder-trouw Dam
Unconfined Compressive Strength (MPa)										
Minimum	122	142	56	293	80	10	-	22	59	5
Maximum	298	194	222	340	130	40	-	62	82	22
Average	225	180	146	317	107	28	58	47	74	-
Sample size	-	4	7	3	-	-	2	4	10	-
Modulus of Elasticity (GPa)										
Minimum	-	39	-	81,13	-	-	-	13,3	-	-
Maximum	-	70	-	82,5	-	-	-	15,4	-	-
Average	-	54	55,16	81,7	-	-	26,4	14,8	25,53	-
Sample size	-	4	1	3	-	-	2	4	1	-
Poisson's ratio										
Minimum	-	0,22	-	0,251	-	-	-	0,29	-	-
Maximum	-	0,33	-	0,288	-	-	-	0,31	-	-
Average	-	0,27	0,28	0,267	-	-	0,16	0,3	0,3	-
Sample size	-	4	1	3	-	-	2	4	1	-
Friction angle (deg.)										
Average	-	-	53	51,3	-	-	-	-	51	-
Sample size	-	-	1	15	-	-	-	-	1	-
Cohesion (MPa)										
Average	-	-	30	57,6	-	-	-	-	8	-
Sample size	-	-	1	15	-	-	-	-	1	-
Density (kg/m³)										
Minimum	-	-	-	2665	2508	-	-	-	-	-
Maximum	-	-	-	2708	2690	-	-	-	-	-
Average	-	-	-	2692	2647	-	-	-	-	-
Sample size	-	-	-	15	-	-	-	-	-	-

Rock Quality Designation (RQD)

The Rock Quality Designation (RQD) is a measure of rock quality based on the percentage of core recovered through drilling (Bieniawski, 1989). It is calculated by measuring the total length of core pieces longer than 100 mm and dividing it by the total length of core run. Since the spacing and condition of discontinuities are not accounted for in the RQD, it does not provide enough information about the quality of a rock mass by itself. However, it is adequate for the identification of unfavourable conditions that may require further investigation (Bieniawski, 1989) and can be used effectively in conjunction with more comprehensive classification systems, such as the Rock Mass Rating.

Rock Mass Rating (RMR)

The Rock Mass Rating (RMR), also referred to as the Geomechanics Classification (Bieniawski, 1989), is based on the RQD, UCS, groundwater conditions and the spacing, condition and orientation of discontinuities. Each parameter is subdivided further into 5 ranges, which have been assigned ratings according to their significance in the overall classification of a rock mass.

After the ratings have been determined, the RMR is calculated as the sum of the ratings with adjustments for unfavourable scenarios. The RMR indicates whether a rock mass is suitable for specific applications, e.g. slopes, tunnels, mines and foundations. Furthermore, it is used in the design of reinforcements, e.g. the type and spacing of rock bolts in tunnels.

The RMR system is still widely used in practice today. Even so, many arguments have been raised regarding its efficacy in modern engineering (Chen and Yin, 2018). While some argue that there is room for improvement, others maintain that it is a time-tested method that has been implemented successfully for decades. The two most widely used variations are the systems introduced in 1989 (RMR89) and 2013 (RMR13).

RMR89 incorporates a combination of the RQD and the joint spacing, whereas it is replaced by Fracture Frequency in RMR13. The reason why the joint spacing and RQD was substituted in RMR13, is that several authorities on the subject suggested that the RQD is a large source of error and that it is no longer essential. Arguments against the RQD include the following (Chen and Yin, 2018):

- Only core pieces longer than 100 mm are considered, which may lead to erroneous measurements of fracturing in a rock mass
- The RQD value is orientation dependent
- The RQD is influenced by personal bias

Nevertheless, RMR89 has been used successfully by geologists and engineers for decades. As a result of the controversy surrounding the subject, a study was conducted that included artificial data sets from theoretical models as well as 187 actual cases worldwide (Chen and Yin, 2018). The study concluded that RMR89 is more accurate, can differentiate better between rock masses with variable characteristics and that it should continue to be used with confidence (Chen and Yin, 2018).

2.6 Foundation Design

2.6.1 Geotechnical Design

Many of the parameters that are required for foundation design possess some degree inherent variability. Numerous methods have been developed to account for the uncertainties, e.g. working load design (WLD), limit states design (LSD), sensitivity analysis and reliability analysis. Single parameter values are selected in WLD and LSD, while the effect of different values on overall stability is considered in sensitivity and reliability analyses (Wyllie, 1999). A combination of methods is usually implemented, since it can be difficult to determine the relationships between parameters.

Out of the methods mentioned here, WLD is the most widely used (Wyllie, 1999). WLD makes provision for safety by incorporating a global Factor of Safety (FoS), which is calculated as the ratio between the design capacity, e.g. the ultimate bearing capacity, and the utilized capacity, e.g. the applied bearing pressure. Although WLD results in safe designs, it is generally less accurate than LSD, since LSD makes provision for safety by incorporating individual partial factors for materials and loads at sources of uncertainty. The trade-offs between safety and accuracy are important to consider for the most efficient use of project resources.

With LSD, limit states can be verified at either the Ultimate Limit State (ULS) or Serviceability Limit State (SLS). ULS refers to the condition that a structure must remain stable against all expected loads throughout its service life (Wyllie, 1999). For example, to prevent bearing, sliding or overturning failure, the resistance of a foundation must be greater than the effect of actions. One or more of the following ultimate limit states must be identified as relevant (SANS 10160-1, 2011):

- STR/STR-P - Failure or excessive deformation of structural members
- EQU - Loss of equilibrium
- GEO - Failure or excessive deformation of the ground
- ACC - Relating to accidental and seismic actions
- FAT - Fatigue failure due to deterioration over time

SLS refers to the condition that a structure must remain safe from excessive damage or settlement that could impair functionality throughout its service life (Wyllie, 1999). Therefore, while ULS design is aimed toward the prevention of catastrophic failure, SLS is aimed toward appearance and functionality (Bond and Harris, 2008).

2.6.2 Failure Modes

Ultimate Limit State (ULS)

Bearing, sliding and overturning failure, as illustrated in Figures 2.21, 2.23, 2.24, respectively, are verified at the ultimate limit state. Spread foundations on rock are normally designed based on the estimated allowable bearing pressure of the founding material (EN 1997-1, 2004). Bearing failure occurs when the design value of bearing resistance, R_d, is exceeded by the design value of vertical load, V_d, transferred by the foundation and superstructure (EN 1997-1, 2004).

A downward vertical load results in displacement, which causes a triangular wedge to become trapped beneath the base. The passive zones beside the wedge are forced away from the base along the path of least resistance, which ultimately leads to the exposed surface in the case of a general bearing failure. On the other hand, when dealing with certain hard rock types, the estimated allowable bearing pressure is often governed by the compressive strength of the concrete in the foundation rather than the rock itself (EN 1997-1, 2004).

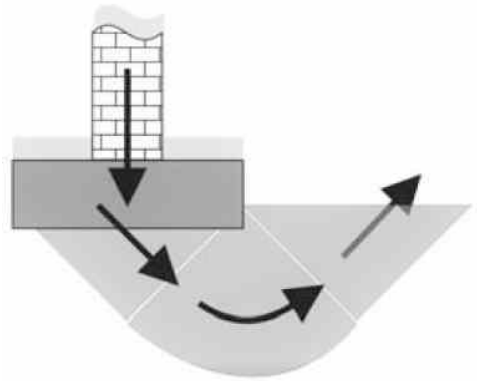

Figure 2.31: Bearing failure (Bond and Harris, 2008).

The characteristic vertical, V_k, and horizontal , H_k, loads are calculated as equivalent loads acting on the bottom of the foundation. The resulting load often acts eccentrically, causing an overturning moment. The eccentricity, e, is calculated by dividing the design moment, M_d, by the design vertical load. Here, only a certain portion of the total foundation area is fully utilized to resist failure. The new reduced area is referred to as the effective area, A'. For circular foundations, A' is elliptical, as displayed in Figure 2.22. The centre of the ellipsoid coincides with the load centre, LC. After A' is calculated along with the length, L_e, and width , B_e, of the ellipsoid, the dimensions of the equivalent rectangular load area, L' and B', can be calculated.

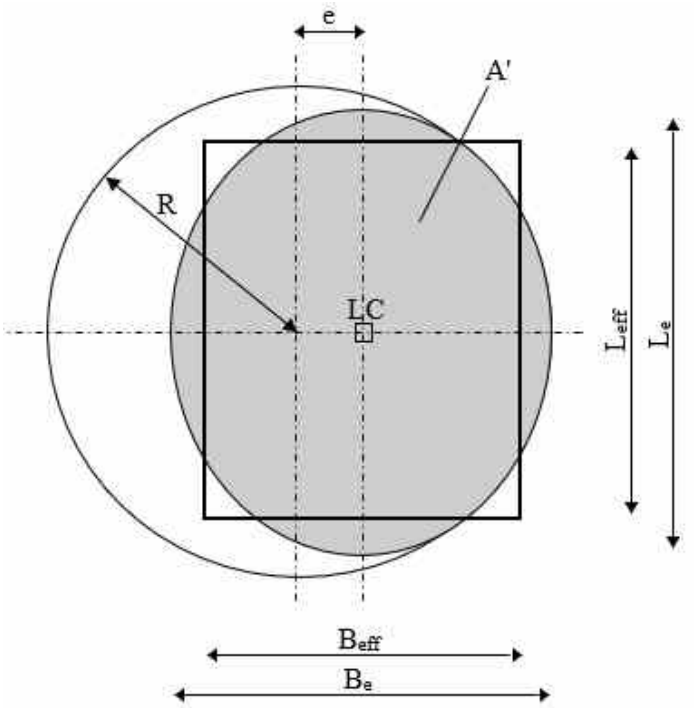

Figure 2.32: Effective area of a circular foundation (DNV/Risϕ, 2002).

It is important to assess whether the eccentricity is within acceptable limits; for circular foundations, $e \leq 0.6R$ (EN 1997-1, 2004). If the eccentricity limit is exceeded, special care must be taken with design values and tolerances. Alternatively, tolerances of up to 100 mm may be considered. One effective way of doing this is to assume that the foundation is 100 mm out of position relative to the column in the most unfavourable direction and re-calculate the size of the base (Day, pers. comm., 2018). Another adjustment is required if a torsional moment, $M_{z,d}$, is imposed on the foundation to account for the interaction between $M_{z,d}$ and the horizontal load, H_d. This can be done by replacing $M_{z,d}$ and H_d with an equivalent horizontal load, H' (DNV/Risϕ, 2002). Furthermore, the effect of water must be accounted for if the depth of the water table below the foundation is less than or equal to diameter of the base.

Sliding failure occurs when the design value of shearing resistance, R_d, is exceeded by the design value of horizontal load, H_d, that is transferred by the foundation and superstructure. It is important to remember that H_d must be replaced by H' if a torsional moment is involved. The design resistance is calculated as the product of V_d and the tangent of the design friction angle of the founding material. In cases where the foundation is pre-cast instead of cast in-situ, the friction angle must be reduced to 0.75 of its original value to account for poorer interlocking between the base and the founding surface (EN 1997-1, 2004). Cohesion is neglected in the analysis.

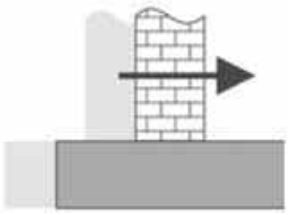

Figure 2.33: Sliding failure (Bond and Harris, 2008).

Overturning failure occurs when the design value of the total stabilizing moment, M_{stb}, is exceeded by the design value of the total destabilizing moment, M_{dst}, resulting in loss of equilibrium (EN 1997-1, 2004). In most cases, overturning is limited by bearing resistance, i.e. governed by the GEO limit state, instead of the EQU limit state as one would expect. However, overturning of foundations on rock may be governed by the EQU limit state provided that bearing resistance is no longer the governing factor (Bond and Harris, 2008).

Figure 2.34: Overturning faliure (Bond and Harris, 2008).

Serviceability Limit State (SLS)

Serviceability is verified if the design value of the effect of actions, E_d, is less than the limiting design value of the relevant criterion, S_d. Examples include retaining wall deflection, excessive flow in dams, vibrations from driven piles and settlement, the last of which is crucial in the design of spread foundations. Limitations on parameters vary depending on the type of structure. According to EN 1997-1 (2004), settlement may be calculated using an equation of the following form:

$$s = \frac{fpB}{E} \tag{2.4}$$

Where:

s = Total settlement

f = Settlement coefficient

p = Uniformly distributed bearing pressure

B = Width or diameter of foundation

E = Design value of modulus of elasticity

Chapter 3

Methods

3.1 Coarse Concrete Aggregates

The suitability of slightly weathered (W2) and highly weathered (W4) tillite for use as coarse concrete aggregate was evaluated. The following tests were included, as prescribed by SANS 1083 - Aggregates from Natural Sources, Aggregates for Concrete (2017):

- Grading
- Flakiness Index (FI)
- Aggregate Crushing Value (ACV)
- 10% Fines Aggregate Crushing Value (10% FACT)

In addition, a slake durability test was performed to assess the effect of weathering on the resistance of tillite to degradation, since aggregate durability influences both the workability of fresh concrete and the durability of hardened concrete. Tests for ASR's were excluded since, as mentioned in Section 2.5.1, petrographic analyses and accelerated mortar bar tests indicated that tillite does not carry a significant risk of ASR's.

3.1.1 Sample Collection and Crushing

W2 and W4 tillite samples were collected from two seperate outcrops south of the site area, as displayed in Figure 3.1. Outcrops were identified according to the grades of weathering described by Brink (1983), as discussed in Section 2.4.3. Due to difficulty of excavation, the collection of W2 tillite was mostly limited to loose-lying cobbles. On the other hand, in situ W4 tillite could be ripped off using a pick-axe. After the samples were broken into suitable feed sizes, they were crushed using a small jaw crusher. Although the crusher could not be set to produce a specific nominal stone size, the bottom jaw opening was adjusted to control the maximum size.

Three phases of crushing were implemented to minimize the size reduction ratio. For the first phase, samples were crushed to a maximum size of 50 mm. For the second and third

phases, the maximum size was reduced to 20 mm. The crusher was choke-fed throughout to facilitate secondary breakdown through interparticle friction and collision.

Figure 3.1: Source locations of slightly weathered (W2) and highly weathered (W4) tillite outcrops.

3.1.2 Grading

The grading of coarse (>5 mm) W2 and W4 tillite was determined according to SANS 3001-AG1 (2014) subsequent to the third phase of crushing. Samples of approximately 3 kg were quartered out according to method MD2 of TMH5 (1981). Samples were oven dried to a constant mass, a. Thereafter, they were soaked and washed through a 0.075 mm sieve for the calculation of dust contents, for which a maximum of 2 % is specified.

Samples were dried to a constant mass once more after the wet sieving process and the mass, b, was recorded. Thereafter, they were sieved on a mechanical shaker through a standard set of nested sieves, as displayed in Figure 3.2. The mass retained on each sieve was recorded along with the mass of dust retained in the pan, c. The dust contents and uniformity coefficients were calculated using Equations 3.1 and 3.2, respectively (SANS 3001-AG1, 2014):

$$D = \frac{(a-b)+c}{M_{F_f}} \tag{3.1}$$

Where:
D = Dust content (%)
a = Dried sample mass prior to wet sieving (g)
b = Dried sample mass subsequent to wet sieving (g)
c = Mass of dust retained in pan (g)

M_{F_f} = Total mass of sample including, a - b (g)

$$U_a = \frac{D_{60}}{D_{30}} \tag{3.2}$$

Where:

U_a = Uniformity coefficient

D_{60} = Hypothetical sieve aperture size through which 60 % of material passes (mm)

D_{30} = Hypothetical sieve aperture size through which 30 % of material passes (mm)

Figure 3.2: Stacked sieves for dry sieving of coarse particles on a mechanical shaker.

3.1.3 Flakiness Index (FI)

Flakiness Indices were determined for W1 and W2 tillite according to SANS 3001-AG4 (2015), wherein a maximum of 35 % is specified. FI's were determined for both samples after the third phase of crushing. Additionally, it was determined after phases 1 and 2 for W2 tillite only, so that the effect of repeated crushing on particle shape may be observed; based on the results, recommendations could be made with regard to on-site crushing of the rock.

Representative samples were quartered out using method MD2 of TMH5 (1981). Samples were sieved through a standard set of sieves on a mechanical shaker until the appropriate size fractions were obtained, as displayed in column 5 of Table 3.1. After the mass of each size fraction was recorded, they were gauged according to their respective slot sizes using a standard flakiness plate, as displayed in Figure 3.3.

Table 3.1: Prescribed Flakiness Index sample sizes for different fractions (after SANS 3001-AG4, 2015).

1	2	3	4	5
Fraction size to be gauged		Slot dimensions		App. mass of sample to pass sieves in column 1 (g)
Passing (mm)	Retained (mm)	Min. length (mm)	Width (mm)	
75,0	50,0	150,0	37,5	4000
50,0	37,5	100,0	25,0	4000
37,5	28,0	75,0	18,7	4000
28,0	20,0	50,0	14,0	3000
20,0	14,0	40,0	10,0	2000
14,0	10,0	27,0	7,0	1250
10,0	7,1	20,0	5,0	750
7,1	5,0	15,0	3,5	500

The initial and passing weights of each fraction was measured. Finally, flakiness indices were determined for each size fraction and for each sample as a whole using Equation 3.3:

$$FI = 100\frac{M_F}{M_S} \tag{3.3}$$

Where:
FI = Flakiness Index
M_F = Mass passing the slots (g)
M_S = Mass of fraction or sample (g)

Figure 3.3: Plate with standard slot dimensions for determination of the Flakiness Index (FI).

3.1.4 ACV and 10%FACT Tests

Aggregate Crushing Value (ACV) and 10% Fines Aggregate Crushing Value (10%FACT) tests were performed according to SANS 3001-AG10 (2012), wherein a maximum of 29 % and minimum of 110 kN is specified for ACV and 10%FACT, respectively. ACV refers to the percentage of fines (in this case <2 mm) generated through the application of a 400 kN vertical load, while the 10%FACT value represents the load required to generate 10 % fines. The tests allow for the elimination of aggregates that have a low resistance to crushing and may generate excessive fines during handling and mixing. A full set of dry and soaked tests were completed, since it also allows for the calculation of water absorption and wet/dry 10%FACT ratios.

Although SANS 3001-AG10 is specified as the standard method for the ACV and 10%FACT tests in SANS 1083, the standard size fractions differ slightly. While a fraction of 10 - 14 mm is used in SANS 3001-AG10, 9.5 - 13.2 mm is used in SANS 1083. However, the outcome should not be affected, since the sizes are interchangeable according to SANS 3001-AG10. Roughly 9 kg of 10 - 14 mm stone is required for a single set of tests. Since 2 full sets of wet and dry tests were to be completed, 18 kg was sieved out for each sample. During sample preparation, stones were compacted in 3 layers inside a measuring container with 25 light strokes of a tamping rod; the apparatus is displayed in Figure 3.4.

Figure 3.4: ACV apparatus - 2 mm sieve and pan (a), measuring container (b), plunger (c), crushing cylinder (d) and tamping rod (e).

After the sample masses were recorded, they were compacted into a crushing cylinder. The cylinder was covered with a plunger and placed on a Contest compression testing machine, as displayed in Figure 3.5, and crushed at a constant rate of 40 kN/min until the maximum prescribed load of 400 kN was reached.

Figure 3.5: ACV sample prior to crushing mounted on a Contest compression machine

Subsequently, the crushed material was sieved on a 2 mm aperture sieve and the passing fraction was weighed. The ACV was calculated using Equation 3.4 (SANS 3001-AG10, 2012):

$$ACV = 100\frac{M_{1p}}{M_1} \tag{3.4}$$

Where:
ACV = Aggregate Crushing Value (%)
M_{1p} = Mass of passing fraction (g)
M_1 = Mass of sample (g)

The first estimate of the load required to produce 10 % fines was calculated using Equation 3.5 and subsequently used in Equation 3.6 to calculate the second estimate (SANS 3001 - AG10, 2012):

$$F_1 = \frac{4000}{(ACV)} \tag{3.5}$$

Where:
F_1 = First 10%FACT load estimate (kN)

$$F_2 = F_1\frac{1-(P_1-10)}{P_1} \tag{3.6}$$

Where:
F_2 = Second 10%FACT load estimate (kN)
P_1 = Actual percentage of fines generated by F_1

The acceptance indicator, ϵ, was calculated using Equation 3.7:

$$\epsilon = \frac{20}{3(ACV)^{0.6}} \tag{3.7}$$

If the acceptance condition, $\epsilon \geq |P_2 - 10|$, was not met, the test would have had to be repeated (SANS 3001 - AG10, 2012). Depending on the result of the acceptance condition, the 10%FACT value was calculated using either Equation 3.8 or Equation 3.9 (SANS 3001 - AG10, 2012):

$$for \epsilon > |P_1 - 10|, \quad (10\%FACT) = \frac{F_1 + F_2}{2} \tag{3.8}$$

$$for \epsilon < |P_1 - 10|, \quad (10\%FACT) = F_2 \tag{3.9}$$

The process was repeated for soaked samples. Thereafter, the wet to dry 10%FACT ratios were calculated using Equation 3.10 (SANS 3001 - AG10, 2012):

$$(10\%FACT_{w/d}) = 100\frac{(10\%FACT_w)}{(10\%FACT_d)} \tag{3.10}$$

Where:
$10\%FACT_{w/d}$ = Wet/dry ratio (%)
$10\%FACT_w$ = Wet 10%FACT load (kN)
$10\%FACT_d$ = Wet 10%FACT load (kN)

Finally, the water absorption was calculated using Equation 3.11 (SANS 3001 - AG10, 2012):

$$W_{Abs} = 100\frac{M_{s_{avg}} - M_{d_{avg}}}{M_{d_{avg}}} \tag{3.11}$$

Where:
W_{Abs} = Water absorption (%)
$M_{s_{avg}}$ = Average mass of surface dry soaked samples (g)
$M_{d_{avg}}$ = Average mass of dry samples (g)

3.1.5 Slake Durability Test

A slake durability test was performed to evaluate and compare the durability of W2 and W4 tillite. Additionally, the test may be used to eliminate instances of degrading tillite - by subjecting the samples to repeated dry/soaked cycles, the affect of the shrinkage/expansion within the matrices on the integrity of individual rock lumps could be observed directly. Although ASTM D4644-16 (2016) is the standard test method for slake durability, an alternative method suggested by Brink (1983) and adjusted by Van Wyk (2013) was selected. According to Brink (1983), the standard method is ideal for the quantitative evaluation

of breakdown into a certain size fraction (<2 mm), while the alternative method is more applicable for the qualitative evaluation of breakdown into various shapes and sizes. Two samples were prepared for each grade of weathering. Each sample consisted of 7 rock lumps that passed the 36.5 mm sieve and were retained on the 26.5 mm sieve. The samples were weighed and placed in separate PVC bins, which are fitted with 20 mm diameter holes and closed off on the sides with 13 mm wire mesh. Plastic containers were placed underneath the bins for the collection of broken particles, as displayed in Figure 3.6.

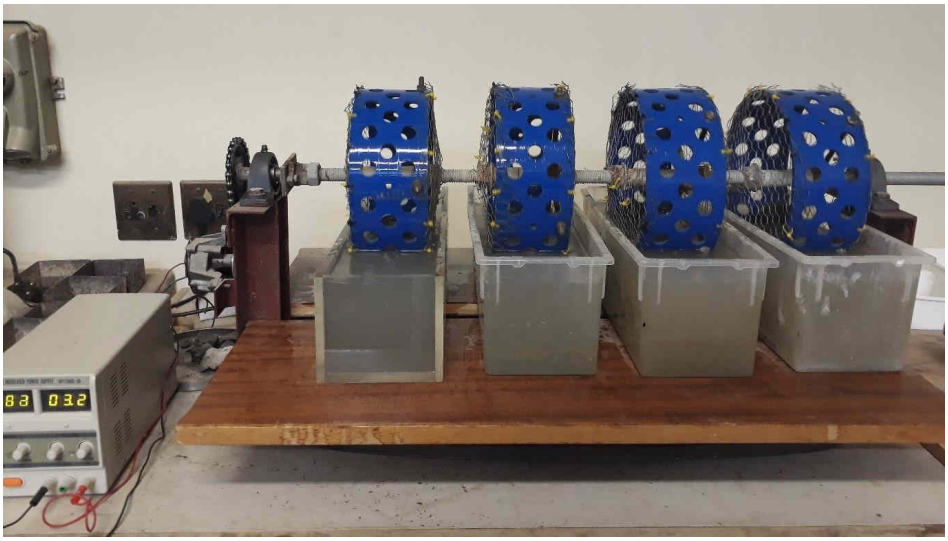

Figure 3.6: Slake durability test in progress.

The samples were rotated for a total of 5 wet/dry cycles at a constant rate of 5 rev/min. The duration of a single cycle was 24 hours, which was comprised of a 12 hour dry cycle followed by a 12 hour wet cycle. For each wet cycle, the plastic containers were elevated so that all rock lumps were submerged entirely. At completion of the final wet cycle, the remaining rock lumps inside the PVC bins were removed, dried and weighed. Remaining fractions of W2 and W4 tillite were calculated using Equation 3.12:

$$F_r = 100\frac{M_{f_{avg}}}{M_{i_{avg}}} \tag{3.12}$$

Where:
F_r = Remaining fraction (%)
$M_{f_{avg}}$ = Average final dry mass of rock lumps (g)
$M_{i_{avg}}$ = Average initial dry mass of rock lumps (g)

3.2 Rock Mass Characterization

In Chapter 2, various reports on the properties of Dwyka tillite were reviewed. Although past studies provide good insight of what can be expected, every site is unique in the conditions it provides. Rock mass characterization methods were implemented to further define local founding conditions. The following methods were included:

- Electro-resistivity
- Drilling and core logging
- Rock Quality Designation (RQD)
- Unconfined Compressive Strength (UCS) tests
- Rock Mass Rating (RMR)

3.2.1 Electro-Resistivity

Electro-resistivity is a non-invasive geophysical tool that employs the direct application of electrical current into the ground through shallow driven electrodes. Measurements can indicate features such as aquifers, cavities, fractured zones, faults and zones of varying permeability. The primary instrumentation consists of a control unit, active multi-electrode cables (multicables) and stainless steel electrodes, as displayed in Figure 3.7.

Figure 3.7: Primary electro-resistivity instrumentation, namely an ARES control unit, multi-electrode cable and stainless steel electrodes (Gf Instruments, n.d.).

Firstly, three parallel 160 m test lines were measured along the length of the site in preparation for an extended measurement. Test measurements were performed from east to west with a parallel spacing of 50 m, starting on the airstrip. Each multicable electrode was placed at a predetermined location. Although the maximum spacing between electrodes is 6 m, a

spacing of 5 m was selected to ensure consistent spacing over vegetation and slight elevations or depressions in the profile.

Electrodes were wetted prior to measurements for improved conductivity. Holes were drilled for electrodes that could not be driven into solid outcrops of tillite. After all electrodes were anchored, as shown in Figure 3.8, the multicables were connected and activated for measurement using an ARES control unit and an external 12 V battery. Here, a dipole-dipole setting was used, as it allows for the most detailed arrays, especially for the detection of vertical structures (Gf Instruments, 2019); other relevant settings are attached in Appendix B.1. Results were deemed representative if similar structures were observed across all test lines.

Figure 3.8: Anchored multi-cable electrode.

For the extended measurement, 3 multicable sections (120 m in total) were measured simultaneously along the path of Test Line 2 Figure 3.9. After the first measurement, a repeating roll-along manoeuvre was used to extend the line for a total measured length of roughly 1 km, i.e. during one 120 m measurement, the unconnected cable is carried to the front of the line and prepared for the following 120 m measurement, for which the cable at the back of the line becomes the unconnected cable.

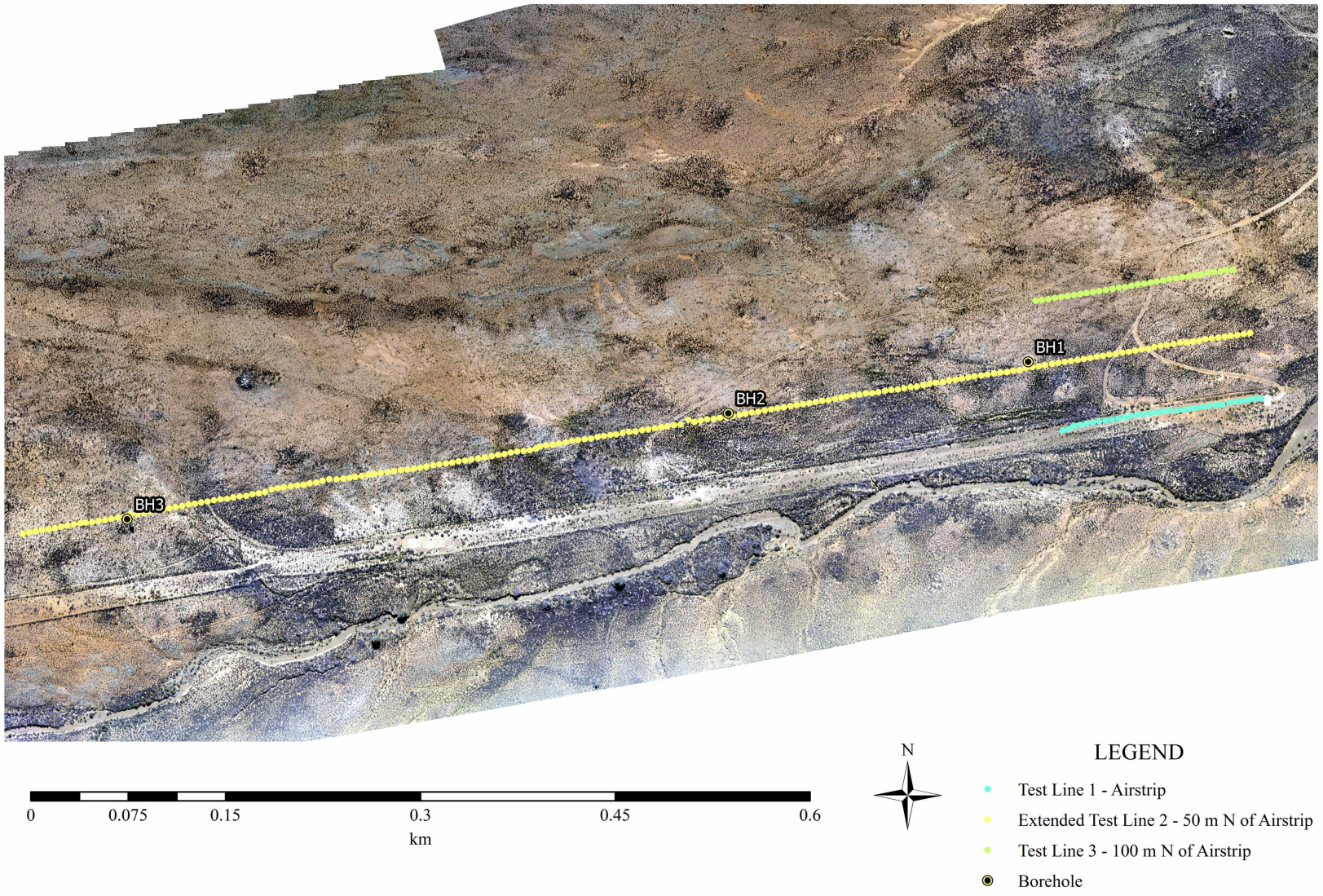

Figure 3.9: Electro-resistivity test lines and locations of subsequent boreholes.

3.2.2 Drilling and Core Logging

Three 100 mm diameter boreholes of 3 m deep were drilled to obtain samples for rock mass characterization and compressive strength tests. Based on resistivity images (see Figure 4.6 on p. 87), 3 locations were selected along Extended Test Line 2, as displayed in Figure 3.9. Since core could only to be drilled to a depth of 3 m, locations were selected where layers of variable resistivity appeared close to the surface. By doing so, core data could potentially be extrapolated to areas that exhibit similar resistivities. Surface outcrops were required for good recovery and for stabilising the core drill. Therefore, drilling was performed slightly north or south of extended Test Line 2; the coordinates are displayed in Table 3.2.

Table 3.2: Coordinates of boreholes along Extended Test Line 2.

Borehole	Latitude	Longitude	Elevation (masl)
BH1	33 ° 14' 21,1" S	20 ° 34' 15,5" E	917,6
BH2	33 ° 14' 22,4" S	20 ° 34' 6,6" E	922,4
BH3	33 ° 14' 25,0" S	20 ° 33' 48,7" E	929,6

A DD 350-CA core drill was used, as displayed in Figure 3.10. The machine only allowed for the recovery of short core pieces at a time. Pieces were occasionally left behind in the borehole, in which case soil was shovelled into the borehole to improve cohesion inside the drill bit and retrieve the pieces. In addition, a constant supply of water during operation lead to the formation of a clayey sludge in the boreholes. As a result, interpretations regarding the orientation, spacing and condition of discontinuities were compromised.

Figure 3.10: Drilling in progress.

Core logging was done according to the method recommended by the Core Logging Committee of South Africa (1976). Core pieces were removed, washed and re-positioned inside the core box prior to logging. Six descriptive parameters were used, namely colour, weathering, fabric and discontinuity spacing, hardness, geologic type and stratigraphic horizon.

3.2.3 Rock Quality Designation (RQD)

Rock Quality Designations (RQD's) were determined for each borehole by dividing the total length of core pieces longer than 100 *mm* by the total length of core run. Based on the RQD's, rock quality was classified as *excellent*, *good*, *fair*, *poor* or *very poor* in accordance with the intervals given in Table 3.3.

Table 3.3: Rock Quality Designation (RQD) class intervals (ASTM D 6032-96, 1997).

RQD (%)	Rock Quality
90 - 100	Excellent
75 - 90	Good
50 - 75	Fair
25 - 50	Poor
0 - 25	Very poor

3.2.4 Unconfined Compressive Strength (UCS) Tests

Compressive strength is a very important parameter in foundation design. Furthermore, it is required for the determination of the RMR. Unconfined Compressive Strength (UCS) tests were performed on 5 standard specimens. The sample population was limited by the amount and quality of core that was recovered. Fortunately, a population of 5 conforms to the minimum amount that is recommended for testing (Bieniawski and Bernede, 1979).

Specimens were cut to length using a table saw. Their surfaces were levelled using a precision grinding machine, as displayed in Figure 3.11. Where possible, specimens were cut to a length/diameter (L:D) ratio of 2.5 - 3.0 (Bieniawski and Bernede, 1979). Alternatively, specimens were deemed acceptable if they conformed to a L:D ratio of 2.0 - 2.5, as prescribed in ASTM D 4543 (2001).

Figure 3.11: UCS specimen preparation on a grinding machine.

Specimen details are summarized in Table 3.4. Since the crushing apparatus that was used specified load application rate in units of kN/min, a unique value was calculated for each specimen according to their cross sectional areas so that all specimens were loaded at a constant rate of 0.5 MPa/s (Bieniawski and Bernede, 1979).

Table 3.4: UCS specimen details and loading conditions.

Sample	Borehole	Depth (m)	Length (mm)	Diameter (mm)	L:D	Area (mm²)	Rate (MPa/s)	Rate (kN/min)
S1	BH1	2,8 - 3,1	195	100	2,0	7854,0	0,5	235,6
S2	BH1	2,4 - 2,7	257	95	2,7	7088,2	0,5	212,6
S3	BH3	1,0 - 1,5	230	91	2,5	6503,9	0,5	195,1
S4	BH2	1,5 - 1,8	225	93	2,4	6792,9	0,5	203,8
S5	BH2	1,8 - 2,1	225	92	2,4	6647,6	0,5	199,4

Due to variable strengths, it was decided that a greater number of specimens must be tested to obtain a more conclusive estimate of compressive strength. Cubes were cut from the remaining rock core for additional testing, as shown in Figure 3.12. Thirty cubes were prepared in total. As described for the cylinders, the load application rate was maintained at 0.5 MPa/s. The cubes were crushed on a calibrated Contest compression machine. Since the slenderness (L:D) ratio has a significant influence on UCS and the cubes had a ratio of 1.0 compared to the ideal 2.5, the resulting UCS values were adjusted accordingly. A graph created by Bewick et al. (2015), in which the relative strength of various materials is plotted against corresponding slenderness ratio's, indicated that UCS at a L:D ratio of 1.0 is equal to around 115 % of UCS at a L:D of 2.5. Therefore, all cube strengths were divided by a factor of 1.15. Finally, data sets were combined for overall estimates of compressive strength for grade W1, W2 and W3 tillite.

Figure 3.12: 50 *mm* cubes cut from remaining rock core for additional UCS tests.

3.2.5 Rock Mass Rating (RMR)

An average RMR was determined for tillite at the site area as an indication of overall rock mass quality. Quality was classified according to the intervals displayed in Table 3.5 and ratings were assigned according to the values displayed in Table 3.6. The appropriate compressive strength range was selected based on UCS results. A few assumptions were made, since the RMR was determined from core samples. Firstly, since the true lengths of discontinuities were unknown, a length >20 *m* was assumed and a rating of 0 was assigned. Secondly, groundwater conditions were assumed to be completely dry based on local climatic conditions. Thirdly, the orientation of discontinuities was classified as favourable based on the apparent dipping angle.

Table 3.5: RMR class intervals (after Bieniawski, 1989).

Classes		
I	Very good rock	81-100
II	Good rock	61-80
III	Fair rock	41-60
IV	Poor rock	21-40
V	Very poor rock	<20

Table 3.6: RMR parameter classes and ratings (after Bieniawski, 1989).

Parameter			Range						
1	Strength of intact rock material	Point-load strength index	> 10 MPa	4 - 10 MPa	2 - 4 MPa	1 - 2 MPa	UCS preferred for low range		
		Uniaxial Comp. Strength	> 250 MPa	100 - 250 MPa	50 - 100 Mpa	25 - 50 MPa	5 - 25 MPa	1 - 5 MPa	< 1 MPa
	Rating		15	12	7	4	2	1	0
2	Drill core quality RQD		90 % - 100 %	75 % - 90 %	50 % - 75 %	25 % - 50 %	< 25 %		
	Rating		20	17	13	8	3		
3	Spacing of Discontinuities		> 2 m	0.6 - 2 m	200 - 600 mm	60 - 200 mm	< 60 mm		
	Rating		20	15	10	8	5		
4	Length/Persistence		< 1 m	1 - 3 m	3 - 10 m	10 - 20 m	>20 m		
	Rating		30	25	20	10	0		
	Separation		None	< 0,1 mm	0,1 - 1,0 mm	1 - 5 mm	> 5 mm		
	Rating		6	5	4	1	0		
	Roughness		Very rough	Rough	Slightly rough	Smooth	Slickensided		
	Rating		6	5	3	1	0		
	Infilling/gouge		None	Hard < 5 mm	Hard > 5 mm	Soft < 5 mm	Soft > 5 mm		
	Rating		6	4	2	2	0		
	Weathering		Unweathered	Slightly weathered	Medium weathered	Highly weathered	Completely weathered		
	Rating		6	5	3	1	0		
5	Ground water	Inflow/10 m tunnel (l/m)	None	< 10	10 - 25	25 - 125	> 125		
		Joint water press./ Maj. prin. stress (σ)	0	< 0.1	0.1 - 0.2	0.2 - 0.5	> 0.5		
		General conditions	Completely dry	Damp	Wet	Dripping	Flowing		
	Rating		15	10	7	4	0		
6	Strike and dip orientation		Very favourable	Favourable	Fair	Unfavourable	Very unfavourable		
	Rating adjustment		0	-2	-7	-15	-25		

3.2.6 Atterberg Limits

During core logging and subsequent tests it was observed that medium weathered tillite is remarkably more clayey than fresh tillite. Therefore, two sets of Atterberg limit tests were performed on unweathered, slightly weathered and medium weathered tillite to quantify and compare moisture sensitivities. Tests were performed according to SANS 3001-GR10 (2013). Core specimens that would otherwise have gone unutilized were crushed in several stages as explained in Section 3.1.1, except that the jaw crusher was adjusted to produce fine aggregates. Aggregates were sieved on a mechanical shaker to obtain sufficient fractions of material passing the 425 μm and 75 μm sieves, as displayed in Figure 3.13.

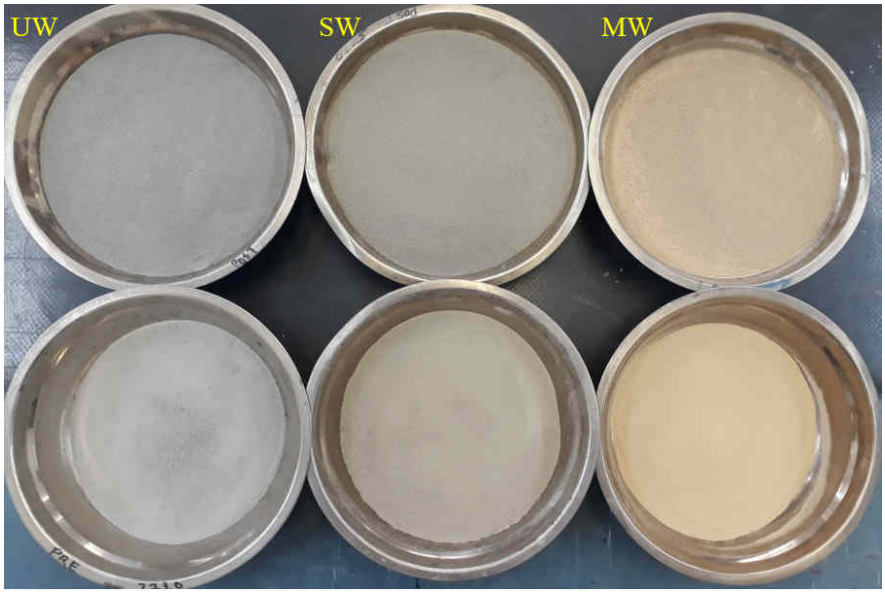

Figure 3.13: Crushed and sieved unweathered (UW), slightly weathered (SW) and medium weathered (MW) tillite passing the 425 μm (top) and 75 μm (bottom) sieves.

Size fractions were adjusted so that each sample contained 75 μm material equal to 20 % of the mass of its 425 μm material. At the start of each test, water was added to the mixture to form a thick paste. Thereafter, the material was placed inside a Casagrande liquid limit instrument, divided using a grooving tool and tapped at a rate of approximately 2 rev/s. The liquid limit (LL) was calculated at the moisture content where divided halves made roughly 10 mm of contact in the centre of the bowl after 22 - 28 taps. From the remaining material, a portion was pressed into a trough for the determination of the shrinkage limit (SL) and a portion was reserved for the determination of the plastic limit (PL). The PL involved the repeated rolling of material into threads with diameters of 3 mm. It was determined at the moisture content where small cracks started to form in the threads, thereby signalling non-plastic behaviour. Finally, the plasticity indices (PI's) were determined as the difference between the plastic and liquid limits.

3.3 Preliminary Foundation Design

Founding conditions on site are expected to meet the requirements comfortably, since the large telemetry dishes are to be emplaced on very competent rock. A preliminary foundation design was performed to evaluate whether that is the case, and if so, to which degree. As a preliminary design, it is merely intended to serve as an indication of the required foundation size and potential governing factors according to basic calculations. According to Avenant (pers. comm., 2019), the dishes that are planned for emplacement at the MSGO are very similar to DSS-36, a 34 m telemetry dish stationed at the Canberra Deep Space Communications Complex (CDSCC), as shown in Figure 3.14.

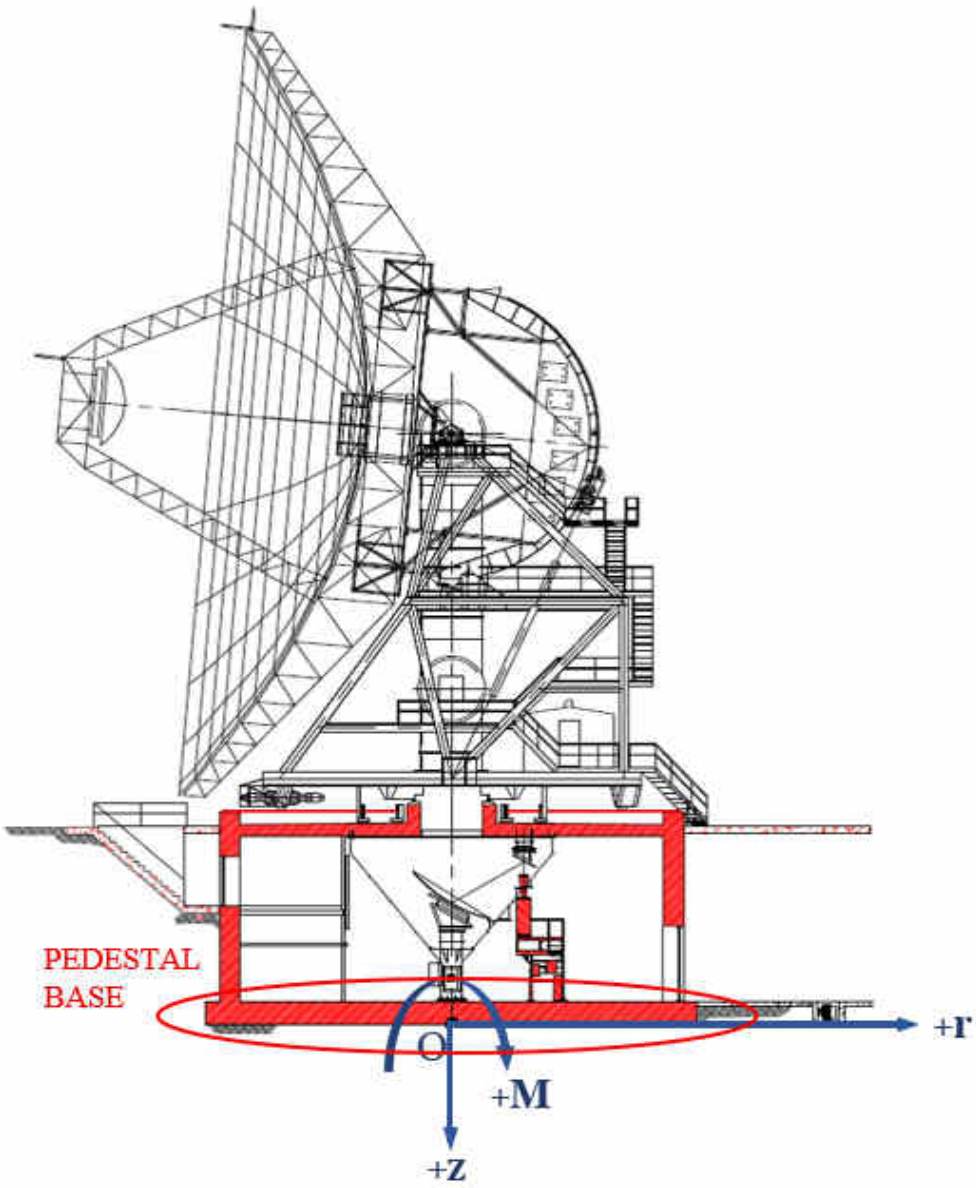

Figure 3.14: Schematic of DSS-36 (Warren, 2016).

The supporting pedestal is a 2-storey cylindrical structure that houses the transmitting and receiving equipment. In the case of DSS-36, the entire pedestal is underground. However, considering the shallow bedrock on site, it is likely that only the pedestal base will be embedded. Here, a founding depth and foundation thickness of 1.5 m was assumed. This section pertains to the design of the base (herinafter referred to only as the foundation).

A limit states design approach was used. Since loads and material properties were factored individually for their uncertainty, a minimum Factor of Safety (FoS) of 1 was deemed satisfactory for sliding and overturning failure. Bearing failure was evaluated using the generalised Hoek-Brown failure criterion; since no standard partial material factors are stated in SANS 10160-1 (2011) for the Hoek-Brown material constants, a minimum FoS of 3 was imposed on bearing failure. Based on recovered core samples, which is discussed further in Chapter 4, the quality of founding rock was assumed to be at least grade W2 tillite. Furthermore, it was assumed that thin layers of W3 tillite will be removed if encountered.

3.3.1 Material Properties

With the exception of compressive strength and the unit weights of the founding and overburden material, properties were obtained indirectly. The following properties were required:

- Unconfined Compressive Strength, UCS
- Modulus of elasticity, E
- Deformation modulus, E_{rm}
- Disturbance factor, D
- Intact rock material constant, m_i
- Geological Strength Index, GSI
- Rock mass material constants, m_b, s and a
- Poisson's ratio, v
- Maximum confining pressure, $\sigma_{3,max}$
- Friction angle, ϕ
- Cohesion, c
- Concrete compressive strength, f_c
- Unit weight of founding material, γ_{W2}

- Unit weight of concrete, γ_c
- Unit weight of overburden material, γ_o

The average UCS of W2 tillite was selected as 74.2 MPa based on test results. The E-modulus of W2 tillite, which was required for the calculation of settlement, was determined as 26.8 GPa from a linear correlation between known values of Dwyka tillite, as displayed in Figure 3.15.

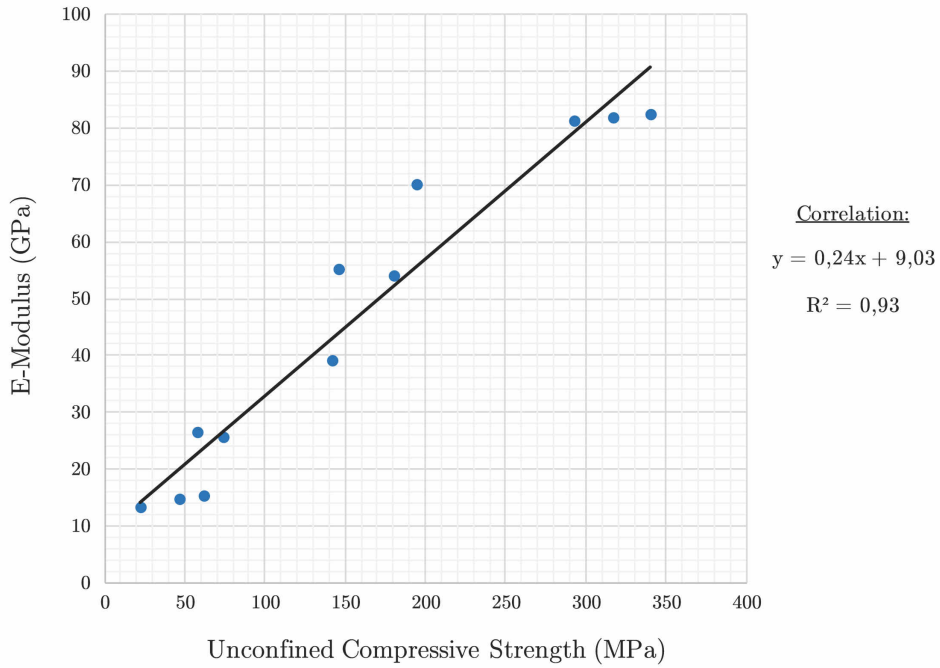

Figure 3.15: Correlation between UCS and E-Modulus for Dwyka tillite.

Since the intact E-modulus is not representative of a fractured rock mass, the equivalent deformation modulus, also referred to as the rock mass modulus, E_{rm}, was calculated using Equation 3.13 (Hoek and Diederichs, 2006):

$$E_{rm} = E(0.02 + \frac{1 - \frac{D}{2}}{1 + e^{((60+15D-GSI)/11)}}) \tag{3.13}$$

A disturbance factor, D, of 0.5 was selected for controlled small-scale blasting (Hoek and Brown, 2018). The Geological Strength Index, GSI, was determined from the average RMR, using Equation 3.14 (Hoek and Brown, 1997):

$$GSI = RMR - 5 \tag{3.14}$$

The intact rock material constant of tillite, m_i, which is a required input parameter for the calculation of the Hoek-Brown principle stresses, was selected as 10.0 based on a study by

Steenkamp (2014). The rock mass material constants, m_b, s and a, were calculated using Equations 3.15, 3.16 and 3.17, respectively (Hoek and Brown, 2018):

$$m_b = m_i e^{\frac{GSI-100}{28-14D}} \tag{3.15}$$

$$s = e^{\frac{GSI-100}{9-3D}} \tag{3.16}$$

$$a = \frac{1}{2} + \frac{1}{6}(e^{\frac{-GSI}{15}} - e^{\frac{-20}{3}}) \tag{3.17}$$

Poisson's ratio was determined as 0.294 from a linear correlation between known values, as displayed in Figure 3.16. Note that the outlier (red) was excluded from the correlation.

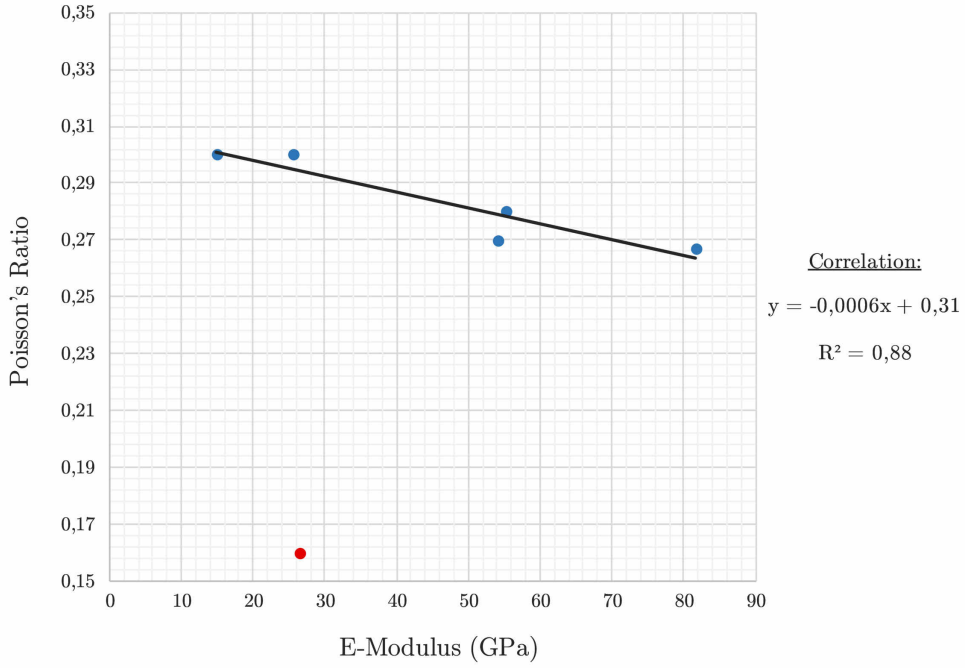

Figure 3.16: Correlation between E-Modulus and Poisson's ratio for Dwyka tillite.

The maximum confining pressure, $\sigma_{3,max}$, was calculated using the generalized Hoek-Brown failure criterion. Here, the minor principle stress was calculated as the major principle stress in the absence of a confining pressure, i.e. as if for a tri-axial specimen turned on its side at the surface of the founding rock, as shown in Equation 3.18:

$$\sigma_{3,max} = 0 + \sigma_{ci}(m_b(\frac{0}{\sigma_{ci}}) + s)^a \tag{3.18}$$

Where:

σ_{ci} = Unconfined Compressive Strength

The values of the Mohr-Coulomb shear strength parameters, c and ϕ, that are summarized in Table 2.7 apply to intact specimens. To obtain parameters that are representative of a rock mass, the Hoek-Brown equivalent values of c and ϕ were calculated using Equations 3.19 and 3.20, respectively (Hoek et. al, 2002):

$$c = \frac{\sigma_{ci}[(1+2a)s + (1-a)m_b\sigma_{3n}](s + m_b\sigma_{3n})^{a-1}}{(1+a)(2+a)\sqrt{1 + (6am_b(s + m_b\sigma_{3n})^{a-1})/((1+a)(2+a))}} \tag{3.19}$$

$$\phi = sin^{-1}[\frac{6am_b(s + m_b\sigma_{3n})^{a-1}}{2(1+a)(2+a) + 6am_b(s + m_b\sigma_{3n})^{a-1}}] \tag{3.20}$$

Where:

$\sigma_{3n} = \sigma_{3,max}/\sigma_{ci}$

As mentioned in Section 2.6.2, bearing pressure should not be allowed exceed the compressive strength of the concrete in the foundation. Concrete strength of 40 MPa was assumed, since it is unlikely that weaker concrete will be used in the foundation of such a large, sensitive structure. Furthermore, the unit weight of concrete was assumed as 24 kN/m^3.

Since local material will be removed prior to construction and subsequently recompacted in layers, the unit weight of overburden material was taken as 19.6 based on the results of modified AASHTO compaction tests that were performed on 3 test hole samples from the site area (Coetzee, 2017). The unit weight of W2 tillite was calculated as 25.3 kN/m^3 by submerging numerous core pieces with known mass in a graduated cylinder. Design values, X_d, were calculated for the STR, STR-P, GEO and EQU limit states using Equation 3.21:

$$X_d = \frac{X_k}{\gamma_m} \tag{3.21}$$

Where:

X_k = Characteristic value of material property

γ_m = Partial material factor, as displayed in Table 3.7

Table 3.7: Partial material factors (SANS 10160-1, 2011).

Parameter	Symbol	Partial Material Factor (γ_m)				
		STR	STR-P	GEO	EQU	SLS
Friction Angle (tanφ')	$\gamma_{\phi'}$	1,0	1,0	1,25	1,25	1,0
Cohesion	$\gamma_{c'}$	1,0	1,0	1,25	1,25	1,0
Weight Density	γ_γ	1,0	1,0	1,0	1,0	1,0

3.3.2 Loads

Due to the sensitivity of the information, a load breakdown of DSS-36 could not be obtained. Available information pertained only to the self-weight of the structure. In the absence of actual values, assumptions were made to obtain estimates, which, albeit very rough, were deemed adequate for preliminary design. The following loads were required:

- Self-weight of the pedestal, $V_{k,pedestal}$
- Self-weight of the dish and supporting structure, $V_{k,dish}$
- Self-weight of the base, $V_{k,base}$
- Radial moment due to self-weight in operating conditions, $M_{k,dish}$
- Vertical load due to wind action, $V_{k,wind}$
- Horizontal load due to wind action, $H_{k,wind}$
- Radial moment due to wind action, $M_{k,wind}$

According to Mai (2015), the mass of DSS-36's pedestal excluding the base is 1 920 000 kg, which translates to a weight, $V_{k,pedestal}$, of 18 835 kN. The total weight of the dish is not specifically stated. Therefore, $V_{k,dish}$ was assumed to be equal to that of the CDSCC's 34 m DSS-12 ECHO, i.e. 2 649 kN (Imbriale, 1988). The remaining loads were scaled from characteristic values of HartRAO's 13.5 m VGOS dish, for which the following load cases were considered:

Load Case 1 – Operating conditions, elevated 50° from horizontal, 120 km/h extreme wind load.

Load Case 2 – Survival position, elevated 90° from horizontal, 200 km/h extreme wind load.

Recall from Section 2.1.2 that the design wind speed for gusts at Matjiesfontein is approximately 144 km/h, which is significantly lower than the highest wind speed considered for the VGOS dish in Load Case 2. In industry, diameter ratios are often used as order-of-magnitude indicators between dishes of different sizes (Botha, pers. comm., 2019). Therefore, a scaling factor of $R = (D/d)$ was used to extrapolate rough estimates of equivalent DSS-36 loads, where D is the diameter of DSS-36 and d is the diameter of the VGOS dish. Loads were scaled either with R^2 or with R^3 depending on whether they are proportional to area or volume, respectively, as shown in Table 3.8. Positive sign conventions are defined in Figure 3.14.

Table 3.8: Equivalent 34 m dish load estimates scaled from a 13.5 m dish.

Load	13.5 m VGOS Value		Scaling Factor (R = D/d)		34 m Dish Estimate	
Load Case 1: Operating Conditions, 120 km/h Extreme Wind Load						
$M_{k,dish}$	41	kNm	R^3	15,97	655	kNm
$V_{k,wind}$	-107	kN	R^2	6,34	-679	kN
$H_{k,wind}$	186	kN	R^2	6,34	1180	kN
$M_{k,wind}$	448	kNm	R^2	6,34	2842	kNm
Load Case 2: Survival Position, 200 km/h Extreme Wind Load						
$M_{k,dish}$	0	kNm	R^3	15,97	0	kNm
$V_{k,wind}$	96	kN	R^2	6,34	609	kN
$H_{k,wind}$	108	kN	R^2	6,34	685	kN
$M_{k,wind}$	1095	kNm	R^2	6,34	6946	kNm

Design values, X_d, were calculated for the STR, STR-P, GEO and EQU limit states using Equation 3.22:

$$X_d = \sum_{i \geq 1} (\gamma_{G,i} G_{k,i}) + \gamma_{Q,1} Q_{k,1} \tag{3.22}$$

Where:

$\gamma_{G,i}$ = Partial factor for permanent action, i

$G_{k,i}$ = Characteristic value of permanent action

$\gamma_{Q,1}$ = Partial factor for variable wind action

$Q_{k,1}$ = Characteristic value of variable wind action

Partial factors were selected from Table 3.9 for the STR, STR-P, GEO and EQU limit states. Loads were treated as either favourable or unfavourable depending on whether they act to stabilize or destabilize the structure with respect to the failure criterion under consideration. For example, loads acting in the positive z-direction (downward) were treated as unfavourable for bearing failure and as favourable for sliding and overturning failure, or vice versa for loads acting in the negative z-direction, e.g. wind uplift. Note that a higher factor of 1.5 was applied to unfavourable wind action, as recommended in SANS 10160-1 (2011) for slender structures that exhibit significant cross-wind response.

Table 3.9: Partial action factors for various limit states (SANS 10160-1, 2011).

Action		Partial Action Factor (γ_F)									
		STR		STR-P		GEO		EQU		SLS	
		Un-F	F	Un-F	F	Un-F	F	Un-F	F	Un-F	F
Permanent Actions	Self-weight	1,2	0,9	1,35	-	1,0	1,0	1,2	0,9	1,1	1,0
Variable Actions	Wind Action	1,3 1,5*	0	1,0	0	1,3 1,5*	0	1,3 1,5*	0	0,6	0
* For slender structures that exhibit significant cross-wind response											

3.3.3 Ultimate Limit State Verification

Bearing Failure

Safety against bearing failure was verified at the STR, STR-P and GE O limit states by the following condition (EN 1997-1, 2004):

$$Q_d \leq R_d \tag{3.23}$$

Where:
Q_d = Design bearing pressure
R_d = Design bearing resistance

The maximum and minimum bearing pressures were calculated using Equation 3.24:

$$Q_d = \frac{V_d}{A'} \pm \frac{M_d R}{I} \tag{3.24}$$

Where:
V_d = Design vertical load
A' = Effective area
M_d = Design radial moment
R = Foundation radius
I = Circular moment of inertia ($\frac{\pi R^4}{4}$)

Here, a negative minimum bearing pressure, i.e. causing uplift, was not allowed. The load eccentricity, e, was calculated using Equation 3.25 (EN 1997-1, 2004):

$$e = \frac{M_d}{V_d} \tag{3.25}$$

Furthermore, the following condition was imposed on the eccentricity (EN 1997-1, 2004):

$$e \leq 0.6R \tag{3.26}$$

As discussed in Section 2.6.2, only a certain elliptical portion of the total surface area of the foundation, A', is fully utilized when load is applied eccentrically. The effective area was calculated using Equation 3.27 (DNV/Risϕ, 2002):

$$A' = 2[R^2 arccos(\frac{e}{R}) - e\sqrt{R^2 - e^2}] \tag{3.27}$$

Finally, the ultimate bearing resistance was calculated as the maximum major principle stress, $\sigma_{1,max}$, using the generalized Hoek-Brown failure criterion, as shown in Equation 3.28 (Hoek and Brown, 2018):

$$\sigma_{1,max} = \sigma_{3,max} + \sigma_{ci}(m_b(\frac{\sigma_{3,max}}{\sigma_{ci}}) + s)^a \tag{3.28}$$

Where:
$\sigma_{3,max}$ = Maximum confining pressure
σ_{ci} = Unconfined Compressive Strength
m_b, s, a = Hoek-Brown rock mass constants

Sliding Failure

Safety against sliding failure was verified at the STR and GEO limit states by the following condition (EN 1997-1, 2004):

$$H_d \leq R_d \tag{3.29}$$

Where:
R_d = Design sliding resistance

Sliding resistance was calculated using Equation 3.30, where partial action factors that are applied to the design vertical load must be set to unity (EN 1997-1, 2004).

$$R_d = V_d tan\phi_d \tag{3.30}$$

Overturning Failure

Safety against overturning failure was verified at the GEO and EQU limit states by the following condition (EN 1997-1, 2004):

$$M_{dst} \leq M_{stb} \tag{3.31}$$

Where:
M_{dst} = Design value of the total destabilising moment
M_{stb} = Design value of the total stabilising moment

Total destabilizing and stabilizing moments were calculated about the bottom edge of the foundation using Equations 3.32 and 3.33, respectively:

$$M_{dst} = M_d \tag{3.32}$$

$$M_{stb} = V_d(R - e) \tag{3.33}$$

3.3.4 Serviceability Limit State Verification

Safety against excessive settlement was verified by the following condition:

$$E_d \leq S_d \tag{3.34}$$

Where:
E_d = Design value of settlement caused by the maximum SLS bearing pressure
S_d = Limiting settlement criteria

Based on a geotechnical report for the emplacement of 40 m diameter dishes at the Goldstone Deep Space Communications Complex (Pacific Soil Engineering Inc., 1979), settlement criteria of 6.35 mm and 3.18 mm were imposed on maximum settlement, δ_{max}, and differential settlement, δ_d, respectively. Equation 3.35, which has a form similar to that of Equation 2.4 of Section 2.6.2 (EN 1997-1, 2004), was proposed by Schleier (1926 cited in Wyllie, 1999) for circular foundations on homogenous isotropic rock masses. To account for the effect of discontinuities, E was substituted by the deformation modulus, E_{rm}, in Equation 3.35. Furthermore, C_d was taken as 1.00 at the centre of the foundation and 0.64 at the edge (Winterkorn and Fang, 1975):

$$\delta_{max} = \frac{C_d Q B (1 - v^2)}{E} \tag{3.35}$$

Where:
C_d = Coefficient for foundation shape and location
Q = Maximum Bearing pressure
B = Foundation diameter
v = Poisson's ratio
E = Modulus of elasticity

Chapter 4

Results and Interpretation

4.1 Concrete Aggregates

4.1.1 Grading

The grading curves of slightly weathered (W2) and highly weathered (W4) tillite are displayed in Figure 4.1. Since the analysis was performed after the third phase of crushing, both gradings were fairly uniform. This is illustrated further through low uniformity coefficients (U_a) of 1.4 and 2.8 obtained for W2 and W4 tillite, respectively. Dust contents were calculated as 0.5 % and 3.9 % for W2 and W4 tillite, respectively. While the maximum requirement of 2 % is met by W2 tillite, the dust content of W4 tillite is nearly twice the maximum limit. Consequently, W4 tillite may adversely affect the workability and water requirement of a concrete mix. Calculations are attached in Appendix A.1, Tables A.1 and A.2.

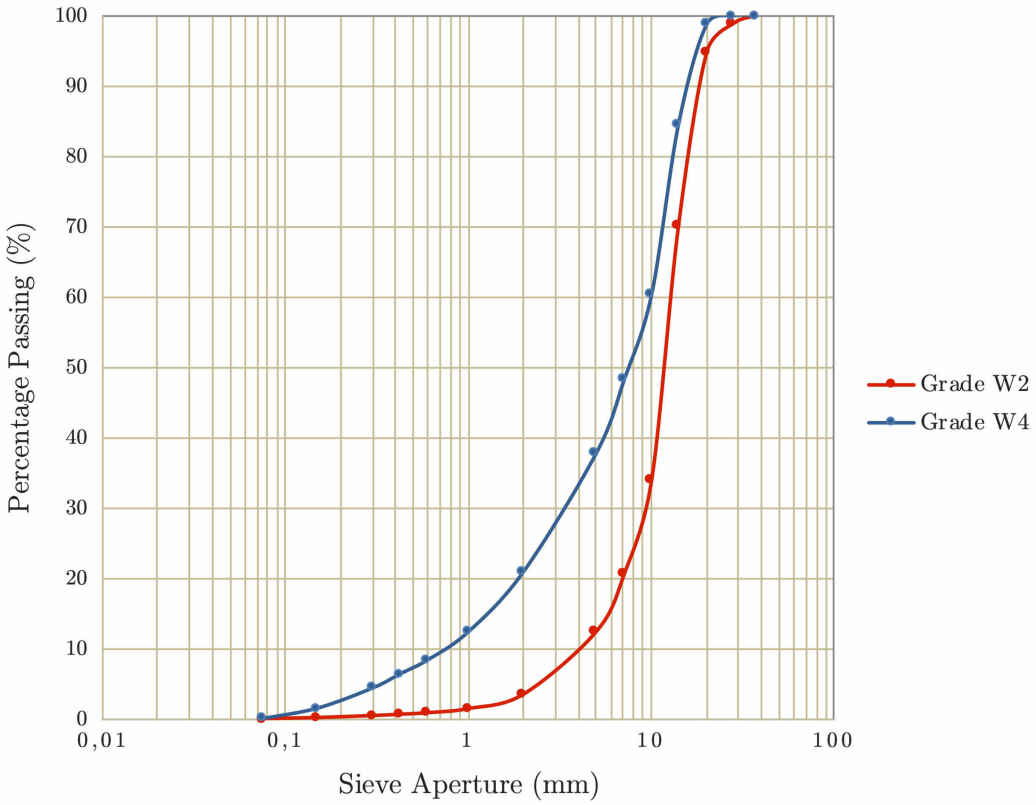

Figure 4.1: Grading curves of crushed slightly weathered (W2) and highly weathered (W4) tillite.

4.1.2 Flakiness Index (FI)

As shown in Table 4.1, Flakiness Indices (FI's) of W2 tillite were determined as 40.2 %, 36.9 % and 24.8 % subsequent to phases 1, 2 and 3 of crushing, respectively. As suggested by Brown and Marek (1996), particle shape was improved significantly with each phase, especially with the final phase, for which the reduction ratio was at its smallest. A more favourable FI of 15 % was obtained for W4 tillite, less than half the maximum limit of 35 %.

Therefore, 3 phases of crushing were sufficient to produce aggregate with acceptable flakiness values for W2 and W4 tillite. Furthermore, the 10 - 14 *mm* size fractions, which yielded FI's of 12.3 % and 10.0 % for W2 and W4 tillite, respectively, are the most favourable in terms of particle shape. An illustration of the results according to individual size fractions is shown in Figure 4.2 and calculation sheets are attached in Appendix A.2, Tables A.3 and A.4.

Table 4.1: Flakiness of different size fractions of slightly weathered (W2) and highly weathered (W4) tillite after phases of crushing.

Size fraction		W2 Tillite (%)			W4 Tillite (%)
Passing (mm)	Retained on (mm)	Phase 1 Max. ± 30 mm	Phase 2 Max. ± 20 mm	Phase 3 Max. ± 20 mm	Phase 3 Max. ± 20 mm
37,5	28,0	25,8	-	-	-
28,0	20,0	40,8	-	-	-
20,0	14,0	44,4	38,6	27,8	17,4
14,0	10,0	46,8	28,2	12,3	10,0
10,0	7,1	55,8	41,8	33,5	15,3
7,1	5,0	47,5	41,3	28,7	16,3
Overall sample FI (%)		40,2	36,9	24,8	15,0

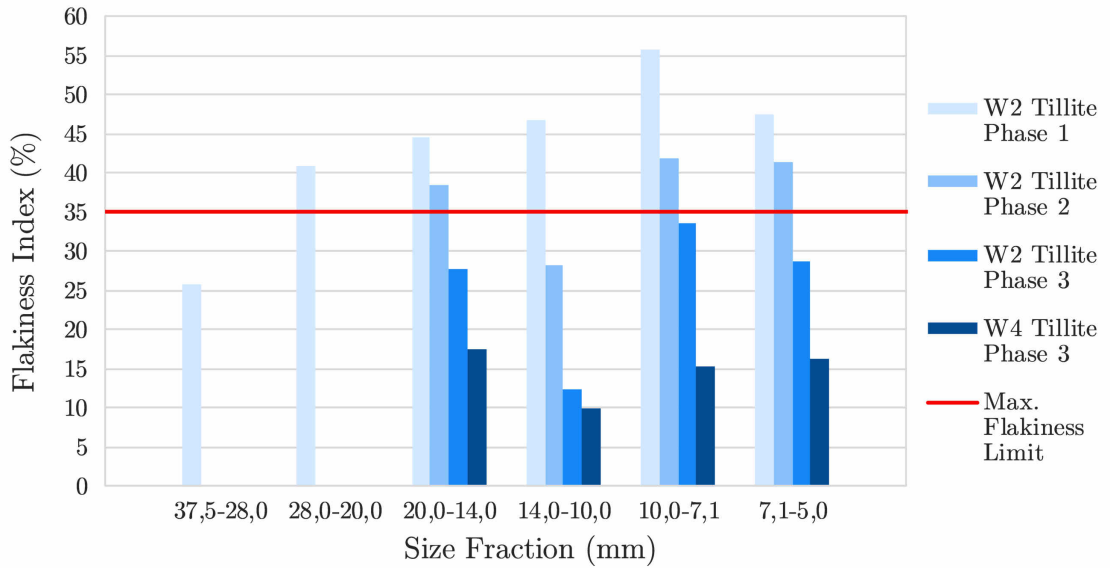

Figure 4.2: Flakiness of slightly weathered (W2) and highly weathered (W4) tillite after phases of crushing, illustrated according to individual size fractions.

4.1.3 ACV and 10%FACT Tests

As mentioned in Section 3.1.4, a maximum of 29 % and minimum of 110 kN is specified for ACV and 10%FACT, respectively. Furthermore, the wet/dry 10%FACT ratio must be greater than 56 % and the water absorption less than 2% for the elimination of degrading tillites (Paige-Green, 1980b). As shown in Table 4.2, the requirements were met by W2 tillite. Dry ACV and 10%FACT requirements were also met by W4 tillite. Surprisingly, the amount of fines produced by W4 tillite during the ACV test was only 1 % higher than that of W2 tillite, possibly since W4 tillite contained fewer flaky particles (Shipway, 1964).

However, the soaked to dry 10%FACT ratio of W4 tillite was calculated as 41 %, which is significantly lower than the recommended minimum of 56 %. Furthermore, its water absorption was calculated as 1.7 %, which is slightly below the recommended maximum of 2 % and may be regarded as marginal. The results indicate that W2 tillite is suitable for use in concrete, while the crushing resistance of W4 tillite diminishes excessively when soaked. Calculation sheets are attached in Appendix A.3, Tables A.5, A.6 and A.7.

Table 4.2: Dry and soaked Aggregate Crushing Value (ACV) and 10% Fines Aggregate Crushing Value (10%FACT) of slightly weathered (W2) and highly weathered (W4) tillite.

Parameter	Symbol	W2	W4	Unit
(Flakiness Index)		*(12,3)*	*(10.0)*	*(%)*
Dry				
Aggregate Crushing Value	ACV	11,1	12,1	%
10% Fines load	10%FACT	305	332	kN
Soaked				
Aggregate Crushing Value	ACV	14,5	21,1	%
10% Fines load	10%FACT	261	135	kN
Soaked/Dry				
Ratio wet/dry	W/D	86	41	-
Water absorbed (soaking)	W_{Abs}	0,5	1,7	%

4.1.4 Slake Durability Test

Degraded material from W2 and W4 rock lumps are displayed in Figure 4.3. In addition, before and after photographs of the rock lumps are attached in Appendix A.4. Although W2 rock lumps managed to stay intact at completion of the slake durability test, their surfaces were smoother and visible discontinuities appeared to be more pronounced. Degraded W2 tillite consisted of a few flaky particles as well as fine material with a blue colouration due to the onset of oxidation. The fineness of the material suggests that it was produced mainly through surface abrasion.

Figure 4.3: Degraded W2 (top) and W4 (bottom) tillite.

In contrast, W4 rock lumps were broken down into numerous coarse particles, which suggests that the bulk of the material was produced through internal degradation. As mentioned in Section 2.4.5, degradation in Dwyka tillite occurs primarily due to shrinkage and expansion of the clay matrix (Paige-Green, 1980b) and the amount of clay minerals increase with the degree of weathering (Dunlevey and Stephens, 1995). Hence, highly weathered W4 tillite contains more clay minerals, which in turn causes higher water absorption and expansion during wet cycles and higher shrinkage during dry cycles. As a result, W4 tillite is more susceptible to rapid degradation.

Quantitative results are summarized in Table 4.3 and illustrated in Figure 4.4. The average slake durabilities of W2 and W4 tillite were calculated as 88 % and 49 %, respectively, which indicates that durability decreases significantly with higher degrees of weathering.

Table 4.3: Fractions of W2 and W4 tillite that were not degraded to particles smaller than 20 *mm* in a slake durability test.

Sample / Parameter	W2(1)	W2(2)	W4(1)	W4(2)
Initial Mass (g)	366,2	347,9	431,5	383,9
Final Mass (g)	324,5	304,1	165,5	226,4
% Remaining	88,6	87,4	38,4	59,0
Avg. % Remaining	88,0		48,7	

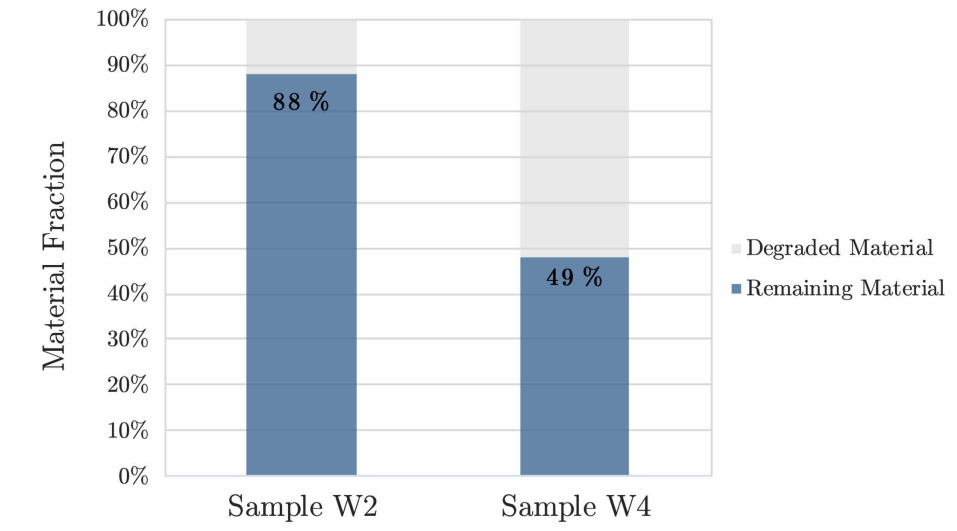

Figure 4.4: Slake durability of W2 and W4 tillite.

4.2 Rock Mass Characterization

4.2.1 Electro-Resistivity

Drilling of electrode-holes was remarkably more common on the eastern half of the site, where bedrock generally appeared to be shallower. Deviation warnings were occasionally displayed on the control unit. Small deviations could mostly be attributed to variations in soil density and moisture content. At instances of excessive deviation, for example in the order of 10 000 Ω, electrodes were adjusted or re-inserted until deviations were within acceptable limits. Data collection was limited by the available time on site. Fortunately, measurement durations decreased from 20 minutes for the initial measurement to roughly 10 minutes for each of the 22 roll-along measurements.

The electro-resistivity results of extended line 2 are displayed in Figure 4.5. Additionally, a reference image wherin the corresponding site locations and relative positions of boreholes are illustrated, is included in Figure 4.6. Greater variability was observed on the western half of the site, such as the extremely hard, intact vertical structures separated by less resistant, fractured zones between the 520 - 720 m marks.

The results indicate that unweathered (W1) tillite is shallower on the eastern half of the site, while it may be encountered at a depth of approximately 5 m on the western half. A greater degree of weathering simply suggests that the rock is more fractured and, therefore, more susceptible to the ingress of moisture. Even so, excavation to 5 m is not necessarily required, since competent slightly weathered (W2) tillite can be found at shallower depths. Moreover, the conditions may be regarded as favourable in terms of excavatability. Overall, no distinct problem-areas were identified.

NOTE: The prominent dark lines that run diagonally through the site (see Figure 4.6) are likely dolerite dikes (Kisters, pers. comm., 2019). They are known to be accompanied by thin discontinuities that allow for the ingress of moisture and, therefore, may be perceived as concentrated lines of vegetation on the surface. These intrusions are usually very strong and resistant to weathering.

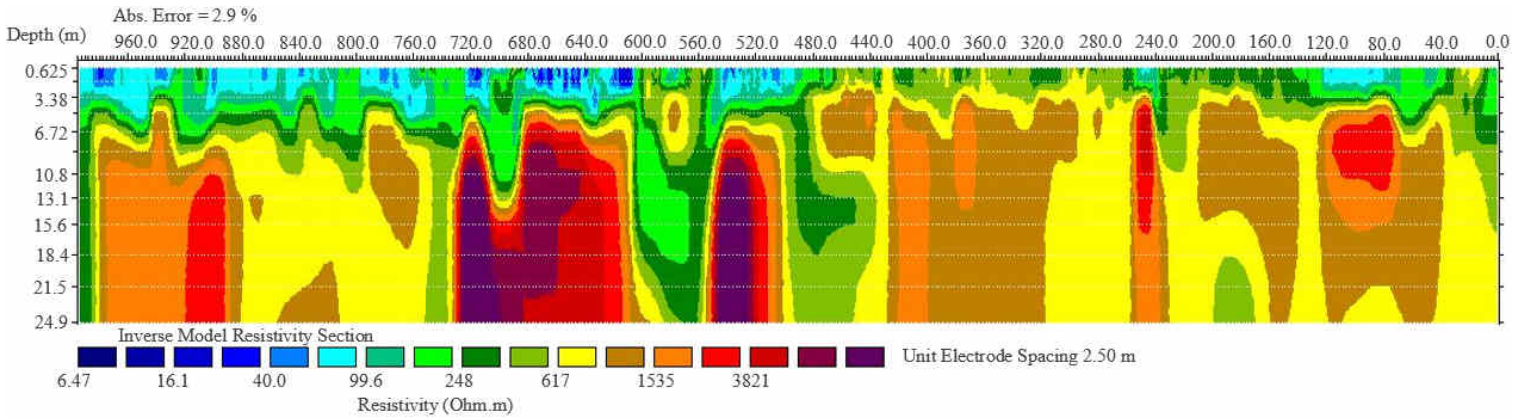

Figure 4.5: Electro-resistivity image of Extended Test Line 2; depth exaggerated by a factor of 6.5.

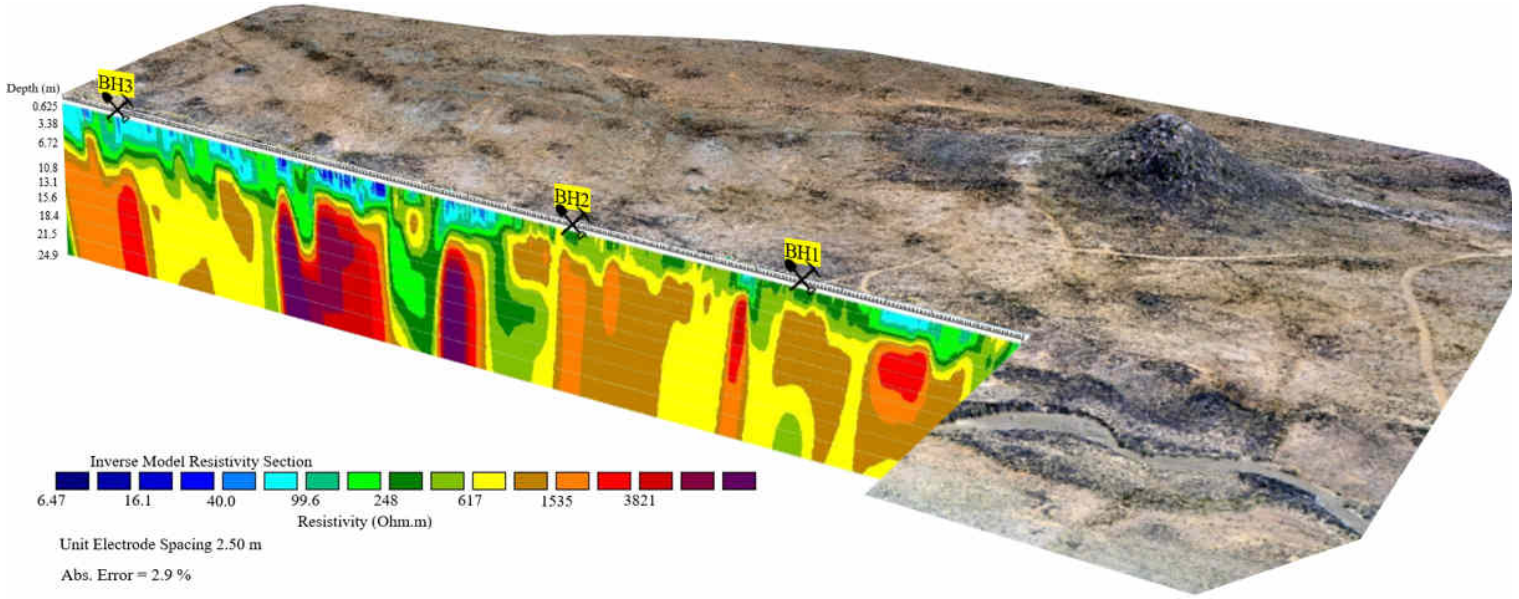

Figure 4.6: Electro-resistivity image and borehole locations of Extended Test Line 2 shown as a section through the site area; depth exaggerated by a factor of 6.5.

4.2.2 Core Logging

A photograph of the core box is displayed in Figure 4.7. The recovered core is comprised entirely of tillite. Three different phases of weathering could be distinguished by colour, namely unweathered (blueish grey), slightly weathered (olive grey) and medium weathered (yellowish brown) tillite.

The clast distribution was classified as poor across all 3 boreholes. Based on the observed clast distribution and the locations of the boreholes, it is likely that core was extracted from the clast-poor upper part of deglaciation sequence D3 (see Section 2.4.2). Detailed core descriptions are displayed in Figure 4.8. Kindly refer to Appendix B.2 for the definitions of descriptive terms.

NOTE: The core drill was able to recover only short segments at a time. Core was often left behind in the borehole, after which soil was shovelled into the borehole in an effort to improve cohesion between the pieces and the drill bit. As a result, interpretations regarding the condition, spacing and orientation of discontinuities were compromised. However, upon fitting pieces in the core box, 3 sets of discontinuities could be distinguished: sub-vertical, roughly 60° from horizontal and roughly 30° from horizontal. Discontinuity information should be verified by future investigations if so required.

Figure 4.7: Core box with tillite from boreholes BH1, BH2 and BH3.

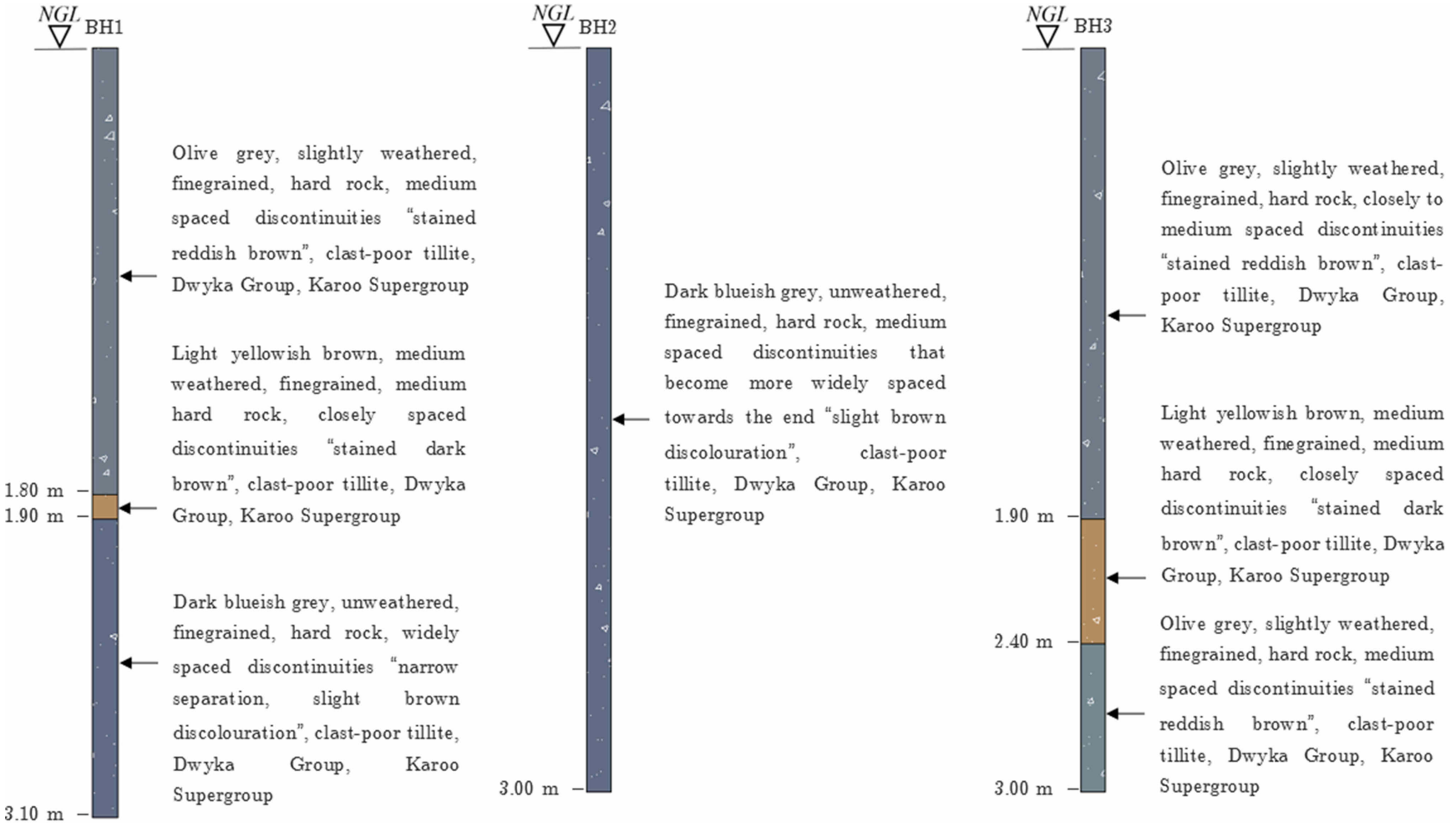

Figure 4.8: Core logs of boreholes BH1, BH2 and BH3.

4.2.3 Rock Quality Designation (RQD)

As displayed in Table 4.4, the RQD's of the core recovered from BH1, BH2 and BH3 were calculated as 81.3 % (good), 85.7 % (good) and 73.3 % (fair), respectively. When compared to the core logs in Figure 4.8, it is apparent that lower core recovery was influenced by higher overall degrees of weathering.

Table 4.4: RQD results of BH1, BH2 and BH3.

Borehole	RQD (%)	Rock Quality
BH1	81,3	Good
BH2	85,7	Good
BH3	73,3	Fair

4.2.4 Unconfined Compressive Strength (UCS) Tests

The UCS results of cylindrical specimens are summarized in Table 4.5. Discolouration was observed on certain failure planes, which indicated that those particular strengths were representative of the strength of discontinuities rather than the intact rock.

Table 4.5: UCS results of cylindrical samples from different depths and boreholes.

Sample	Borehole	Depth (m)	Failure Load (kN)	Failure Mode	UCS (MPa)
S1	BH1	2,8 - 3,1	445,6	Shear along discontinuity	56,7
S2	BH1	2,4 - 2,7	479,8	Shear along discontinuity	67,7
S3	BH3	1,0 - 1,5	404,1	Shear along discontinuity	62,1
S4	BH2	1,5 - 1,8	510,3	Intact - explosive rupture	75,1
S5	BH2	1,8 - 2,1	664,4	Intact - explosive rupture	99,9

Furthermore, UCS tests were performed for 30 cubes. After cube strengths had been adjusted for the effect of slenderness, their values were fairly similar to those obtained for cylindrical specimens from the same boreholes and depths. The average, maximum and minimum UCS values of W1, W2 and W3 tillite are displayed in Table 4.6. Additionally, specimen details are summarized in Appendix B.3.

Based on their average strengths, recovered W1 and W2 tillite samples are classified as hard to very hard rock, while W3 tillite samples are classified as medium hard rock (CLC SA, 1976). When compared to UCS values from previous studies on Dwyka tillite (Table 2.7), that of the Matjiesfontein tillites fall within the normal range, albeit on the lower end - possibly since the samples were obtained from a relatively shallow depth.

Table 4.6: Overall UCS results of cubes and cylindrical specimens.

Grade	Minimum (MPa)	Maximum (MPa)	Average (MPa)	Sample Size
W1 - (Unweathered)	56,7	121,8	86,2	15
W2 - (Slightly weathered)	52,8	111,6	74,2	17
W3 - (Medium weathered)	23,6	25,2	24,5	3

4.2.5 Rock Mass Rating (RMR)

As shown in Table 4.7, the RMR was calculated as 60. Therefore, the rock mass is classified as "Class III - Fair Rock". However, a number of conservative assumptions were made during the analysis that could underestimate the actual rock mass quality. If the rating was merely 1 point higher, for example if the actual persistance of discontinuities is less than 20 m, the RMR would have improved to "Class II - Good Rock". Therefore, it may be more appropriate to specify a range for RMR, i.e. "Fair to Good Rock".

Table 4.7: Summary of RMR results.

Parameter	Description	Rating
Intact rock strength	50 - 100 Mpa	7
Drill core quality (RQD)	75 % - 90 %	17
Spacing of Discontinuities	200 - 600 mm	10
Length/Persistence	> 20 m	0
Separation	0,1 - 1,0 mm	4
Roughness	Rough	5
Infilling/gouge	Hard < 5 mm	4
Weathering	Slightly weathered	5
Ground water	Completely dry	15
Discontinuity orientation	Fair	-7
Total rating	III - Fair rock	**60**

4.2.6 Atterberg Limits

The results of Atterberg limit tests that were performed on crushed W1, W2 and W3 tillite are summarized in Table 4.8. Due to virtually non-existent plasticity in the W1 and W2 tillites, their liquid and plastic limits could not be determined; as recommended in SANS 3001-GR10 (2013), only linear shrinkages were determined for these samples.

Resulting shrinkages were very low, which confirmed that the W1 and W2 tillite samples are non-plastic. As expected, higher plasticity was observed in medium weathered tillite. However, the results indicated that it possesses low plasticity at the most. Therefore, plasticity is not a major concern.

Table 4.8: Atterberg limit results of unweathered, slightly weathered and medium weathered tillite.

Sample →	Unweathered		Slightly Weathered		Medium Weathered	
Parameter ↓	Test 1	Test 2	Test 1	Test 2	Test 1	Test 2
Liquid limit						
Wet mass (g)	-	-	-	-	19,2	23,3
Dry mass (g)	-	-	-	-	16,7	20
Liquid limit (%)	-	-	-	-	15,0	16,5
Linear shrinkage						
Wet length (mm)	150,0	150,0	150,0	150,0	150,0	150,0
Dry length (mm)	149,5	149,5	149,0	148,5	149,0	148,0
Shrinkage (%)	0,3	0,3	0,7	1,0	0,7	1,3
Plastic limit						
Wet mass (g)	-	-	-	-	20,1	16,1
Dry mass (g)	-	-	-	-	17,3	13,7
Plastic limit (%)	-	-	-	-	16,2	17,5
Plasticity Index - PI	0,0	0,0	0,0	0,0	1,2	1,0
	Non-plastic	Non-plastic	Non-plastic	Non-plastic	Low plasticity	Low plasticity

4.3 Preliminary Foundation Design

During the iterative design process it quickly became apparent that the minimum foundation size is governed by the size of the dish and the space required inside the pedestal for the housing and comfortable operation of the telemetry equipment. The foundation of DSS-36 contains 400 m^3 of concrete (Mai, 2015) and has a height of nearly 2 m (Nagle, 2014). Therefore, the foundation would have a diameter of approximately 16 m, which was assumed as the minimum diameter for the verification of all limit states. In addition, limit states were verified for smaller diameters to illustrate the variation of governing failure modes and Factors of Safety.

4.3.1 Design Material Properties

The design values of material properties are displayed in Table 4.9. Note that only the Mohr-Coulomb parameters varied for certain limit states due to standard partial material factors.

Table 4.9: Design values of material properties.

Parameter	Symbol	Design Value, X_d	Unit
Unconfined Compressive Strength	UCS	74,2	Mpa
Modulus of Elasticity	E	26,8	GPa
Modulus of Deformation	E_{rm}	5,42	GPa
Disturbance factor	D	0,5	-
Intact rock material constant	m_i	10	-
Geological Strength Index	GSI	55	-
Hoek-Brown rock mass material constants	m_b	1,173	-
	s	0,0025	-
	a	0,504	-
Poisson's ratio	v	0,294	-
Maximum confining pressure	$\sigma_{3,max}$	3,6	MPa
Compressive strength of concrete	f_c	40	MPa
Unit weight of concrete	γ_c	24,0	kN/m³
Unit weight of overburden	γ_o	19,6	kN/m³
Unit weight of founding material	γ_{W2}	25,3	kN/m³
STR/STR-P/SLS			
Cohesion (Hoek-Brown eq.)	c	1,209	MPa
Friction angle (Hoek-Brown eq.)	φ	41	Deg.
GEO/EQU			
Cohesion (Hoek-Brown eq.)	c	0,967	MPa
Friction angle (Hoek-Brown eq.)	φ	32,8	Deg.

4.3.2 Design Loads

The resulting design loads are displayed in Table 4.10. Note that V_d applies specifically for a $\phi 16\ m$ foundation, since the self-weight of the foundation is included in the design vertical load. Detailed design load calculation sheets for all failure modes and limit states are attached in Appendix C.1.

Table 4.10: Design values of loads.

Limit State	Load Case 1: Operating Conditions 120 km/h Extreme Wind Load			Load Case 2: Survival Position 200 km/h Extreme Wind Load		
	Vd (kN)	Hd (kN)	Md (kNm)	Vd (kN)	Hd (kN)	Md (kNm)
Bearing Failure						
STR	35484	1770	5048	34466	1028	10418
STR-P	39453	1180	3726	38775	685	6946
GEO	29740	1770	4917	28722	1028	10418
Sliding Failure						
STR	25850	1770	5048	24936	1028	10418
GEO	28722	1770	4917	27809	1028	10418
Overturning Failure						
STR	25850	1770	5048	33553	1028	10418
EQU	25850	1770	5048	33553	1028	10418
GEO	28722	1770	4917	27809	1028	10418
Settlement						
SLS	32001	708	2425	31594	411	4167

4.3.3 Ultimate Limit State Verification

Bearing Failure

As mentioned in Section 3.3, a minimum FoS of 3 was imposed on bearing failure, since no standard partial material factors are available for the Hoek-Brown rock mass properties. As shown in Table 4.11, the ultimate bearing resistance was calculated as 21 MPa, which translates to an allowable pressure of 7 MPa. The estimate is deemed conservative, since it represents a relatively small fraction of the average UCS of intact W2 tillite, 74.2 MPa. The corresponding Hoek-Brown failure envelope is attached in Appendix C.2, Figure C.1.

Table 4.11: Safety bearing failure for a $\phi 16\ m$ foundation.

Parameter	Symbol	Value	Unit
Foundation diameter	φ	16	m
Ultimate bearing resistance	Rd	21	MPa
Min. Factor of Safety	FoS	3	-
Allowable bearing pressure	Qallow	7	MPa
Effective area	A'	195	m²
Max. applied bearing pressure	Qd	0,216	MPa
Actual Factor of Safety (Rd/Qd)	FoS	97	-

Bearing failure is governed by the STR limit state of Load Case 2 for diameters ranging between 1 - 9 m. Thereafter, it is governed by the STR-P limit state of Load Case 2, as the increased permanent load becomes dominant over constant variable loads. Safety against bearing failure is satisfied from a diameter of 4 m, where the FoS = 5. For a $\phi 16$ m foundation, the FoS was calculated as 97. Factors of Safety against bearing failure for various foundation diameters at the GEO, STR and STR-P limit states are attached in Appendix C.3, Figure C.2.

Sliding Failure

Safety against sliding failure is satisfied from a diameter of 1 m, where the FoS = 8. For a $\phi 16$ m foundation, the FoS was calculated as 11, as shown in Table 4.12. Failure is governed by the GEO limit state of Load Case 1, which is followed closely by the STR limit state of Load Case 1. Interestingly, the GEO limit state is more conservative for Load Case 1 due to reduced shear strength, while the STR limit state is more conservative for Load Case 2 due to reduced favourable loads. The variation illustrates how combinations of loads, material properties and partial factors can make it difficult to correctly predict the governing limit state prior to calculations. Factors of Safety against sliding failure for various foundation diameters at the GEO and STR limit states are attached in Appendix C.3, Figure C.3.

Table 4.12: Safety against sliding failure for a $\phi 16$ m foundation.

Parameter	Symbol	Value	Unit
Foundation diameter	φ	16	m
Sliding resistance	R_d	19974	kN
Min. Factor of Safety	FoS	1	-
Design horizontal load	H_d	1770	kN
Actual Factor of Safety (R_d/H_d)	FoS	11	-

Overturning Failure

Safety against overturning failure is satisfied from a diameter of 2 m, where the load eccentricity is acceptable and the FoS = 1. For a $\phi 16$ m foundation, the FoS was calculated as 18, as shown in Table 4.13. Failure is governed by the EQU limit state of Load Case 2, since unfavourable loads are factored more heavily relative to the GEO limit state. Factors of Safety against overturning failure for various foundation diameters at the EQU and GEO limit states are attached in Appendix C.3, Figure C.4.

Table 4.13: Safety against overturning failure for a $\phi 16$ m foundation.

Parameter	Symbol	Value	Unit
Foundation diameter	φ	16	m
Stabilising moment	M_{stb}	191954	kNm
Min. Factor of Safety	FoS	1	-
Max. eccentricity (0.6R)	e_{max}	4,8	m
Actual eccentricity	e	0,3	m
Destabilising moment	M_{dst}	10419	kNm
Actual Factor of Safety (M_{stb}/M_{dst})	FoS	18	-

Factors of safety for the governing limit states of the ULS failure modes are displayed in Figure 4.9. Since a higher minimum FoS of 3 was imposed on safety against bearing failure, it is indicated as the governing failure mode for foundation diameters ranging between 1 - 4 m. Furthermore, overturning failure is indicated as the governing failure mode for foundation diameters ranging between 4 - 10 m, while sliding failure is indicated as the governing failure mode for diameters larger than 10 m.

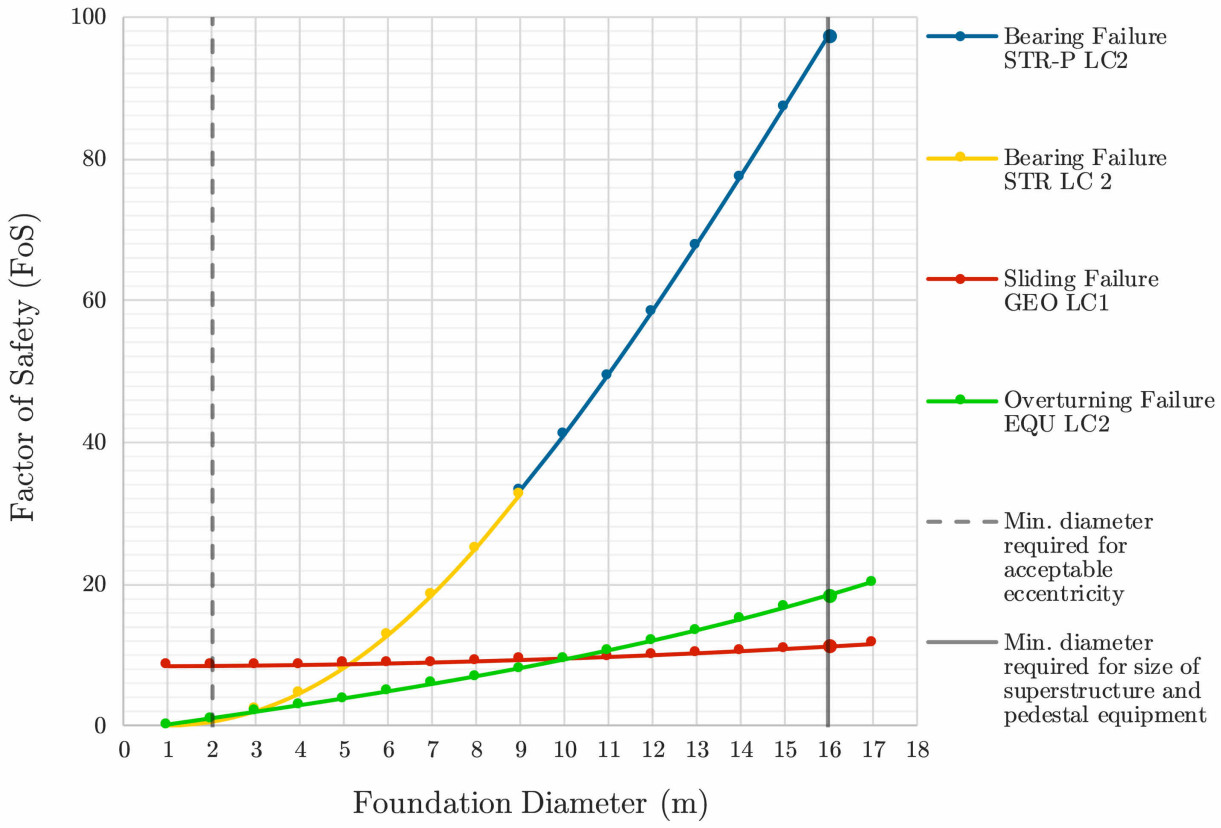

Figure 4.9: Factors of safety against the governing limit states of bearing, sliding and overturning failure.

4.3.4 Serviceability Limit State Verification

Settlement

Based on the assumed criteria, safety against excessive settlement is satisfied from a foundation diameter of 2 m, as shown in Figure 4.10. As shown in Table 4.14, the maximum settlement, δ_{max}, was calculated as 0.46 mm for a $\phi 16$ m foundation, which is safely below the maximum limit of 6.35 mm. Similarly, maximum differential settlement, δ_d, was calculated as 0.17 mm, which is below the maximum limit of 3.18 mm.

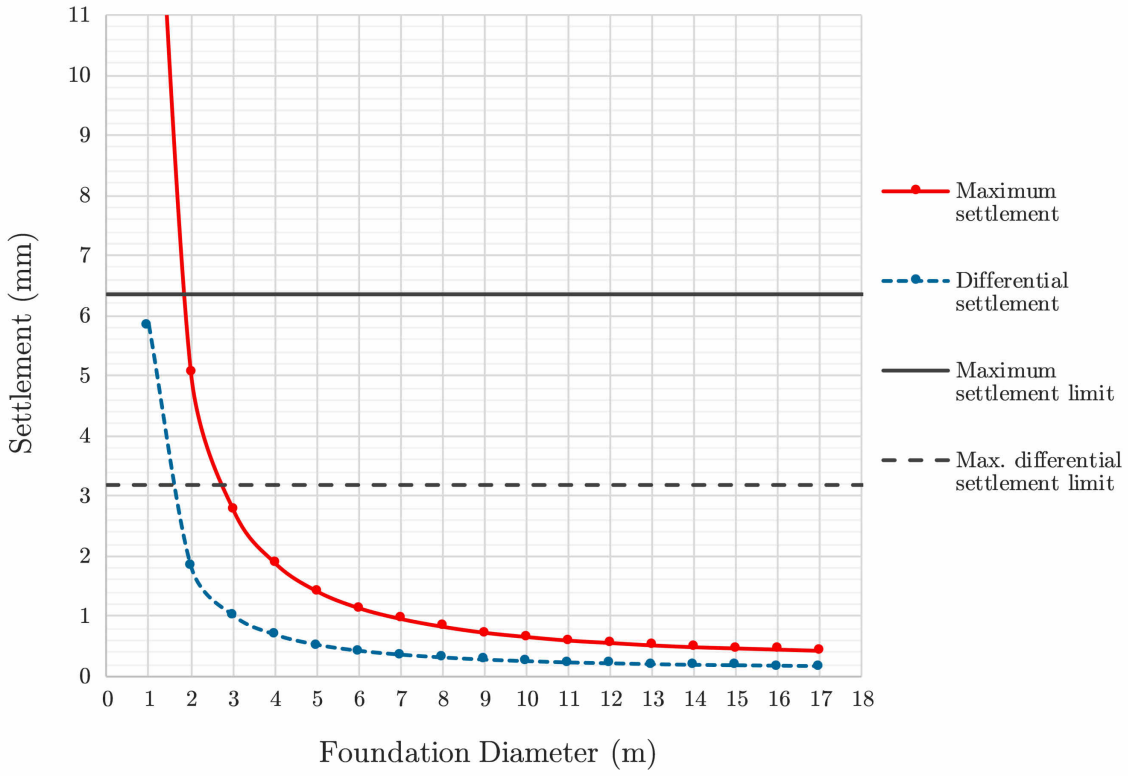

Figure 4.10: Maximum settlement and maximum differential settlement for various foundation diameters.

While the sensitivity of the results for changes in the foundation diameter is shown in Figure 4.10, it was also noted that the results are not particularly sensitive to changes in the deformation modulus; for example, if the modulus is decreased by a factor of 10, δ_{max} and δ_d would increase to 4.61 mm and 1.66 mm, respectively, which still satisfies the assumed criteria. Therefore, the results indicate no significant risk of excessive settlement. The preliminary foundation dimensions are illustrated in Figure 4.11.

Table 4.14: $\phi 16$ m foundation settlement.

Parameter	Symbol	Value	Unit
Max. applied bearing pressure	Q_d	0,171	MPa
Foundation diameter	B	16	m
Poisson's ratio	v	0,294	-
Deformation modulus	E_{rm}	5,42	MPa
Maximum settlement	δ_{max}	0,46	mm
Maximum diff. settlement	δ_d	0,17	mm

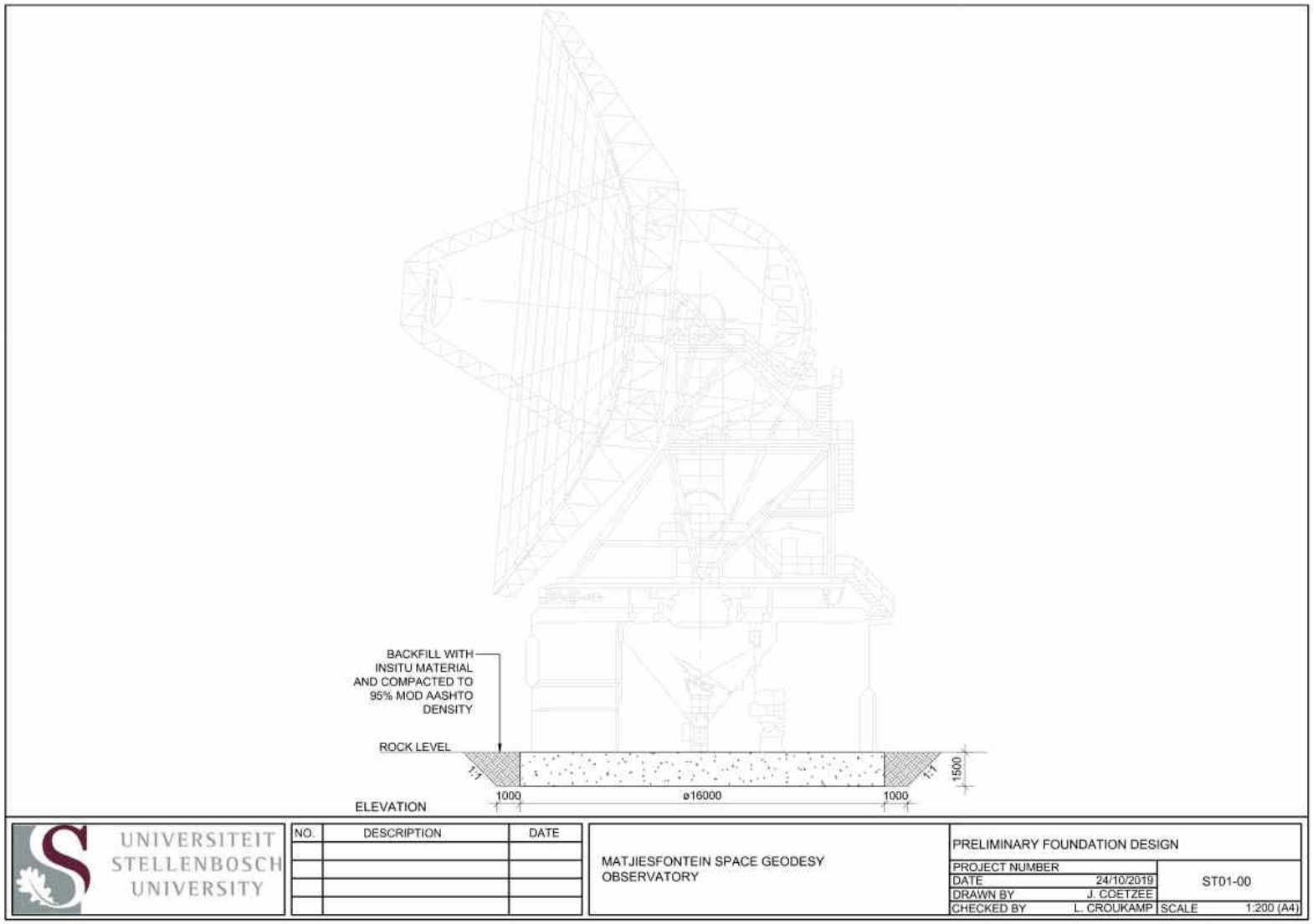

Figure 4.11: Basic technical drawing with preliminary foundation dimensions.

Chapter 5

Conclusions and Recommendations

5.1 Conclusions

5.1.1 Concrete Aggregates

Suitability

As mentioned in Section 2.5.1, previous studies have indicated that local tillite does not carry a significant risk of ASR's. In addition, the results displayed in Table 5.1 were obtained during the current study. After 3 phases of crushing, the gradings of both W2 and W4 tillite were fairly uniform. The maximum dust limit specification of 2 % was met by W2 tillite, while the dust content of W4 tillite was calculated as 3.9 %, nearly twice the maximum limit. Consequently, W4 tillite may generate excessive fines during handling and mixing, which would adversely affect the workability and water requirement of a concrete mix.

Three phases of crushing were sufficient to produce aggregate with acceptable Flakiness Indices for both W2 and W4 tillite. It was noted during crushing that W2 tillite tended to break into fragments, while W4 tillite tended to break into blocky particles. Therefore, the average flakiness of W4 tillite was remarkably lower than that of W2 tillite. The $10 - 14\ mm$ size fractions exhibited the most favourable particle shape for both samples.

Crushing resistance requirements were met by W2 tillite for dry and soaked tests. Furthermore, its water absorption was calculated as 0.5 %, well below the maximum limit of 2 %. The crushing resistance of dry W4 tillite rivalled and, in the case of the dry 10%FACT test, surpassed that of W2 tillite, possibly due to its superior particle shape. However, the low wet to dry 10%FACT ratio of W2 tillite suggests that its crushing resistance diminishes when soaked. Furthermore, the water absorption of W4 tillite was classified as marginal. Similar to dust content, the results indicate that W4 tillite may adversely affect the workability and water requirement of a concrete mix.

Table 5.1: Suitability of W2 and W4 tillite for use as coarse concrete aggregates.

Parameter	Requirement	W2 Tillite	W4 Tillite
Dust content (%)	≤ 2	0,5	3,9
Flakiness Index, FI (%)	≤ 35	24,8	15
Aggregate Crushing Value, ACV (%)	≤ 29	11,1	12,1
10%FACT value (kN)	≥ 110	305	332
Wet/dry 10%FACT ratio (%)	≥ 56	86	41
Water absorption (%)	≤ 2	0,5	1,7
Slake durability (%)	-	88	49
Overall		*Pass*	*Fail*

Key:
Pass
Marginal
Fail

Finally, the slake durability of W2 tillite was calculated as 88 %, which indicates that it would contribute to the workability of fresh concrete as well as the durability of hardened concrete. In contrast, the slake durability of W4 tillite was calculated as 49 %. Overall, the results indicate that W2 tillite would make an excellent coarse concrete aggregate. Although W4 tillite possesses certain favourable properties, i.e. particle shape and dry crushing resistance, they are negated by its unfavourable properties, i.e. dust content, soaked crushing resistance, water absorption and durability. Therefore, W4 tillite is not suitable for use in concrete.

Feasibility

It has been determined that W2 tillite is suitable for use in concrete. However, the question of whether it makes financial sense to produce aggregate locally, as opposed to procurement from alternative sources, still requires attention. Therefore, a basic feasibility was performed. The 2-storey pedestal of DSS-36 contains 1200 m^3 of concrete (Mai, 2015). As mentioned in Section 2.5.1, approximately 70 % of the volume of concrete is typically made up of aggregates (after Owens, 2013). Assuming a coarse-to-fine aggregate ratio of 1:1 (after van Wyk, 2013), roughly 420 m^3 of coarse aggregate is required for the construction of a single pedestal.

While the bulk of the rock can be supplied by excavation for the embedment of the pedestal base, it may not be enough for the construction of an entire pedestal. Fortunately, a stockpile of W1 and W2 tillite, which was excavated during the construction of government subsidy (RDP) housing, is located less than 1 km from the site area, as shown in Figure 5.1. The surface area of the stockpile was determined as 1225 m^2. Assuming a conservative average depth of 0.5 m, the stockpile could supply about 600 m^3 of raw material, enough to cover the deficit for at least 2 pedestals.

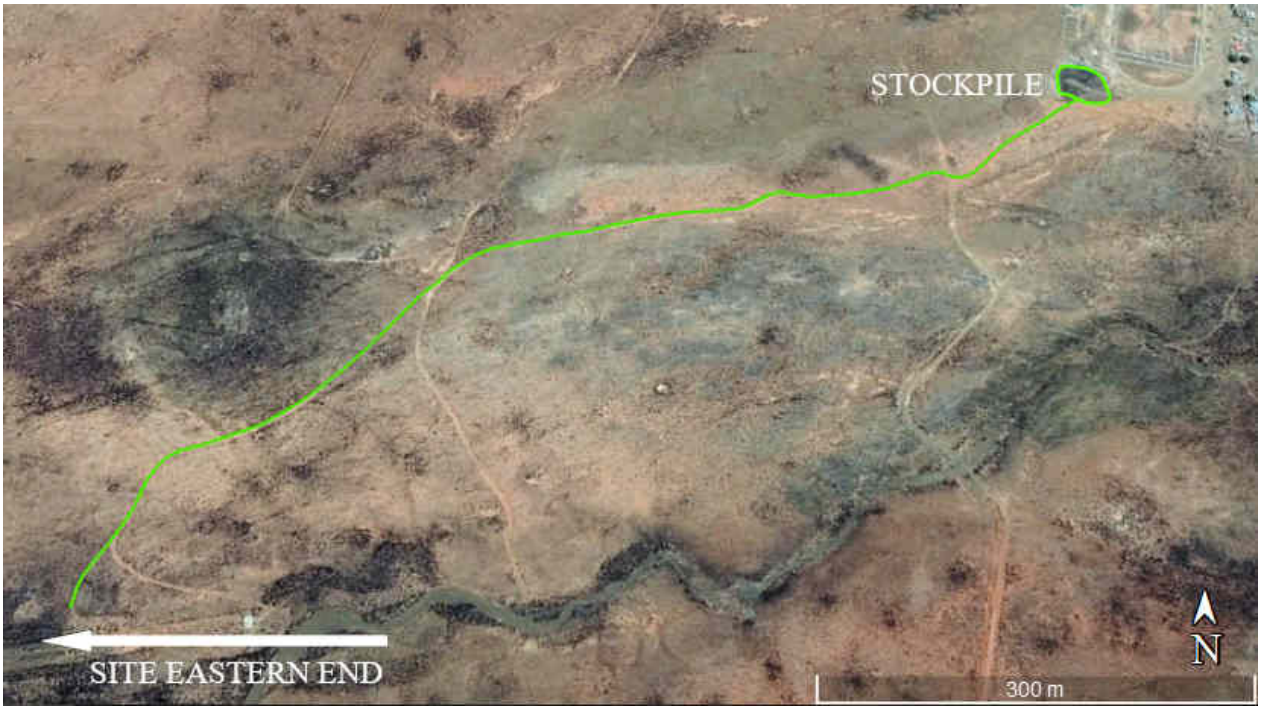

Figure 5.1: Tillite stockpile in close proximity to the site area.

Using the density of W2 tillite, 2579 kg/m^3, the required volume corresponds to 1083 tonnes of coarse aggregate. A hired mobile crusher from GLC Plant Hire has a production capacity of 200 - 220 tonnes per hour (Conradie, pers. comm., 2019). Assuming 60 % utilization, the production rate is reduced to 120 tonnes per hour. As shown in Table 5.2, the total crushing time was calculated as 9 hours, slightly longer than the minimum hiring period of 8 hours that is specified for the crusher.

Table 5.2: Approximate coarse aggregate requirements for the construction of one pedestal.

Parameter	Ref.	Calculation	Value	Unit
Concrete in DSS-36 pedestal	①	= ①	1200	m³
Roughly 70% aggregates	②	= ① x 0,7	840	m³
Ratio coarse to fine aggregates	③	= ② x 0,5	420	m³
Density of W2 tillite	④	= ④	2579	kg/m³
App. mass of coarse aggregates required	⑤	= ③ x ④	1083180	kg
App. mass of coarse aggregates required	⑥	= ⑤ ÷ 1000	1083	t
Crusher production capacity	⑦	= ⑦	120	t/hour
Required crushing time, min. 8 hours	⑧	= ⑥ ÷ ⑦	9	hours

The crusher is usually fed using an excavator and a loader. Additionally, the equipment would require transportation to and from the site area. In accordance with the rates in Table 5.3, the cost of producing coarse aggregate for one pedestal equates to R 114 830. Note that all costs are excluding VAT and may vary with time. The term “wet rate” indicates that the cost of diesel is included.

Table 5.3: Cost of producing aggregate locally (Conradie, pers. comm., 2019).

20 Ton Excavator		
Transport to site on lowbed truck & establishment	R	10 650
Operation @ 725 R/hour wet rate	R	6 525
De-establishment & transport from site on lowbed truck	R	10 650
Foton 958 Loader		
Transport to site on lowbed truck & establishment	R	10 650
Operation @ 695 R/hour wet rate	R	6 255
De-establishment & transport from site on lowbed truck	R	10 650
Crusher		
Transport to site on lowbed truck & establishment	R	20 950
Operation @ 1950 R/hour wet rate	R	17 550
De-establishment & transport from site on lowbed truck	R	20 950
Accommodation		
Accommodation @ ± 500 R/night x 3 workers	R	1 500
TOTAL	R	114 830

A quotation was obtained for the procurement of coarse aggregate from the Brewelskloof quarry (Worcester, Western Cape). As shown in Table 5.4, the cost of procurement is approximately R 714 780. Moreover, note that the cost of subsequent removal of material from the site is not included. According to the values stated here, local production can reduce the cost of coarse aggregate significantly, e.g. by roughly R 600 000 per pedestal.

Table 5.4: Cost of procurement (Diedericks, pers. comm., 2019).

Brewelskloof quarry 14 mm stone		
1083 t @ R 660/t	R	714 780

5.1.2 Rock Mass Characterization

Electro-resistivity tests indicated an apparent change in the geological features halfway along the length of the site. On the eastern half of the site, the geology is more consistent. Unweathered tillite can be encountered within 2 m below the surface, which was the case for boreholes 1 and 2. On the western half of the site, electro-resistivity results indicated that unweathered tillite can be encountered from a depth of roughly 5 m, while competent slightly weathered tillite can be found at shallower depths.

No distinct problem areas were identified. The eastern half of the site area is more favourable in terms of rock mass quality and consistency, while the western half may be slightly more favourable in terms of excavatability and the installation of services. Regardless, the site provides suitable founding conditions for the emplacement of large telemetry dishes.

Subsequently, three boreholes were drilled, namely BH1, BH2 and BH3. BH1 consisted of slightly weathered (W2) and unweathered (W1) tillite that was separated by medium weathered (W3) tillite between 1.8 – 1.9 m. BH2 consisted entirely of W1 tillite. BH3 consisted of W2 tillite separated by W3 tillite between 1.9 – 2.4 m. The rock qualities (RQD) of the core recovered from BH1, BH2 and BH3 were classified as "good", "good" and "fair", respectively.

Furthermore, the average unconfined compressive strengths (UCS) of W1, W2 and W3 tillite were determined as 86.2 MPa, 74.2 MPa and 24.5 MPa, respectively. Although the UCS of W3 is significantly lower than that of its fresher counterparts, it still classifies as medium hard rock (CLC SA, 1976) and provides substantial bearing resistance. Nonetheless, W3 tillite in BH1 and BH3 appeared in relatively thin layers, which can be removed if higher quality rock is required or preferred.

Furthermore, the average Rock Mass Rating (RMR) was determined as 60 from the recovered core, which is classifies as "fair rock" and falls short "good rock" by 1 point. However, due to conservative assumptions regarding the persistence and condition of discontinuities, a range, "fair to good rock", was deemed more representative. Finally, it was observed during testing that the texture of W3 tillite was noticeably more plastic than that of W1 and W2 tillite. However, Atterberg limit tests suggested low plasticity at the most.

5.1.3 Preliminary Foundation Design

Many of the values used in the preliminary foundation design were determined through indirect methods. Therefore, the results are intended only as rough estimates with the purpose of providing an indication of the required foundation size and potential governing factors.

The minimum foundation diameter was determined as 16 m. The design indicated that the minimum diameter is governed neither by the verified ground failure modes nor by the compressive strength of concrete in the foundation, but by the size of the dish and the space required in the pedestal for the housing and comfortable operation of telemetry equipment. The ULS failure modes, namely bearing, sliding and overturning failure, were verified at various smaller diameters to show the variation of governing failure modes and corresponding Factors of Safety (FoS).

The ultimate bearing resistance was calculated as 21 MPa using the general Hoek-Brown failure criterion. Since no standard partial material factors were available for the Hoek-Brown rock mass properties, bearing failure was subjected to a minimum FoS of 3. In contrast, sliding and overturning failure was subjected to a minimum FoS of 1, since available partial factors allowed for a complete limit states design approach. For a $\phi 16$ m foundation, FoS against bearing, sliding and overturning failure were calculated as 97, 11 and 18, respectively. Furthermore, the maximum total and differential settlements were calculated as 0.46 mm and 0.17 mm, which are safely below the assumed criteria of 6.35 mm and 3.18 mm, respectively. Therefore, the results indicate that the site is suitable for the emplacement of large telemetry dishes.

5.2 Recommendations

Concrete Aggregates

- While the use of highly weathered tillite is not recommended, unweathered and slightly weathered tillite is deemed suitable for use as coarse aggregate in concrete.
- The Washington Degradation test is recommended if further evidence of aggregate durability is required, as the results can be checked against existing criteria developed for degrading tillites (discussed in Section 2.4.6).
- Recall that slightly weathered tillite tended to splinter/flake upon impact and three phases of crushing were required to produce aggregate with suitable particle shape. Therefore, Flakiness Indices of crushed material should be evaluated prior to use.
- If an unacceptable degree of flakiness is observed, several phases of crushing should be implemented, throughout which the size reduction ratio should be kept as small as practically possible. Secondary breakdown can be facilitated by ensuring a constant feed of material to the crusher.
- For the most efficient use of materials, raw material for crushing should be sourced from excavations for the emplacement of the foundations and the installation of services.
- If excavated material contains subordinate amounts of medium weathered tillite, the material should be subjected to the appropriate tests prior to use as coarse aggregate in concrete, since medium weathered tillite may exhibit certain unfavourable properties that are similar to that of highly weathered tillite.
- To supplement excavated material, the available stockpile of unweathered and slightly weathered tillite, as discussed in Section 5.1.1, is recommended.
- The actual volume of the available stockpile should be determined using more accurate methods, e.g. drone or total station surveying.
- To verify the financial benefit of producing aggregate locally, a more extensive feasibility study should be performed using final design quantities and updated costs.

Further Investigation

- Core should be recovered from locations that are considered for emplacement.
- Higher quality drilling is recommended for the reliable characterization of discontinuities.

- Drilling should be performed to a depth that is equal to (or greater than) the diameter of the foundation to allow for core logging over the depth of influence of the foundation. Furthermore, the comparison of new core data to electro-resistivity results may allow for more reliable data extrapolation over the site area.
- The intact elastic modulus and Poisson's ratio should be determined directly, e.g. through triaxial tests.
- The in-situ deformation modulus should be determined directly, e.g. through plate jacking tests in boreholes.
- Finally, since the preliminary foundation design is largely based on assumptions, no crucial decisions should be made based solely upon its findings; it is prudent for these decisions to be based on final design calculations, which should incorporate load cases and failure criteria that apply specifically to the type of dish that is to be emplaced.

References

Addis, B. & Owens, G. 2001. *Fulton's Concrete Technology*. 8th ed. Midrand: Cement & Concrete Institute.

Alexander, M. & Mindess, S. 2005. *Aggregates in Concrete*. 1st ed. CRC Press.

Allaby, M. 2008. *Oxford Dictionary of Earth Sciences*. 3rd ed. M. Allaby (ed.). Oxford: Oxford University Press.

ASTM D 6032–96. 1997. *Standard Test Method for Determining Rock Quality Designation (RQD) of Rock Core*. West Conshohocken.

ASTM D4543–01. 2001. *Standard Practices for Preparing Rock Core Specimens and Determining Dimensional and Shape Tolerances*. West Conshohocken.

ASTM D4644-16. 2016. *Standard Test Method for Slake Durability of Shales and Other Similar Weak Rocks*. West Conshohocken.

Augustyn, A., Bauer, P., Duignan, B., Eldridge, A., Gregersen, E., McKenna, A., Petruzzello, M., Rafferty, J.P., et al. 2018. *Mid-Latitude Steppe and Desert Climate*. [Online], Available: https://www.britannica.com/science/mid-latitude-steppe-and-desert-climate#ref1092477 [2018, July 26].

Aveni, A.F. 1999. *Stairways to the stars : skywatching in three great ancient cultures*. 1st ed. Wiley. [Online], Available: https://www.wiley.com/en-us/Stairways+to+the+Stars%3A+Skywatching+in+Three+Great+Ancient+Cultures-p-9780471329763 [2018, May 11].

Bewick, R.P., Amann, F., Kaiser, P.K. & Martin, C.D. 2015. Interpretation of UCS Test Results for Engineering Design. In Montreal: International Society for Rock Mechanics *The 13th International Congress of Rock Mechanics*.

Bieniawski, Z.T. 1989. *Engineering Rock Mass Classifications: a Complete Manual for Engineers and Geologists in Mining, Civil and Petroleum Engineering*. 1st ed. Toronto: John Wiley & Sons, Inc.

Bieniawski, Z.T. & Bernede, M.J. 1979. Suggested Methods for Determining the Uniaxial Compressive Strength and Deformability of Rock Materials. *International Journal of Rock Mechanics and Mining Sciences & Geomechanics Abstracts*. 16(2).

Bond, A. & Harris, A. 2008. *Decoding Eurocode 7*. 1st ed. T. Moore (ed.). New York: Taylor & Francis.

Bothma, S. 2015. Geotechnical Properties and Foundation Requirements for the Satellite and Lunar Laser Ranger at the Matjiesfontein Space Geodesy Observatory. Stellenbosch University.

Bowles, J.E. 1996. *Foundation Analysis and Design*. 5th ed. Singapore: McGraw-Hill.

Brink, A.B.A. 1983. *Engineering Geology of Southern Africa Volume 3: The Karoo Sequence*. Silverton: Building Publications.

Brophy, S. 2015. *Minor Matjiesfontein earthquake groundbreaking for SA's ability to measure seismic activity*. [Online], Available: https://www.traveller24.com/Explore/minor-matjiesfontein-earthquake-groundbreaking-for-sas-ability-to-measure-seismic-activity-20151204 [2018, May 20].

Brown, R.H. & Marek, C.R. 1996. *Effect of Crusher Operation on Coarse Aggregate Shape*.

Buser, B. 2014. *May 2014 Newsletter - Cape Town*. [Online], Available:

http://samilitaryhistory.org/14/c14mayne.html [2018, May 22].

Chen, Q. & Yin, T. 2018. Should the Use of the Rock Quality Designation be Discontinued in the Rock Mass Rating System? *Rock Mechanics and Rock Engineering*.

CLC SA. 1976. A Guide to Core Logging for Rock Engineering. In Core Logging Committee of the South Africa Section of The Association of Engineering Geologists (ed.). Johannesburg *Symposium on Exploration for Rock Engineering*.

Coetzee, J. 2017. A Preliminary Geotechnical Investigation for the Placement of Radio Astronomical Dishes at Matjiesfontein.

Combrinck, L. 2007. *White Paper towards the Establishment of the International Institute for Space Geodesy and Earth Observation (IISGEO)*.

Croukamp, L., Combrinck, L. & Fourie, S. 2014. Geotechnical investigations at Matjiesfontein Space Geodesy Observatory for the emplacement of geodetic and geoscience instruments. In Johannesburg *Inkaba yeAfrika and !Khure Afrika 10th Annual Conference*.

Das, B.M. & Sivakugan, N. 2017. *Principles of Foundation Engineering*. 9th ed. Boston: Cengage.

Deffree, S. 2017. *German rocket is 1st to reach space, October 3, 1942*. [Online], Available: https://www.edn.com/electronics-blogs/edn-moments/4397678/German-rocket-is-1st-to-reach-space--October-3--1942 [2018, May 11].

DeVille Wickens, H. n.d. *Matjiesfontein 1:50 000 Field Sheet*.

DeVille Wickens, H. & Cole, D. 2017. *Stratigraphic Evolution of the Dwyka and Ecca Groups, Southwestern Karoo Basin*.

DNV/Risø. 2002. *Guidelines for Design of Wind Turbines*. 2nd ed. Copenhagen: Det Norske Veritas & Risø National Laboratory.

Dunford, B. 2012. *Goldstone*. [Online], Available: http://www.ridingwithrobots.org/2012/11/goldstone/ [2018, May 11].

Dunlevey, J.N. & Stephens, D.J. 1995. The Use of Dwyka Group Diamictite as Crushed Aggregate in Natal. *Civil engineering : Magazine of the South African Institution of Civil Engineers*. 37(2).

Eff-Darwich, A., Rodriguez-Losada, J.A., De la Nuez, J., Hernandez-Gutierrez, L.E. & Romero-Ruiz, C. 2010. Comparative analysis of the impact of geological activity on the structural design of telescope facilities in the Canary Islands, Hawaii and Chile. *Monthly Notices of the Royal Astronomical Society*. 407(3).

EN1997-1. 2004. *Eurocode 7: Geotechnical Design - Part 1: General Rules*. CEN.

ESA/Hubble. 2006. *Hubble's Sharpest View of the Orion Nebula*. [Online], Available: https://www.spacetelescope.org/images/heic0601a/ [2018, May 11].

Fernandes, I. & Broekmans, M.A.T.M. 2013. Alkali–Silica Reactions: An Overview. Part I. *Metallography, Microstructure, and Analysis volume*. 2.

Frandsen, D. 2018. *History of Matjiesfontein – The Karoo, South Africa*. [Online], Available: https://www.karoo-southafrica.com/koup/matjiesfontein/history-of-matjiesfontein/ [2018, May 22].

Geertsema, A.J. 2000. *The Engineering Characteristics of Important Southern African Rock Types with Emphasis on Shear Strength of Concrete Dam Foundations*. Pretoria.

Gf Instruments. 2019. *Short guide for resistivity and induced polarization tomography*. Brno: Gf Instruments, s.r.o.

Gf Instruments. n.d. *ARES - Automatic Resistivity System*. [Online], Available: http://www.gfinstruments.cz/index.php?menu=gi&cont=ares_ov [2019, August 17].

Harikrishna, M.S. 2018. [Online], Available: https://www.slideshare.net/HarikrishnaMS1/deterioration-of-concrete.

Harris Geospatial Solutions Inc. 2018. *Atmospheric Windows and Optical Sensors*. [Online], Available: http://www.harrisgeospatial.com/Support/SelfHelpTools/HelpArticles/HelpArticles-Detail/TabId/2718/ArtMID/10220/ArticleID/17333/Atmospheric-Windows-and-Optical-Sensors.aspx [2018, May 11].

Hoek, E. & Brown, E.T. 1988. The Hoek-Brown Failure Criterion - a 1988 Update. In J.H. Curran (ed.). Toronto: Civil Engineering Department University of Toronto *15th Canadian Rock Mechanics Symposium*.

Hoek, E. & Brown, E.T. 1997. Practical Estimates of Rock Mass Strength. *International Journal Rock Mechanics Mining Science*.

Hoek, E. & Brown, E.T. 2018. The Hoek–Brown failure criterion and GSI – 2018 edition. *Journal of Rock Mechanics and Geotechnical Engineering*. 11(3).

Hoek, E. & Diederichs, M.S. 2006. Empirical estimation of rock mass modulus. *International Journal of Rock Mechanics and Mining Sciences*. 43(2).

Hoek, E., Carranza-Torres, C. & Corkum, B. 2002. Hoek-Brown failure criterion - 2002 Edition. In Toronto *NARMS-TAC Conference*.

Iffat, S. 2015. Relation Between Density and Compressive Strength of Hardened Concrete. *Concrete Research Letters*. 6(4).

Imbriale, W.A. 1998. *Evolution of the Deep Space Network 34-m Diameter Antennas*. Pasadena.

ISECG. 2013. [Online], Available: https://www.nasa.gov/sites/default/files/files/Benefits-Stemming-from-Space-Exploration-2013-TAGGED.pdf [2018, May 14].

ISRM. 1985. Suggested Method for Determining Point Load Strength Index. *International Journal of Rock Mechanics and Mining Sciences & Geomechanics Abstracts*. 22(2).

Jaeger, C. 1979. *Rock Mechanics and Engineering*. 2nd ed. New York: Cambridge University Press.

Jaeger, J.C., Cook, N.G.W. & Zimmerman, R.W. 2007. *Fundamentals of Rock Mechanics*. 4th ed. Oxford: Blackwell Publishing.

Janse van Rensburg, C. 2017. Site Characterization and Foundation Design for the Emplacement of Radio Telescope Antennas at the Matjiesfontein Space Geodesy Observatory. Stellenbosch University.

Jebasingh, R.A.I. 2016. *Landforms Produced by Glaciers*. [Online], Available: http://officersiasacademy.blogspot.com/2016/04/landforms-created-by-glacier.html [2018, June 25].

Keurkloof Karoo Farm Accommodation. 2018. *Experience a Karoo Farm*. [Online], Available: https://keurkloof.co.za/karoo-guest-farm-south-africa/ [2018, May 22].

Khan, S. & Dhobale, S.B. 2018. Effect of Flaky Aggregates on the Strength and Workability of Concrete. *International Research Journal of Engineering and Technology (IRJET)*. 5(9).

Kijko, A., Graham, G., Bejaichund, M., Roblin, D. & Brandt, M.B.C. 2003. *Probabilistic Peak Ground Acceleration and Spectral Seismic Hazard Maps for South Africa*.

Ko, E. 2017. *NASA Canberra Deep Space Communications Complex*. Australia: YouTube. [Online], Available: https://www.youtube.com/watch?v=rQwQHX_6GEI.

Kruger, A.C., Retief, J.V. & Goliger, A.M. 2017. Development of an updated fundamental basic wind speed map for SANS 10160-3. *Journal of The South African Institution of Civil Engineering*. 59(4):12–25.

Laingsburg Municipality. 2017. *Final 5 Year Review Integrated Development Plan*. Laingsburg.

Mai, T. 2015. *Deep Space Station 36 Construction Gallery*. [Online], Available: https://www.nasa.gov/directorates/heo/scan/services/networks/DSS36_antenna_gallery.html [2019, September 16].

Mai, T. 2018. *Deep Space Network*. NASA. [Online], Available: https://www.nasa.gov/directorates/heo/scan/services/networks/dsn [2018, May 11].

Martin, A. 2017. *How much do governments spend on space science?* [Online], Available: http://www.alphr.com/space/1005737/how-much-do-governments-spend-on-space-science [2018, May 14].

Mindess, S., Young, J.F. & Darwin, D. 2003. *Concrete*. 2nd ed. New Jersey: Prentice Hall.

Moskowitz, C. 2010. *Truth Behind the Photos: What the Hubble Space Telescope Really Sees*. [Online], Available: https://www.space.com/8059-truth-photos-hubble-space-telescope-sees.html [2018, May 10].

Mukai, K. 2016. *Thirty Years of Space VLBI*. [Online], Available: https://asd.gsfc.nasa.gov/blueshift/index.php/2016/07/25/thirty-years-of-space-vlbi/ [2018, May 14].

Nagle, G. 2014. *Growing a Garden of Dishes*. [Online], Available: https://blog.csiro.au/growing-a-garden-of-dishes/ [2019, September 21].

Nan, R., Peng, B., Qiu, Y., Ren, G., Wu, S., Zheng, Y., Zhu, W., Wu, J.H., et al. 2002. Kilometer-square Area Radio Synthesis Telescope KARST. [Online], Available: https://www.skatelescope.org/uploaded/8481_17_memo_Nan.pdf [2018, May 11].

NASA. 2007. *The Pioneer Missions*. National Aeronautics and Space Administration (NASA). [Online], Available: https://www.nasa.gov/centers/ames/missions/archive/pioneer.html [2018, May 11].

NASA JPL. n.d. *Voyager - Planetary Voyage*. [Online], Available: https://voyager.jpl.nasa.gov/mission/science/planetary-voyage/ [2018, May 11].

Owens, G. 2013. *Fundamentals of Concrete*. 3rd ed. Midrand: Cement and Concrete Institute.

Pacific Soil Engineering Inc. 1979. *Geotechnical Investigation Report for Proposed Array of Six 40-Meter Diameter Antennas*. Pasadena.

Paige-Green, P. 1980a. The Clay Mineralogy of Dwyka Tillite in Southern Africa and its Effect on the Geotechnical Properties. *South African Journal of Geology*. 83(2):291–296. [Online], Available: https://journals.co.za/docserver/fulltext/sajg/83/2/1205.pdf?expires=1549457227&id=id&accname=guest&checksum=980FBDC89DEAB066A32CDA83336A1DFD [2019, February 06].

Paige-Green, P. 1980b. Durability Testing of and Specifications for Degrading Dwyka Tillite in Southern Africa. In Accra: National Institute for Transport & Road Research (CSIR) *Seventh Regional Conference for Africa on Soil Mechanics and Foundation Engineering*.

Paige-Green, P. 1984. The Use of Tillite in Flexible Pavements in Southern Africa. In Harare: National Institute for Transport & Road Research (CSIR) *Eighth Regional Conference for Africa on Soil Mechanics and Foundation Engineering*.

Redd, N.T. 2018. *NASA's Deep Space Network: How Spacecraft Phone Home*. [Online], Available: https://www.space.com/39578-deep-space-network.html [2018, May 11].

Reimers, R. 2015. *How we figured out that Earth goes around the sun*. USA: YouTube - SciShow Space. [Online], Available: https://www.youtube.com/watch?v=khIzr6610cQ.

Retief, J.V., Dunaiski, P.E., Day, P.W., Holicky, M., Goliger, A.M., Kruger, A.C., Wium, J.A. & Dymond, J.S. 2009. *Background to SANS 10160*. 1st ed. J.V. Retief & P.E. Dunaiski (eds.). Stellenbosch: SUN Media.

Rocscience Inc. 2002. [Online], Available: www.rocscience.com.

SANRAL. 2014. *South African Pavement Engineering Manual Chapter 10: Pavement Design*. 2nd ed. South African National Roads Agency Ltd. (SANRAL). [Online], Available: www.nra.co.za [2019, February 13].

SANS 10160-1. 2011. *South African National Standard Basis of Structural Design and Actions for Buildings and Industrial Structures - Part 1: Structural Design*. Pretoria: SABS Standards Division.

SANS 10160-4. 2017. *Basis of Structural Design and Actions for Buildings and Industrial Structures Part 4: Seismic Actions and General Requirements for Buildings*. Pretoria.

SANS 1083. 2017. *Aggregates from Natural Sources - Aggregates for Concrete*. Pretoria.

SANS 3001-AG1. 2014. *Civil engineering test methods Part AG1: Particle size analysis of aggregates by sieving*. Pretoria.

SANS 3001-AG10. 2012. *Civil engineering test methods Part AG10: ACV (aggregate crushing value) and 10 % FACT (fines aggregate crushing test) values of coarse aggregates*. Pretoria.

SANS 3001-AG16. 2013. *Determination of the Durability Mill Index Values for Aggregates*. Pretoria.

SANS 3001-AG4. 2015. *Civil engineering test methods Part AG4: Determination of the flakiness index of coarse aggregate*. Pretoria.

SANS 3001-GR10. 2013. *Civil engineering test methods Part GR10: Determination of the one-point liquid limit, plastic limit, plasticity index and linear shrinkage*. Pretoria.

Schoneman, A. 2018. *Plucking (Glacier Erosion)*. [Online], Available: https://www.studyblue.com/#flashcard/flip/14525687 [2019, February 12].

Shipway, C.H. 1964. A Study of the Aggregate Crushing Test. In *2nd ARRB Conference 2(2)*.

Shuttleworth, M. 2010a. *Mesopotamian Astronomy*. [Online], Available: https://explorable.com/mesopotamian-astronomy [2018, May 11].

Shuttleworth, M. 2010b. *Ancient Astronomy, Science And The Ancient Greeks*. [Online], Available: https://explorable.com/greek-astronomy [2018, May 11].

SKA South Africa. 2018. *Everything You Want to Know About the SKA*. [Online], Available: http://www.ska.ac.za/about/faqs/ [2018, May 14].

Snyderskloof. 2013. *Snyderskloof Matjiesfontein Karoo Cottage*. [Online], Available: http://www.snyderskloof.co.za/ [2018, May 26].

Steenkamp, N.C. 2014. Challenges of Developing a Ventilation Shaft in Kalahari and Karoo Formations, Northern Cape, South Africa. In Adelaide *12th AusIMM Underground Operators Conference*.

TMH5. 1981. *Technical Methods for Highways 5: Sampling Methods for Road Construction Materials MD2 - Division of a Sample by Quartering*. Pretoria.

TRH3. 2007. *Technical Recommendations for Highways 3: Design and Construction of Surfacing Seals*. Pretoria.

Warren, A. 2016. *Say hello to NASA's latest spacecraft tracking antenna*. [Online], Available: https://blog.csiro.au/nasa-latest-spacecraft-tracking-antenna/ [2019, September 16].

Winterkorn, H.F. & Fang, H.Y. 1975. *Foundation Engineering Handbook*. New York: Van Nostrand Reinhold.

Van Wyk, P. 2013. Rock Mechanics for Construction of the Gravimeter Vault at the Matjiesfontein Space Geodesy and Earth Observation Observatory. Stellenbosch University.

Wyllie, D.C. 1999. *Foundations on Rock*. 2nd ed. London: E & FN Spon.

Zinan, C. 2019. *Earth's largest radio telescope identifies 86 pulsars*. [Online], Available: https://www.telegraph.co.uk/china-watch/technology/china-fast-telescope-discoveries/ [2019, October 12].

Appendices

Appendix A

Concrete Aggregates

A.1 Grading

Table A.1: Grading calculations for crushed slightly weathered (W2) tillite.

Sieve Aperture (mm)	Mass Retained (mm)	Cum. mass retained (g)	% Retained	% Passing
37,5	0	0	0	100
28	42	42	1	99
20	146	188	4	95
14	895	1082	25	70
10	1307	2389	36	34
7,1	484	2873	13	21
5	298	3170	8	12
2	323	3493	9	3
1	75	3568	2	1
0,6	21	3589	1	1
0,425	8	3597	0	1
0,3	7	3604	0	0
0,15	10	3614	0	0
0,075	6	3620	0	0
Pan	1	3620	0	0
Mass after sieving - M_{Ff} (g)	3637			
Dried sample mass - a (g)	3638	Dust in pan - c (g)	1	
Dried mass after wet sieving - b (g)	3620	Dust content - 100(a - b +c) / M_{Ff} (%)	0,5	

Table A.2: Grading calculations for crushed highly weathered (W4) tillite.

Sieve Aperture (mm)	Mass Retained (mm)	Cum. mass retained (g)	% Retained	% Passing
37,5	0	0	0	100
28	0	0	0	100
20	40	40	1	99
14	480	520	14	85
10	812	1333	24	60
7,1	407	1739	12	48
5	353	2092	10	38
2	569	2661	17	21
1	288	2949	9	12
0,6	135	3084	4	8
0,425	67	3151	2	6
0,3	68	3219	2	4
0,15	97	3316	3	2
0,075	50	3366	1	0
Pan	2	3368	0	0
Mass after sieving - M_{Ff} (g)	3502			
Dried sample mass - a (g)	3488	Dust in pan - c (g)	2	
Dried mass after wet sieving - b (g)	3354	Dust content - 100(a - b +c) / M_{Ff} (%)	3,9	

A.2 Flakiness Index

Table A.3: Flakiness Index calculations for slightly weathered (W2) tillite.

Size fraction		Slot size		Mass of fraction		Flakiness Index (FI)	
Passing (mm)	Retained (mm)	Length (mm)	Width (mm)	Total mass (g)	Mass passing slot (g)		
Phase 1: Maximum stone size approximately 30 mm							
37,5	28,0	75,0	18,7	1034,3	266,7	25,8	%
28,0	20,0	50,0	14,0	998,2	407,5	40,8	%
20,0	14,0	40,0	10,0	722,9	321,2	44,4	%
14,0	10,0	27,0	7,0	563,2	263,4	46,8	%
10,0	7,1	20,0	5,0	239,2	133,5	55,8	%
7,1	5,0	15,0	3,5	509,1	241,9	47,5	%
			TOTAL	4066,9	1634,2	**40,2**	%
Phase 2: Maximum stone size approximately 20 mm							
37,5	28,0	75,0	18,7	0,0	0,0	-	%
28,0	20,0	50,0	14,0	0,0	0,0	-	%
20,0	14,0	40,0	10,0	778,6	300,3	38,6	%
14,0	10,0	27,0	7,0	551,4	155,4	28,2	%
10,0	7,1	20,0	5,0	261,8	109,4	41,8	%
7,1	5,0	15,0	3,5	512,5	211,7	41,3	%
			TOTAL	2104,3	776,8	**36,9**	%
Phase 3: Maximum stone size approximately 20 mm							
37,5	28,0	75,0	18,7	0,0	0,0	-	%
28,0	20,0	50,0	14,0	0,0	0,0	-	%
20,0	14,0	40,0	10,0	753,7	209,3	27,8	%
14,0	10,0	27,0	7,0	515,6	63,4	12,3	%
10,0	7,1	20,0	5,0	265,0	88,7	33,5	%
7,1	5,0	15,0	3,5	511,2	146,5	28,7	%
			TOTAL	2045,5	507,9	**24,8**	%

Table A.4: Flakiness Index calculations for highly weathered (W4) tillite.

Size fraction		Slot size		Mass of fraction		Flakiness Index (FI)	
Passing (mm)	Retained (mm)	Length (mm)	Width (mm)	Total mass (g)	Mass passing slot (g)		
Phase 3: Maximum stone size approximately 20 mm							
37,5	28,0	75,0	18,7	0,0	0,0	-	%
28,0	20,0	50,0	14,0	0,0	0,0	-	%
20,0	14,0	40,0	10,0	756,5	131,8	17,4	%
14,0	10,0	27,0	7,0	514,1	51,6	10,0	%
10,0	7,1	20,0	5,0	256,2	39,3	15,3	%
7,1	5,0	15,0	3,5	508,3	83,0	16,3	%
			TOTAL	2035,1	305,7	**15,0**	%

A.3 ACV and 10%FACT Tests

Table A.5: Dry ACV and 10%FACT calculations.

Parameter	Symbol	W2	W4	Unit
1st Point				
Max. load	F1	400,0	400,0	kN
Sample mass	M1	2610,0	2676,0	g
Passing 2 mm	M1P	290,6	324,0	g
Aggregate Crushing Value	ACV	11,1	12,1	%
2nd Point				
Max. load	F2	359,3	330,4	kN
Sample mass	M2	2627,8	2649,0	g
Mass passing 2 mm	M2P	309,7	262,0	g
Percentage passing 2 mm	P2	11,8	9,9	%
3rd Point				
Max. load	F3	304,8	334,0	kN
Sample mass	M3	2667,1	2691,0	g
Passing 2 mm	M3P	259,4	269,0	g
Percentage passing 2 mm	P3	9,7	10,0	%
Acceptance condition	ε	1,6	1,5	-
	|P3-10|	0,3	0,0	%
	|P2-10|	1,8	0,1	%
10% Fines load	10%FACT	**305**	**332**	kN

Table A.6: Soaked ACV and 10%FACT calculations.

Parameter	Symbol	W2	W4	Unit
1st Point				
Max. load	F1	400,0	400,0	kN
Dry sample mass	M	2618,7	2678,8	g
Surface dry soaked mass	M1	2629,3	2725,4	g
Passing 2 mm	M1P	379,2	565,0	g
Aggregate Crushing Value	ACV	14,5	21,1	%
2nd Point				
Max. load	F2	276,2	193,2	kN
Dry sample mass	M	2633,4	2686,2	g
Surface dry soaked mass	M2	2647,1	2729,0	g
Mass passing 2 mm	M2P	297,4	391,0	g
Percentage passing 2 mm	P2	11,2	14,3	%
3rd Point				
Max. load	F3	245,9	134,8	kN
Dry sample mass	M	2653,8	2679,4	g
Surface dry soaked mass	M3	2666,5	2727,0	g
Passing 2 mm	M3P	270,4	275,0	g
Percentage passing 2 mm	P3	10,1	10,1	%
Acceptance condition	ε	1,3	1,1	-
	|P3-10|	0,1	0,1	%
	|P2-10|	1,2	4,3	%
10% Fines load	10%FACT	261	135	kN

Table A.7: Water absorption and wet/dry 10%FACT calculations.

Parameter	Symbol	W2	W4	Unit
Wet/Dry Relationship				
Ratio wet/dry	W/D	86	41	%
Avg. mass dry agg.	M_{avg}	2635,3	2681,5	g
Avg. mass surface dry soaked	M_{iavg}	2647,6	2727,1	g
Water absorbed (soaking)	W_{Abs}	0,5	1,7	%

A.4 Slake Durability

Table A.8: Photographs of slightly weathered (W2) tillite rock lumps before and after 5 wet/dry cycles.

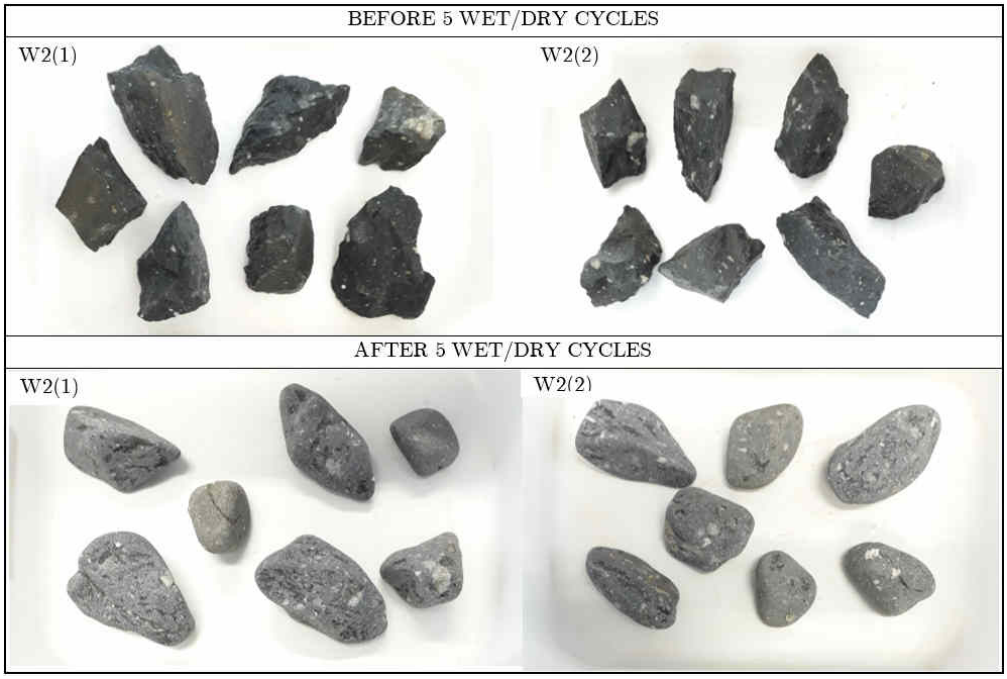

Table A.9: Photographs of highly weathered (W4) tillite rock lumps before and after 5 wet/dry cycles.

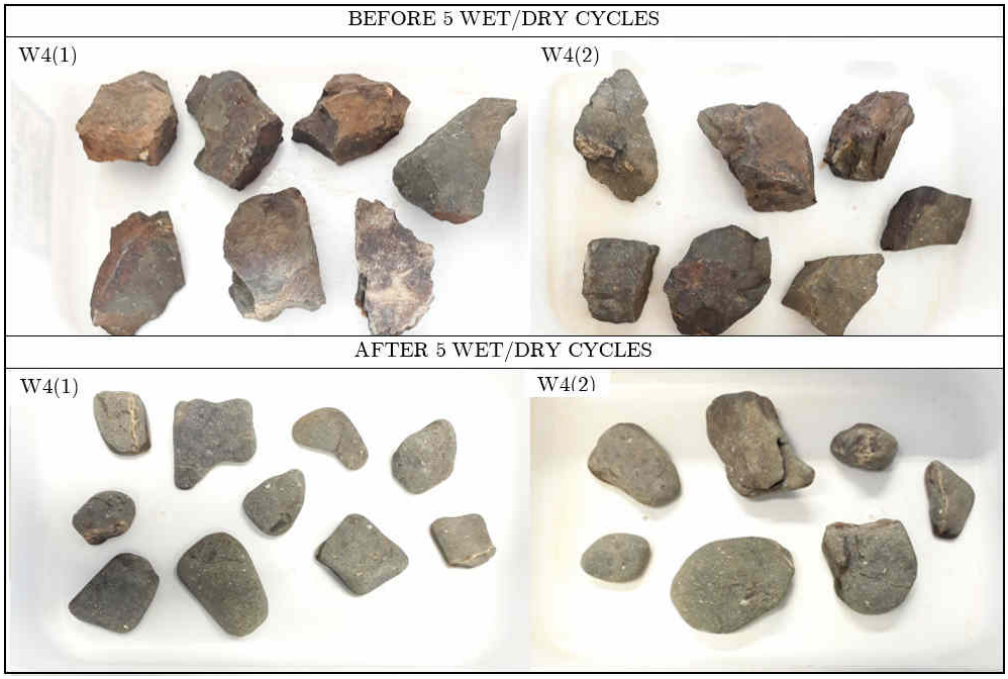

Appendix B

Rock Mass Characterization

B.1 Electro-Resistivity

Table B.1: Electro-resistivity inversion settings.

Parameter		Value
Type:	2D-Multicable, dipole-dipole (N4)	-
Spacing:	First element	0 m
	Length	995 m
	Electrode spacing	5 m
	S-min	0 m
	S-max	995 m
Reading:	Edge type	Full
	Pulse	0.5 s
	Tot. measurement distance per cable section	40 m
	Stacking	4
	Max. error	5%
	Power	850 W
Damping factors:	Initial value	0,15
	Minimum value	0,02
	Higher damping factor for first layer	5
	Use higher damping factors	No
	Adjust damping factors	Yes
Forward modeling:	4 nodes	Yes
	Finest mesh	Yes
	Finite-difference method	Yes
Robust inversion:	Use standard data constraint	Yes
	Cutoff factor	0,05
	Use standard model constraint	Yes
	Cutoff factor	0,005
	Reduce effect of side blocks	Yes
	Limit resistivity range	Yes
	Enable all options	No
Model discretization:	Extended model, cells half-width of unit spacing	Yes

B.2 Core Logging

Table B.2: Core logging description definitions.

Parameter	Description	
Colour		
Colour	(Munsell colour chart)	
Degrees of weathering		
Unweathered	Completely fresh blueish grey tillite Very hard (70 MPa - 200 MPa)	
Slightly weathered	Similar to unweathered tillite Stained brown on discontinuity planes	
Medium weathered	Stained brown throughout Hard (25 MPa - 70 MPa) to soft (3 MPa - 10 MPa)	
Highly weathered	Stained yellow, pink or white; structure retained Soft (3 MPa - 10 MPa) to very soft (1 MPa - 3	
Completely weathered	Stained dark brown to black; gravelly residual soil Little to no inherited fabric; soft/stiff/loose gravel	
Parameter	**Value**	**Unit**
Fabric		
Very finegrained	< 0,06	mm
Finegrained	0,06 - 0,2	mm
Medium grained	0,2 - 0,6	mm
Coarse grained	0,6 - 2,0	mm
Very coarse grained	> 2,0	mm
Discontinuity spacing		
Very widely	> 1000	mm
Widely	300 - 1000	mm
Medium	100 - 300	mm
Closely	30 - 100	mm
Very closely	10 - 30	mm
Hardness		
Very soft	1 - 3	MPa
Soft	3 - 10	MPa
Medium hard	10 - 25	MPa
Hard	25 - 70	MPa
Very hard	70 - 200	MPa
Extremely hard	> 200	MPa

B.3 Unconfined Compressive Strength (UCS) Tests

Table B.3: Unconfined Compressive Strength (UCS) calculations for standard cylindrical specimens.

Specimen	Borehole	Depth (m)	Grade (Wi)	Area (mm^2)	Rate (MPa/s)	Rate (kN/min)	Failure Load (kN)	Failure Load (MPa)
S1	BH1	2,8 - 3,1	W1	7854,0	0,5	235,6	445,6	56,7
S2	BH1	2,4 - 2,7	W1	7088,2	0,5	212,6	479,8	67,7
S3	BH3	1,0 - 1,5	W2	6503,9	0,5	195,1	404,1	62,1
S4	BH2	1,5 - 1,8	W1	6792,9	0,5	203,8	510,3	75,1
S5	BH2	1,8 - 2,1	W1	6647,6	0,5	199,4	664,4	99,9

Table B.4: Unconfined Compressive Strength (UCS) calculations for tillite cube specimens.

Specimen	Borehole	Depth (m)	Grade (Wi)	Area (mm^2)	Rate (MPa/s)	Rate (kN/min)	Failure Load (kN)	Failure Load (MPa)
1	BH1	0,1-1,8	W2	2550	0,5	76,5	213,2	83,6
2	BH1	0,1-1,8	W2	2591	0,5	77,7	265,5	102,5
3	BH1	1,9-3,0	W1	2612	0,5	78,4	275,7	105,5
4	BH1	1,9-3,0	W1	2650	0,5	79,5	205,6	77,6
5	BH3	2,4-2,9	W2	2702	0,5	81,1	214,1	79,3
6	BH3	2,4-2,9	W2	2703	0,5	81,1	190,8	70,6
7	BH3	2,4-2,9	W2	2600	0,5	78,0	153,1	58,9
8	BH3	2,4-2,9	W2	2625	0,5	78,8	165,5	63,1
9	BH3	1,1-1,4	W2	2500	0,5	75,0	279,1	111,6
10	BH3	1,1-1,4	W2	2654	0,5	79,6	208,7	78,6
11	BH3	1,1-1,4	W2	2525	0,5	75,8	164,1	65,0
12	BH3	1,1-1,4	W2	2476	0,5	74,3	160,1	64,6
13	BH3	1,1-1,4	W2	2677	0,5	80,3	210,5	78,6
14	BH2	2,2-2,8	W1	2525	0,5	75,8	232,8	92,2
15	BH2	2,2-2,8	W1	2525	0,5	75,8	197,4	78,2
16	BH2	2,2-2,8	W1	2625	0,5	78,8	254,2	96,9
17	BH2	2,2-2,8	W1	2627	0,5	78,8	319,8	121,8
18	BH3	1,8-2,1	W3	2470	0,5	74,1	61,0	24,7
19	BH3	1,8-2,1	W3	2330	0,5	69,9	55,1	23,6
20	BH3	1,8-2,1	W3	2678	0,5	80,3	67,5	25,2
21	BH3	1,0-1,5	W2	2575	0,5	77,3	205,1	79,7
22	BH3	1,0-1,5	W2	2659	0,5	79,8	140,3	52,8
23	BH1	1,9-3,0	W1	2573	0,5	77,2	193,3	75,1
24	BH1	2,4-2,7	W1	2652	0,5	79,6	241,9	91,2
25	BH1	2,4-2,7	W1	2325	0,5	69,8	168,7	72,6
26	BH2	2,2-2,8	W1	2835	0,5	85,1	224,1	79,0
27	BH2	2,2-2,8	W1	3048	0,5	91,4	315,6	103,5
28	BH1	0-1,8	W2	3145	0,5	94,4	214,7	68,3
29	BH1	0-1,8	W2	2677	0,5	80,3	199,0	74,3
30	BH3	0,4-0,7	W2	2410	0,5	72,3	164,5	68,3

Appendix C

Foundation Design

C.1 Design Loads

Table C.1: Bearing failure design loads calculations.

Characteristic Value, X_c		STR			STR-P			Unit
		γ_F	Design Value, X_d		γ_F	Design Value, X_d		
LC1: Operating Conditions, 120 km/h Extreme Wind Load								
$V_{k,dish}$	2649	1,2	$V_{d,dish}$	3178	1,35	$V_{d,dish}$	3576	kN
$V_{k,pedestal}$	18835	1,2	$V_{d,pedestal}$	22602	1,35	$V_{d,pedestal}$	25428	kN
$V_{k,base}$	7238	1,2	$V_{d,base}$	8686	1,35	$V_{d,base}$	9771	kN
$V_{k,wind}$	679	1,5	$V_{d,wind}$	1018	1,0	$V_{d,wind}$	679	kN
			$V_{d,total}$	**35484**		**$V_{d,total}$**	**39453**	**kN**
$H_{k,wind}$	1180	1,5	$H_{d,wind}$	1770	1,0	$H_{d,wind}$	1180	kN
			$H_{d,tot}$	**1770**		**$H_{d,tot}$**	**1180**	**kN**
$M_{k,dish}$	655	1,2	$M_{d,dish}$	786	1,35	$M_{d,dish}$	884	kNm
$M_{k,wind}$	2842	1,5	$M_{d,wind}$	4262	1,0	$M_{d,wind}$	2842	kNm
			$M_{d,tot}$	**5048**		**$M_{d,tot}$**	**3726**	**kNm**
LC2: Survival Position, 200 km/h Extreme Wind Load								
$V_{k,dish}$	2649	1,2	$V_{d,dish}$	3178	1,35	$V_{d,dish}$	3576	kN
$V_{k,pedestal}$	18835	1,2	$V_{d,pedestal}$	22602	1,35	$V_{d,pedestal}$	25428	kN
$V_{k,base}$	7238	1,2	$V_{d,base}$	8686	1,35	$V_{d,base}$	9771	kN
$V_{k,wind}$	-609	0,0	$V_{d,wind}$	0	0,0	$V_{d,wind}$	0	kN
			$V_{d,total}$	**34466**		**$V_{d,total}$**	**38775**	**kN**
$H_{k,wind}$	685	1,5	$H_{d,wind}$	1028	1,0	$H_{d,wind}$	685	kN
			$H_{d,tot}$	**1028**		**$H_{d,tot}$**	**685**	**kN**
$M_{k,dish}$	0	1,2	$M_{d,dish}$	0	1,35	$M_{d,dish}$	0	kNm
$M_{k,wind}$	6946	1,5	$M_{d,wind}$	10418	1,0	$M_{d,wind}$	6946	kNm
			$M_{d,tot}$	**10418**		**$M_{d,tot}$**	**6946**	**kNm**

Table C.2: Bearing failure design loads calculations cont'd.

Characteristic Value, X_c		GEO γ_F	Design Value, X_d		Unit
LC1: Operating Conditions, 120 km/h Extreme Wind Load					
$V_{k,dish}$	2649	1,0	$V_{d,dish}$	2649	kN
$V_{k,pedestal}$	18835	1,0	$V_{d,pedestal}$	18835	kN
$V_{k,base}$	7238	1,0	$V_{d,base}$	7238	kN
$V_{k,wind}$	679	1,5	$V_{d,wind}$	1018	kN
			$V_{d,total}$	**29740**	**kN**
$H_{k,wind}$	1180	1,5	$H_{d,wind}$	1770	kN
			$H_{d,tot}$	**1770**	**kN**
$M_{k,dish}$	655	1,0	$M_{d,dish}$	655	kNm
$M_{k,wind}$	2842	1,5	$M_{d,wind}$	4262	kNm
			$M_{d,tot}$	**4917**	**kNm**
LC2: Survival Position, 200 km/h Extreme Wind Load					
$V_{k,dish}$	2649	1,0	$V_{d,dish}$	2649	kN
$V_{k,pedestal}$	18835	1,0	$V_{d,pedestal}$	18835	kN
$V_{k,base}$	7238	1,0	$V_{d,base}$	7238	kN
$V_{k,wind}$	-609	0,0	$V_{d,wind}$	0	kN
			$V_{d,total}$	**28722**	**kN**
$H_{k,wind}$	685	1,5	$H_{d,wind}$	1028	kN
			$H_{d,tot}$	**1028**	**kN**
$M_{k,dish}$	0	1,0	$M_{d,dish}$	0	kNm
$M_{k,wind}$	6946	1,5	$M_{d,wind}$	10418	kNm
			$M_{d,tot}$	**10418**	**kNm**

Table C.3: Sliding failure design loads calculations.

Characteristic Value, X_c		STR			GEO			Unit
		γ_F	Design Value, X_d		γ_F	Design Value, X_d		
LC1: Operating Conditions, 120 km/h Extreme Wind Load								
$V_{k,dish}$	2649	0,9	$V_{d,dish}$	2384	1,0	$V_{d,dish}$	2649	kN
$V_{k,pedestal}$	18835	0,9	$V_{d,pedestal}$	16952	1,0	$V_{d,pedestal}$	18835	kN
$V_{k,base}$	7238	0,9	$V_{d,base}$	6514	1,0	$V_{d,base}$	7238	kN
$V_{k,wind}$	679	0,0	$V_{d,wind}$	0	0,0	$V_{d,wind}$	0	kN
			$V_{d,total}$	**25850**		**$V_{d,total}$**	**28722**	**kN**
$H_{k,wind}$	1180	1,5	$H_{d,wind}$	1770	1,5	$H_{d,wind}$	1770	kN
			$H_{d,tot}$	**1770**		**$H_{d,tot}$**	**1770**	**kN**
$M_{k,dish}$	655	1,2	$M_{d,dish}$	786	1,0	$M_{d,dish}$	655	kNm
$M_{k,wind}$	2842	1,5	$M_{d,wind}$	4262	1,5	$M_{d,wind}$	4262	kNm
			$M_{d,tot}$	**5048**		**$M_{d,tot}$**	**4917**	**kNm**
LC2: Survival Position, 200 km/h Extreme Wind Load								
$V_{k,dish}$	2649	0,9	$V_{d,dish}$	2384	1,0	$V_{d,dish}$	2649	kN
$V_{k,pedestal}$	18835	0,9	$V_{d,pedestal}$	16952	1,0	$V_{d,pedestal}$	18835	kN
$V_{k,base}$	7238	0,9	$V_{d,base}$	6514	1,0	$V_{d,base}$	7238	kN
$V_{k,wind}$	-609	1,5	$V_{d,wind}$	-913	1,5	$V_{d,wind}$	-913	kN
			$V_{d,total}$	**24936**		**$V_{d,total}$**	**27809**	**kN**
$H_{k,wind}$	685	1,5	$H_{d,wind}$	1028	1,5	$H_{d,wind}$	1028	kN
			$H_{d,tot}$	**1028**		**$H_{d,tot}$**	**1028**	**kN**
$M_{k,dish}$	0	1,2	$M_{d,dish}$	0	1,0	$M_{d,dish}$	0	kNm
$M_{k,wind}$	6946	1,5	$M_{d,wind}$	10418	1,5	$M_{d,wind}$	10418	kNm
			$M_{d,tot}$	**10418**		**$M_{d,tot}$**	**10418**	**kNm**

Table C.4: Overturning failure design loads calculations.

Characteristic Value, X_c		STR/EQU			GEO			Unit
		γ_F	Design Value, X_d		γ_F	Design Value, X_d		
LC1: Operating Conditions, 120 km/h Extreme Wind Load								
$V_{k,dish}$	2649	0,9	$V_{d,dish}$	2384	1,0	$V_{d,dish}$	2649	kN
$V_{k,pedestal}$	18835	0,9	$V_{d,pedestal}$	16952	1,0	$V_{d,pedestal}$	18835	kN
$V_{k,base}$	7238	0,9	$V_{d,base}$	6514	1,0	$V_{d,base}$	7238	kN
$V_{k,wind}$	679	0,0	$V_{d,wind}$	0	0,0	$V_{d,wind}$	0	kN
			$V_{d,total}$	**25850**		**$V_{d,total}$**	**28722**	**kN**
$H_{k,wind}$	1180	1,5	$H_{d,wind}$	1770	1,5	$H_{d,wind}$	1770	kN
			$H_{d,tot}$	**1770**		**$H_{d,tot}$**	**1770**	**kN**
$M_{k,dish}$	655	1,2	$M_{d,dish}$	786	1,0	$M_{d,dish}$	655	kNm
$M_{k,wind}$	2842	1,5	$M_{d,wind}$	4262	1,5	$M_{d,wind}$	4262	kNm
			$M_{d,tot}$	**5048**		**$M_{d,tot}$**	**4917**	**kNm**
LC2: Survival Position, 200 km/h Extreme Wind Load								
$V_{k,dish}$	2649	1,2	$V_{d,dish}$	3178	1,0	$V_{d,dish}$	2649	kN
$V_{k,pedestal}$	18835	1,2	$V_{d,pedestal}$	22602	1,0	$V_{d,pedestal}$	18835	kN
$V_{k,base}$	7238	1,2	$V_{d,base}$	8686	1,0	$V_{d,base}$	7238	kN
$V_{k,wind}$	-609	1,5	$V_{d,wind}$	-913	1,5	$V_{d,wind}$	-913	kN
			$V_{d,total}$	**33553**		**$V_{d,total}$**	**27809**	**kN**
$H_{k,wind}$	685	1,5	$H_{d,wind}$	1028	1,5	$H_{d,wind}$	1028	kN
			$H_{d,tot}$	**1028**		**$H_{d,tot}$**	**1028**	**kN**
$M_{k,dish}$	0	1,2	$M_{d,dish}$	0	1,0	$M_{d,dish}$	0	kNm
$M_{k,wind}$	6946	1,5	$M_{d,wind}$	10418	1,5	$M_{d,wind}$	10418	kNm
			$M_{d,tot}$	**10418**		**$M_{d,tot}$**	**10418**	**kNm**

Table C.5: Settlement design loads calculations.

Characteristic Value, X_c		SLS γ_F	Design Value, X_d		Unit
LC1: Operating Conditions, 120 km/h Extreme Wind Load					
$V_{k,dish}$	2649	1,1	$V_{d,dish}$	2914	kN
$V_{k,pedestal}$	18835	1,1	$V_{d,pedestal}$	20719	kN
$V_{k,base}$	7238	1,1	$V_{d,base}$	7962	kN
$V_{k,wind}$	679	0,6	$V_{d,wind}$	407	kN
			$V_{d,total}$	**32001**	**kN**
$H_{k,wind}$	1180	0,6	$H_{d,wind}$	708	kN
			$H_{d,tot}$	**708**	**kN**
$M_{k,dish}$	655	1,1	$M_{d,dish}$	720	kNm
$M_{k,wind}$	2842	0,6	$M_{d,wind}$	1705	kNm
			$M_{d,tot}$	**2425**	**kNm**
LC2: Survival Position, 200 km/h Extreme Wind Load					
$V_{k,dish}$	2649	1,1	$V_{d,dish}$	2914	kN
$V_{k,pedestal}$	18835	1,1	$V_{d,pedestal}$	20719	kN
$V_{k,base}$	7238	1,1	$V_{d,base}$	7962	kN
$V_{k,wind}$	-609	0,0	$V_{d,wind}$	0	kN
			$V_{d,total}$	**31594**	**kN**
$H_{k,wind}$	685	0,6	$H_{d,wind}$	411	kN
			$H_{d,tot}$	**411**	**kN**
$M_{k,dish}$	0	1,1	$M_{d,dish}$	0	kNm
$M_{k,wind}$	6946	0,6	$M_{d,wind}$	4167	kNm
			$M_{d,tot}$	**4167**	**kNm**

C.2 Ultimate Bearing Pressure

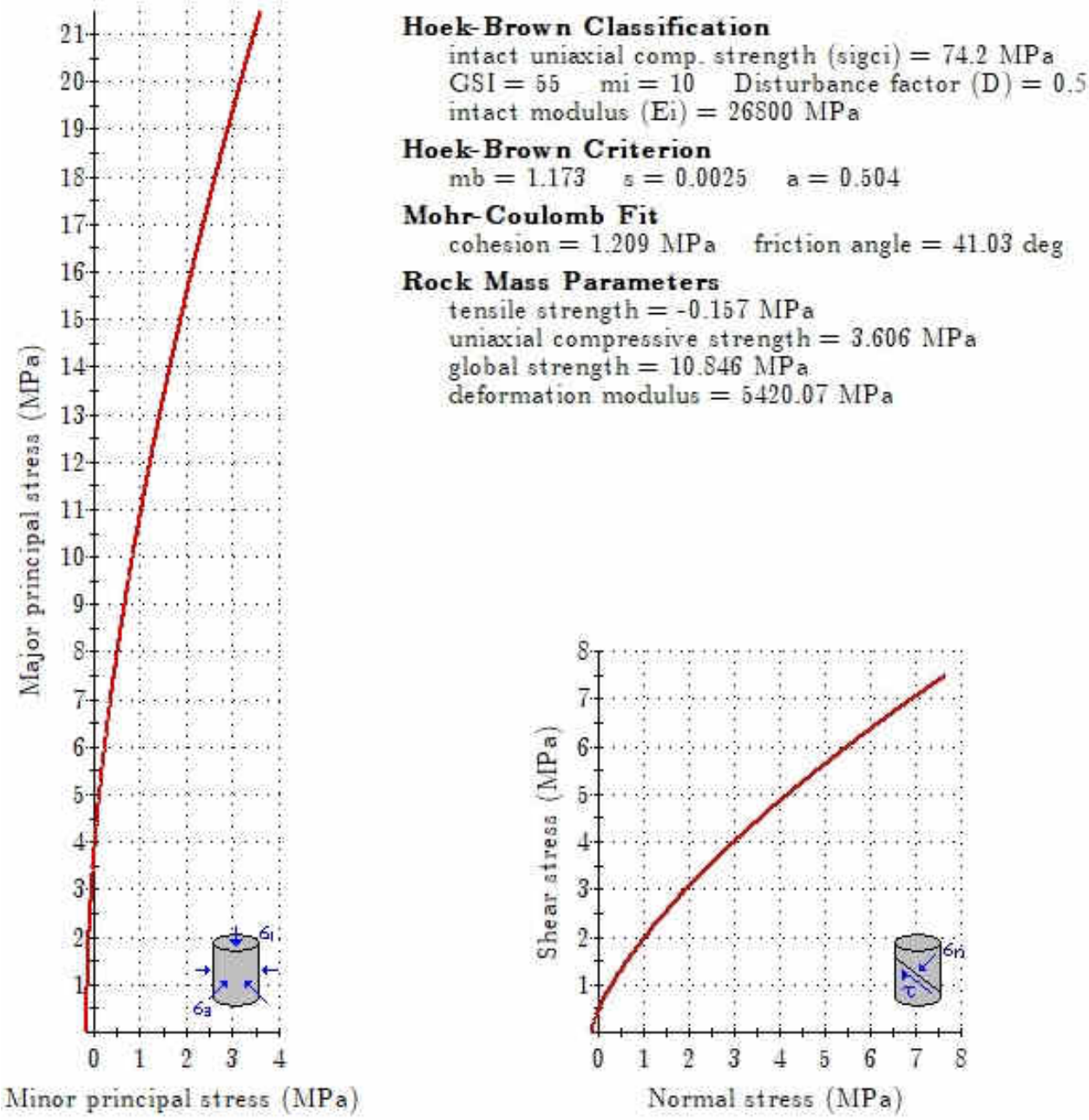

Figure C.1: Hoek-Brown failure envelope (Rocscience Inc., 2002).

C.3 Governing Limit States

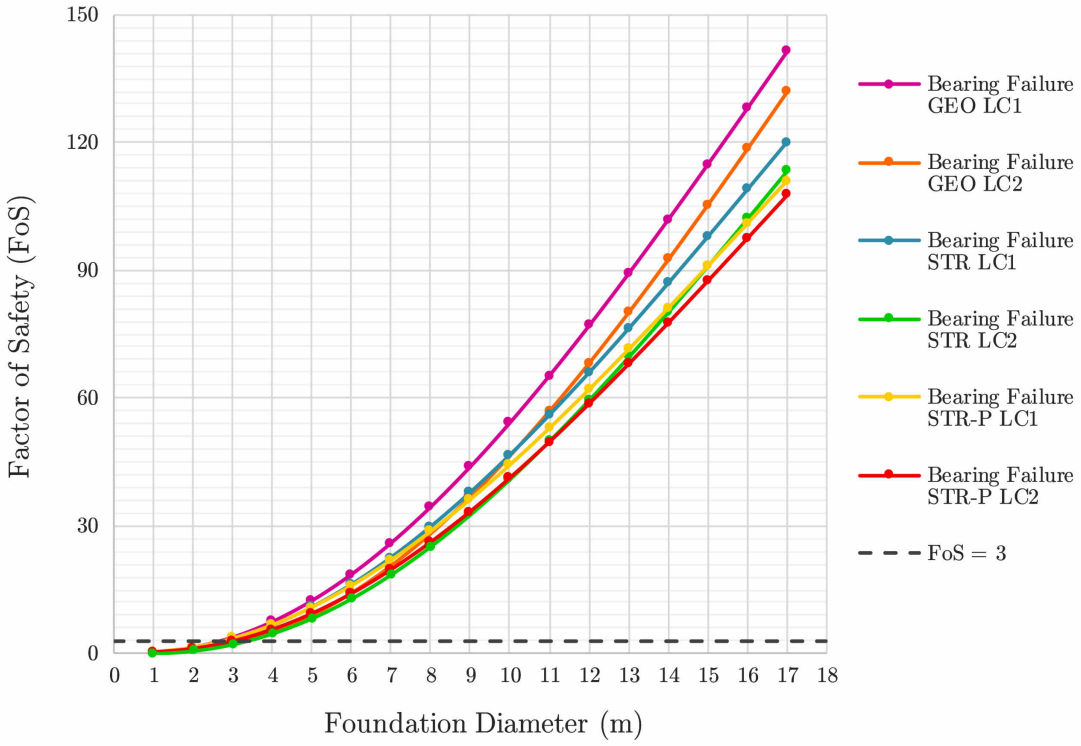

Figure C.2: Safety against bearing failure for the STR, STR-P and GEO limit states.

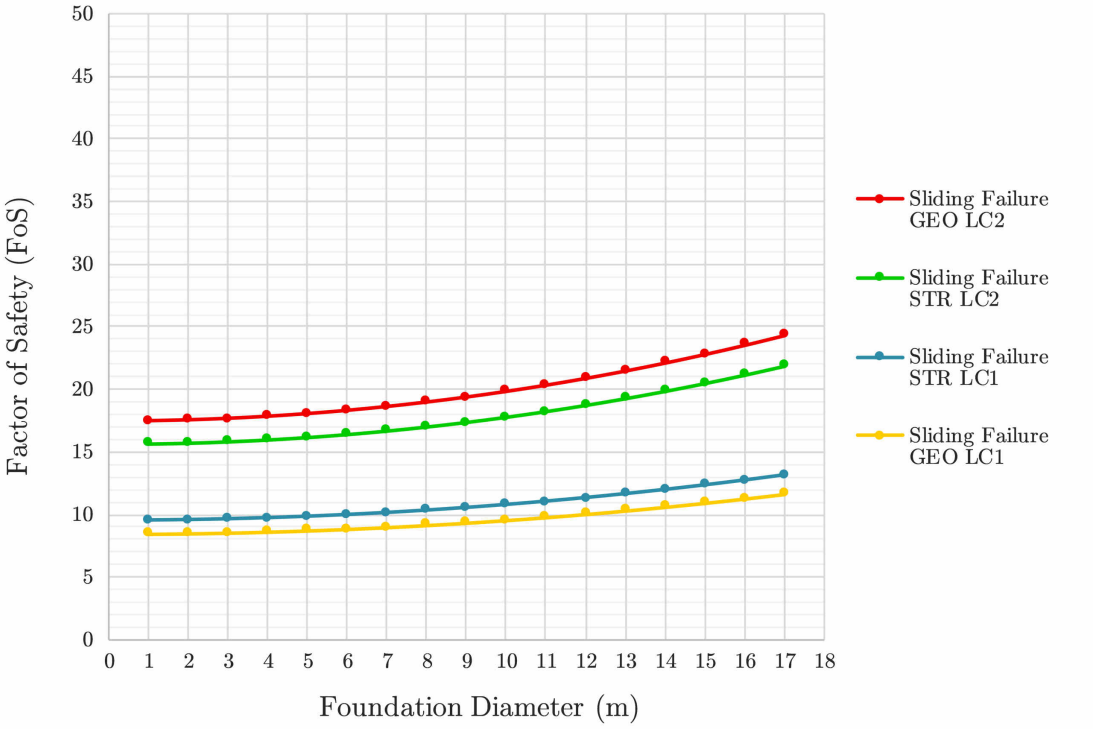

Figure C.3: Safety against sliding failure for the STR and GEO limit states.

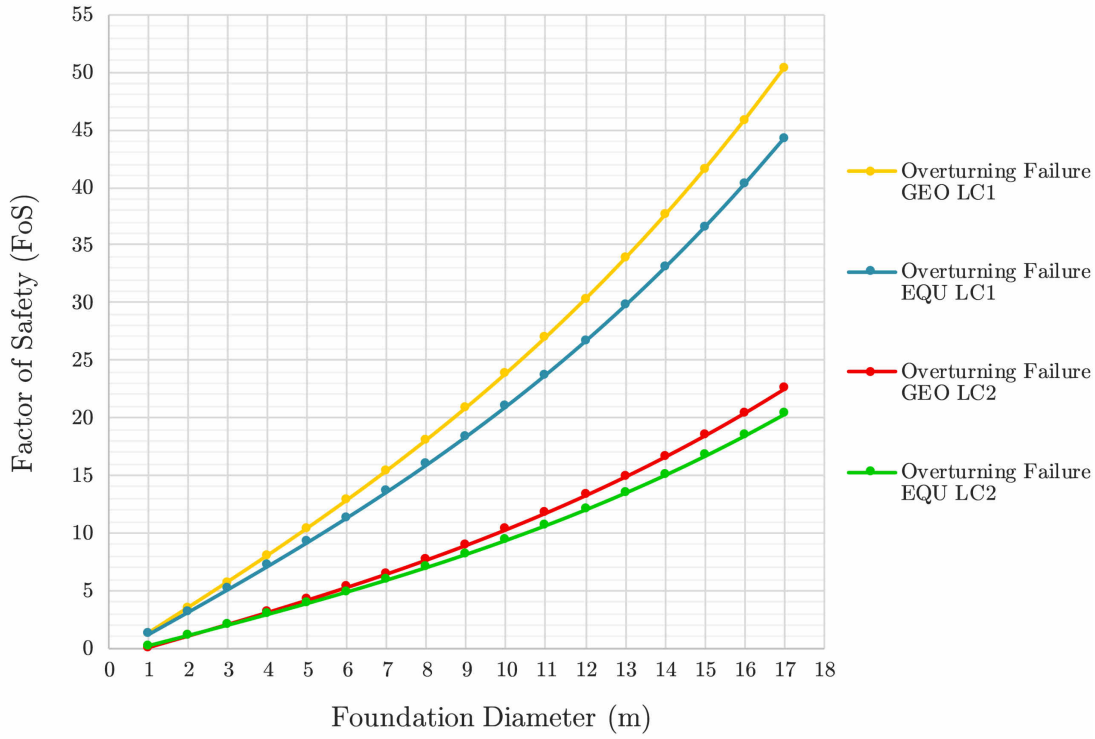

Figure C.4: Safety against overturning failure for the GEO and EQU limit states.